Process Monitoring, Modeling, and Quality Assessment for Printed Electronics with Aerosol Jet Printing Technology

A Dissertation
Presented to
The Academic Faculty

by

Yung-Hang Chang

In Partial Fulfillment
of the Requirements for the Degree
Doctor of Philosophy in the
H. Milton Stewart School of Industrial and Systems Engineering

Georgia Institute of Technology
August 2017

Process Monitoring, Modeling, and Quality Assessment for Printed Electronics with Aerosol Jet Printing Technology

Approved by:

Professor Ben Wang, Advisor
School of Industrial and Systems Engineering
Georgia Institute of Technology

Professor Jianjun Shi
School of Industrial and Systems Engineering
Georgia Institute of Technology

Professor Chun Zhang, Co-Advisor
School of Industrial and Systems Engineering
Georgia Institute of Technology

Professor Tequila A. L. Harris
The George W. Woodruff School of Mechanical Engineering
Georgia Institute of Technology

Professor Kamran Paynabar
School of Industrial and Systems Engineering
Georgia Institute of Technology

Date Approved: May 05, 2017

To my parents, and my sister

ACKNOWLEDGEMENTS

I would like to express my gratitude to my advisor, Dr. Ben Wang, for his constant support, guidance, and patience throughout my Ph.D. studies. I would also like to express my grateful to my co-advisor, Dr. Chuck Zhang, for his insightful encouragement and advice on my research.

I like to thank my committee member, Dr. Kamran Paynabar, Dr. Jianjun Shi, and Dr. Tequila Harris, for their dedications and constructive suggestions on my dissertation. Their time, their inputs, and advice are invaluable in completing the dissertation.

I also own my deep thanks to my good friend and colleague, Dr. Kan Wang, who offer plenty of help not only in my research but also in my life.

I would like to appreciate all staff members at Georgia Tech Manufacturing Institute, Mrs. Martha Miller, Ms. Laura Day, Mrs. Latanya Buckner, Mr. Ben Coffman, Mr. David Barnes, Mr. Will Smith, Dr. Billyde Brown, Dr. Jianfeng Shi. It is my pressure to work with such a wonderful team.

Finally, I would like to thank my parents and my sister for their encouragement and patient throughout my life and education.

TABLE OF CONTENTS

LIST OF TABLES

LIST OF FIGURES

SUMMARY

Printed electronics (PE) technology has attracted significant attention in recent years due to its potential to simplify process steps and reduce costs when compared to conventional photolithography. Conventional photolithography consists of multiple steps, including thin film vapor deposition, photoresist deposition, masking, and wet etching. PE technology, on the other hand, is a one-step deposition process with post-sintering (or baking) to activate printed ink functionality. Furthermore, PE technology can be readily scaled to large-area production with high throughput with roll-to-roll printing. These features can be applied in a way that lowers cost and offers flexibility for work in large areas. These features offer new ways to develop novel electronics and accelerate their use in other areas of research and production. Examples include rapid prototyping, pilot production, small lot size production, organic light emitting diodes, organic solar cells, thin-film transistors, logic circuits, radio frequency identification (RFID) tags, and sensors.

Aerosol jet printing (AJP) was developed in 2007 by Optomec, Inc., to fulfill the increasing demand for miniature and flexible electronics. According to Thomson Reuters, more than 500 journal papers on using AJP for research in the PE area were published in the last five years. Compared with other PE technologies, such as screen printing and inkjet printing, AJP has demonstrated superior capabilities, for example, having a smaller feature size, thinner layer deposition, a larger pool of available ink and substrate materials, non-planar printing capability, and a low processing temperature. These

advantages make AJP one of the most competitive manufacturing technologies in the PE industry today.

There are some limitations however. AJP is limited by not having in situ monitoring or control capabilities, which leads to inconsistent performance in products. Up to today, most AJP systems are installed in laboratories or research centers for fundamental research, product design, and prototyping. In spite of the increasing maturity of lab-scale fabrication, the lack of quality control becomes a critical roadblock for this transformative technology to be a viable production process. Using AJP for industrial applications involves complex system interactions including printed materials, process parameters, environment, post treatment, and device characterization, all of which require an in-depth understanding of the science and engineering of AJP. Since AJP is a relatively new technology in the electronics industry, the knowledge base is relatively limited. In addition, there are no well-established guidelines or standards to define the quality of printed electronic products and information is lacking on the lifetime performance of printed devices.

The objective of this proposed research is to create a knowledge base and establish engineering methods and tools for AJP quality control by understanding the relationships between the AJP process, properties, structure, morphology and performance. The research conducted in the following steps:

Chapter 4 focuses on developing monitoring methods for the AJP process and includes a vibration-based wavelet method for atomization monitoring and image processing techniques for extracting quantitative printed line quality matrices. In the end of the

chapter, a design of experiment model using central composite design (CDD) is conducted to create a process model and create printing optimization guidelines.

Chapter 5 presents two representative applications that could benefit from AJP technologies, but they suffer from process variation. The finding and results concluded in Chapter 4 are applied to the process to demonstrate the effectiveness. We observed a 20% variation reduction and a 50% completion rate improvement in gas sensor and 3D transmission line fabrication, respectively.

Chapter 6 demonstrates two novel manufacturing processes that extend current AJP capabilities into 3D printing and the nanocomposite fabrication area. A facile method called print-stick-peel (PSP) was developed for integrating printed sensors into 3D printed objects. This method overcomes several challenges in the integration of 3D printing and printed electronics such as surface roughness, surface mismatch, and temperature limitation. Another method developed is called dual material aerosol jet printing (DMAJP), which can mix polymer and conductive filler material in different ratios on the fly. This method can fabricate conductive tailorable nanocomposites in a single piece and machine setup, which has a potential impact on soft robotics and nano-actuator research.

CHAPTER 1. INTRODUCTION

1.1 Overview

Printed electronics (PE) technology has attracted significant attention in recent years due to its potential to simplify process steps and reduce costs when compared to conventional photolithography. Conventional photolithography consists of multiple steps, including thin film vapor deposition, photoresist deposition, masking, and wet etching. PE technology, on the other hand, is a one-step deposition process with post-sintering (or baking) to activate printed ink functionality. Figure 1 compares steps between the conventional lithography process and PE technology.

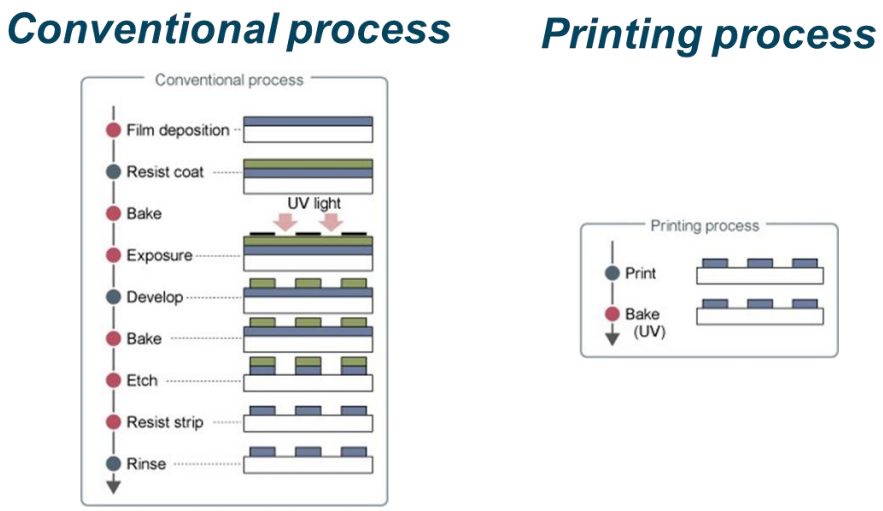

Figure 1: Process Steps between a Conventional Process and a Printing process

Furthermore, PE technology can be readily scaled to large-area production with high throughput with roll-to-roll printing. These features can be applied in a way that lowers cost and offers flexibility for work in large areas. These features offer new ways to

develop novel electronics and accelerate their use in other areas of research and production. Examples include rapid prototyping, pilot production, small lot size production, organic light emitting diodes, organic solar cells, thin-film transistors, logic circuits, radio frequency identification (RFID) tags, and sensors.

Aerosol jet printing® (AJP) was developed in 2007 by Optomec, Inc., to fulfill the increasing demand for miniature and flexible electronics. According to Thomson Reuters, more than 500 journal papers were published in the last five years that use AJP capabilities for research in the PE area. Compared with other PE technologies, such as screen printing and inkjet printing, AJP has demonstrated superior capabilities, for example, having a smaller feature size, thinner layer deposition, a larger pool of available ink and substrate materials, non-planar printing capability, and a low processing temperature. These advantages make AJP one of the most competitive manufacturing technologies in the PE industry today.

The AJP process is also fast, flexible, and has a high tolerance for errors. It saves time for circuit designers by directly converting patterns in CAD/CAM files into prototypes. It also has a much wider range of inks and substrates. Most importantly, it greatly simplifies the manufacturing process. Masking and screen-printing processes take several steps to fabricate a circuit. Making a mask or a new screen can take days, even weeks. With the AJP process, there is the possibility of turning what used to take weeks of prototyping into hours. With this kind of improvement, it seems inevitable that the AJP process will revolutionize the electronics industry.

1.2 Problem Statement & Objective

Although AJP possesses several unique capabilities, there are some limitations. AJP is limited by not having in situ monitoring or control capabilities, which leads to inconsistent performance in final products. To date, most AJP systems were installed in laboratories or research centers for fundamental research, product design, and prototyping. In spite of the increasing maturity of lab-scale fabrication, the lack of quality control becomes a critical roadblock for this transformative technology to become a viable production process. Using AJP for industrial applications involves complex system interactions including printed materials, process parameters, environment, post treatment, and device characterization. All of these require an in-depth understanding of the science and engineering of AJP. Since AJP is a relatively new technology in the electronics industry, the knowledge base is relatively limited. In addition, there are no well-established guidelines or standards to define the quality of printed electronic products. Information is lacking on the stability of the printing process and lifetime performance of printed devices.

Because of the complex multiphase fluid dynamics involved in an AJP system, the quality of printed lines can be affected by uncertain factors presented by materials, manufacturing processes, working environments, or even operators. Some of these factors are constantly changing. For example, most types of ink used in AJP employ co-solvent systems for stabilization. Different volatility properties of solvents result in different internal pressures inside the system during atomization. Adding a gas-washing pretreatment can alleviate this issue. However, this increases the system complexity by

introducing more variables into the process. With these uncertainties, the inconsistency in line printing quality is almost inevitable.

Several researchers have been investigating the relationship between process parameters and printed morphologies, as well as developing computational fluid dynamic models for the deposition process. These investigations are based on the assumptions that the source, or the atomization process, is stable over time. In reality, the atomization process is changing from time to time and its behavior varies by the ink material compositions. There is still a lack of monitoring tools that can report the process stability information and communicate with maintenance staff requesting remedial action. The challenge of the lack of monitoring strategies yields low completion rates at both the prototyping and production levels. Large variation in the device performance is observed from batch to batch. There is a more detailed review and discussion of current quality issues in the AJP process in the next chapters.

The objective of this research consists of three major parts. In the first part, we explore the capabilities of the AJP process for manufacturing innovative devices with novel materials and advanced designs. Through the fabrication process, several manufacturing challenges and limitations in AJP quality control are identified. In the second part, we created a series of engineering methods and establish a knowledge base to address these drawbacks through statistical process control tools. In the third part, we discover and develop new process methods that can move AJP capability to another emerging advanced manufacturing area such as 3D printing and nanocomposite fabrication.

1.3 Thesis Organization

The thesis is organized as follows: Chapter 2 reviews existing literature related to printed electronic technologies, their quality control, process modeling and device applications. Chapter 3 introduces the research structure and methodology for this thesis topic. Chapter 4 introduces two representative applications of AJP for demonstrating its unique capabilities, as well as identifying the fabrication variation and limitations in developing these applications. The applications include a printed ammonia gas sensor for hazardous environment detection, and a transmission line for a D-band wireless application. Chapter 5 introduces process monitoring strategies for the AJP process, which includes an image-based quality metrics for printed line morphologies, a vibration-based signal analysis for atomization process monitoring, and a design of experiment for investigating process parameters. Chapter 6 explores new manufacturing processes based on AJP. Two novel process methods were developed for extending the AJP capability to emerging advanced manufacturing fields, including 3D printing and nanocomposite fabrication. Chapter 7 summarizes the thesis and introduces future research direction.

CHAPTER 2. LITERATURE REVIEW

2.1 Printed Electronic Technologies

Printing technologies such as screen printing, gravure printing, flexography printing, and offset printing have been applied to conventional electronics fabrication for a long time. They have also been applied to the manufacturing processes of many advanced PE products. Depending on the nature of the PE product, a suitable choice of manufacturing method has to be made regarding the ink, substrate, designed device structure, pattern geometry, manufacturing speed, yield, quality, and production cost.

PE technologies can be generally categorized into two major groups based on how the ink is ejected and deposited: contact printing and non-contact printing [1]. Figure 2 shows the sub-categories of the printing electronic process. Each technology has its own advantages and disadvantages. Contact printing is best suited for low-resolution and high-throughput applications. Non-contact printing is flexible in design and uses less material. It is more suitable for rapid prototyping and novel sensor development. The throughput of non-contact printing is typically lower than that of contact printing. However, the feasibility of scaling a non-contact printing process has been proven with a parallel nozzle array [2].

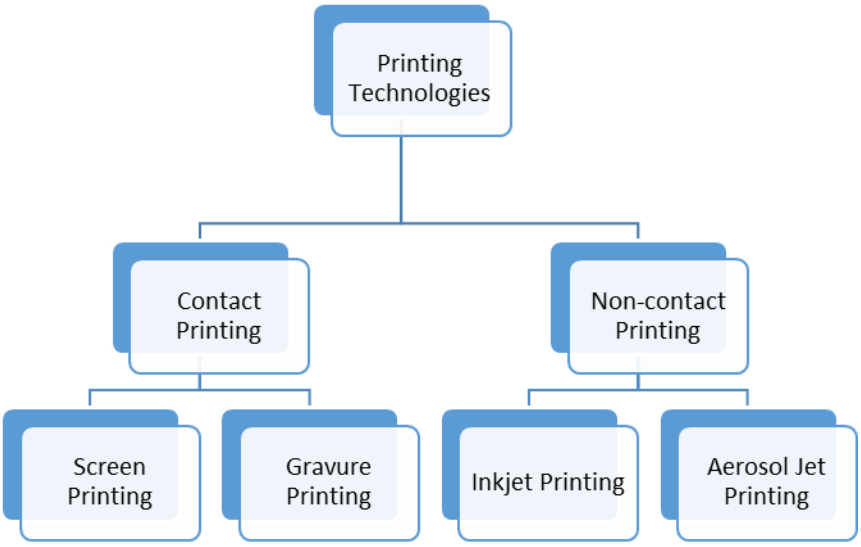

Figure 2: Printing Technology Categories

2.1.1 Screen Printing

Screen printing is a very mature technology for printed electronics and has been adopted for use in making printed circuit boards (PCB), interconnect fabrications, and printing current collectors for solar cells. The process of screen printing is illustrated in Figure 3. A squeegee forces ink through a screen to create patterns on a target substrate. After transfer, the ink remains in the voids and the screen is lifted. Screen printing has been used for fabricating numerous printed electronic devices including organic thin film transistors [3], photovoltaics [4-6], and sensors [7, 8].

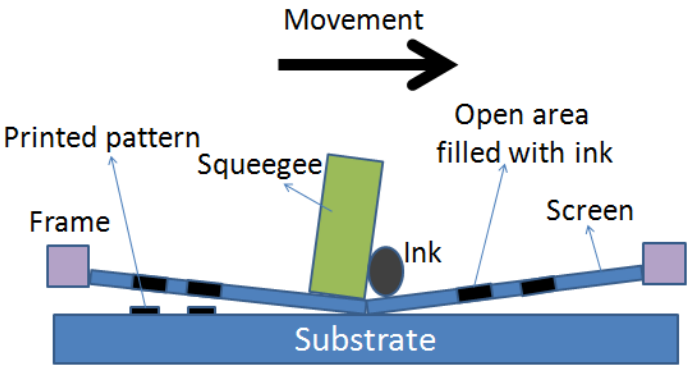

Figure 3: Screen Printing Process [9]

2.1.2 Gravure Printing

Gravure printing is a promising technology for printing devices that require higher resolutions than screen printing can provide. A schematic of gravure printing is shown in Figure 4. Gravure printing is used in industries that require high-quality and high-speed printing such as the magazine industry and the printing of currency. The working mechanism for gravure printing begins with a cylinder patterned with cavities called a print roller going through an ink reservoir to coat the cylinder uniformly. A doctor blade removes the excess ink outside of the cavities. The gravure cylinder or impression roller then presses onto a target substrate to transfer the desired pattern. The gravure process has high throughput and high resolution. It is suited for large area and low cost device fabrication. Several researchers have demonstrated using gravure printing for fabricating printed electronic devices including electrodes [10], transistors [11], RFIDs [12], and indium tin oxide (ITO) [13]. Novel 2D materials, such as carbon nanotubes and graphene, were also printed using gravure printing [14, 15].

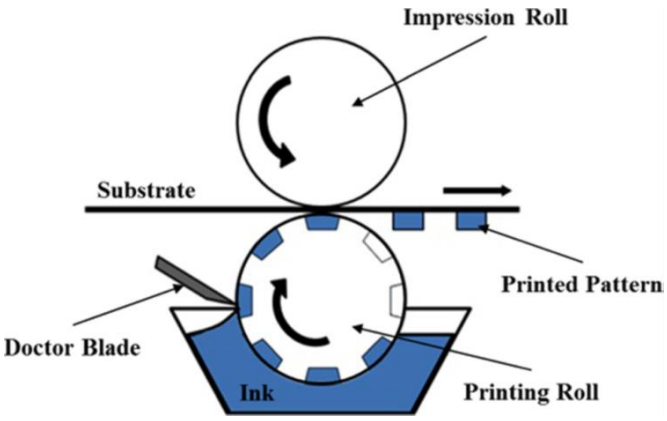

Figure 4: Gravure Printing Process

2.1.3 Inkjet Printing

Inkjet printing is a drop-on-demand additive printing technology. Unlike screen and gravure printing, inkjet printing does not require a patterned stencil or cylinder. Instead, digital layout files are used to define the printing patterns. In inkjet printing, the printing head moves along the stage as drops are jetted onto the substrate. There are three primarily energy sources that used for droplet creation: heat, piezoelectric deflection and electrical field. Figure 5(a) described a heat generated inkjet method. A heating element is warmed and vaporized nearby ink which creates a pressure wave that forces a droplet out of a nozzle. A major drawback to this method is that the inks used must be compatible with the temperature pulses which limited the variety of the ink selection. An alternative method is piezoelectric jetting (Figure 5(b)). With this method, a piezoelectric plate is deformed by an applied electric field. This deformation creates an acoustic wave and forces out ink droplet. This jetting method can work with a wide range of inks of intermediate viscosity and surface tension.

The third jetting method is electrohydrodynamic printing which is capable to create tiny jetted drops and fabricate highest resolution printing circuits. Electrohydrodynamic uses an electric field between a pendant drop of ink at the jetting nozzle and the substrate to deform the meniscus of this nozzle drop and force a small drop from its nadir as shown in figure 5(c).

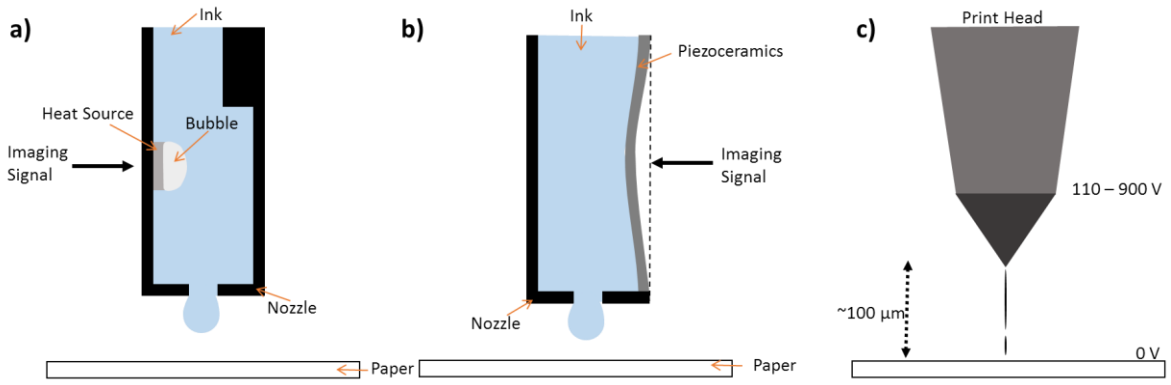

Figure 5: Inkjet Printing Process (a) thermal bubble, (b) piezoelectric, and (c) electrohydrodynamic [16]

Inkjet printing has been widely adopted in many printing electronics research groups because of the low cost of inkjet printers and the flexibility to work on different materials. Inkjet printing has been used to fabricate thin film transistor (TFT) consisting of zinc oxide (ZnO) and polyvinylpyrrolidone (PVP) as the active device region and gate dielectric, respectively[17]. An inkjet printing and vacuum drying process can be used to develop a high performance n-channel transistor that has a uniform amorphous C60 Fullerene[18]. Resistors, capacitors and inductors are developed using inkjet printing on polyimide substrate with various functional inks [19-22]. Recently, carbon nanotubes and graphene materials were successfully printed using inkjet technology for flexible transistors and advance sensors [23, 24].

2.1.4 Aerosol Jet® Printing

Aerosol jet printing is a relatively new non-contact printing method in printed electronics. In the aerosol jet printing process, functional inks are aerosolized with an atomizer. A gas stream is used as carrier gas to direct aerosol particles toward the deposition head. A sheath gas flow is used in the deposition head to aerodynamically focus the aerosol flow. Figure 6 shows a schematic of aerosol jet printing. The AJP process consists of three major steps: 1) Atomization step for generating aerosolized particles; 2) Deposition process for controlling deposition flow rates; and 3) Post treatment step for activating ink functionality through thermal, laser, or UV.

One important benefit for AJP is the long standoff distance between the printing head and the substrates. Therefore, the substrate does not have to be planar in order to print the desired pattern on it. The only limitation for the substrate being used in AJP is mostly governed by the ink properties. The limitations on the ink for AJP are the physical and chemical properties that enable the ink to be atomized. A range of materials have been developed and used for printing conductors, semiconductors and dielectrics.

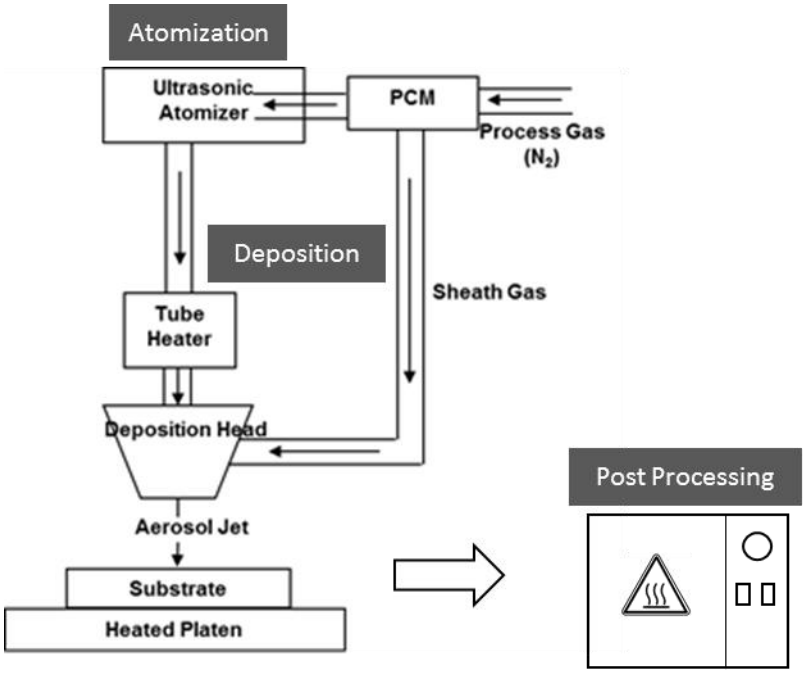

Figure 6: Aerosol Jet Printing Process

2.2 Major Challenges in Printed Electronics and Aerosol Jet® Printing

The field of PE is fast evolving with the newest material technologies and mechanical engineering technologies. One reflection of this is the rapid expansion of the range of materials PE technologies can process. Piezoelectric inks, semiconductor inks, biological inks, and other functional inks have been added to this set in recent years. The viscosity of the ink is also less of a limitation with the newly developed processes. For example, aerosol jet printing, which is one of the newest members of PE technologies, can theoretically process inks with any viscosity within a range of 1 cP to 3000 cP, whereas inkjet printing typically requires the ink viscosity to be between 8-12 cP. However, there are still a number of considerations regarding printability when choosing an ink for a PE process [25, 26].

2.2.1 Ink Dispersion Stability

One serious consideration for choosing an ink material is its stability [27, 28]. The majority of inks for PE processes are in a form of suspension, such as metallic nanoparticle inks, ceramic inks, and carbon-based nanomaterial inks. To disperse the nanoparticles homogeneously, an appropriate solvent must be identified. Usually, surfactants are also needed to keep the nanoparticles in suspension from re-aggregating. However, surfactants can adversely affect the properties of printed devices, especially the electrical conductivity. The dilemma is that surfactants are required to separate nanoparticles in the ink, but aren't desired in the final product where the nanoparticles are supposed to be in touch with each other without barriers. Even with surfactants, agglomeration is destined to happen in most suspension inks. This leads to the most common problem with PE machines: nozzle clogging. Because of the size of nanoparticles and possible agglomerates, the reduction in diameter of the printing nozzle is limited; therefore, the print resolution is also limited. A possible solution to this issue is to develop solution inks to replace suspension inks, like the particle-free reactive silver ink developed by Lewis, et al. This ink can print through 100 nm nozzles, which is one order of magnitude smaller than the suspension inks.

Another challenge with the inks is the material lifetime [29]. Some inks, or the solvents of the inks, are reactive when exposed to light, moisture, oxygen, or heat sources. After synthesis, the content of those inks are continuously changing. This makes the performance of printed devices unpredictable. It is even a larger problem when considering the supply chain of the entire PE industry. There are some good formulas for

conventional metallic inks that have been tested in the market for many years. However, it is a very common issue among newly developed inks, especially biological inks.

Other than the issues with the materials, there are other challenges in the printing processes like the registration of printed patterns for multi-layer devices [30]. For precisely designed electronics, the layout of different layers has to overlap exactly in order for the device to work properly. However, the running part needs to be taken out from the printing machine for sintering/drying/curing after each layer is printed. Positioning errors are inevitable, even with the best part handling system, because of the precision limits of the printing stage and the dimension change of the printed pattern after sintering/drying/curing. There are some image-based systems for registration, but the improvements are not satisfactory.

2.2.2 Inks and Substrates Mismatch

The inks and substrates used in PE devices cause many issues at the process level. For example, the sintering/drying/curing of a certain ink has to be compatible with the thermal tolerances of the corresponding substrate. This is an important issue in 3D printing/printed electronics integration as many 3D printable materials are plastics with a low working temperature. Conductive inks usually require high temperature post-processing. To solve this problem, research has been done on transferring printed patterns from a temporary, high-temperature substrate to the destiny surfaces using the differences in surface energies [31]. Another possible solution is to develop low temperature sintering conductive inks.

2.2.3 Quality Control and Repeatability of Aerosol Jet Printing

The uniformity of the printed pattern is another issue with the processes, especially the direct-write processes. The lines printed by PE processes often have ill-defined edges, discontinuity, overspray, etc., as shown in Figure 7. The areas filled by those lines, therefore, have voids, uneven thickness, rough surface, etc. Many of these are not effectively controlled in current practice, which leads to another challenge - quality control and repeatability.

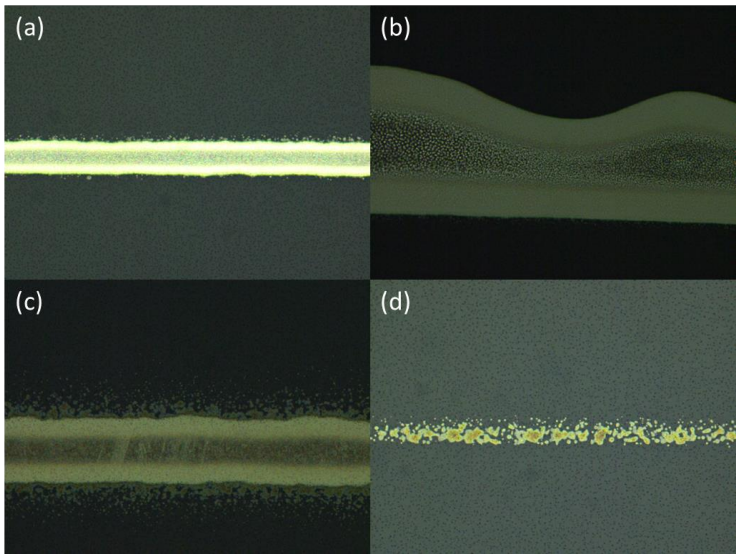

Figure 7: Uniformity issues in printed lines. (a) A typical printed line by aerosol jet printing; (b) voids and ill-defined edges; (c) overspray; (d) discontinuity [32]

Compared to conventional electronics manufacturing, PE technologies are far below the current standards of quality control in the industry. The poor repeatability of printed electronics devices is a combined effect of many factors, such as unstable inks, substrate wettability, defects in printed patterns, ink/substrate adhesion, dynamic machine condition, uncontrolled printing atmosphere, etc. With the development of in situ monitoring technology and automatic process control methodologies, the repeatability of

PE technologies is expected to gradually improve with the amount of ongoing research being done.

Several researchers have studied the evolution of line morphology by adjusting the AJP parameters that are controllable. Goth et al. [33] first studied aerosol jet printed silver lines and revealed the relationship between the width of the printed lines and the process parameters, three adjustable flow rates and the stage speed. Figure 8 shows the correlation between line width and flow settings for two different print velocities. It shows that the printed line width increases when the flow control parameters also rise.

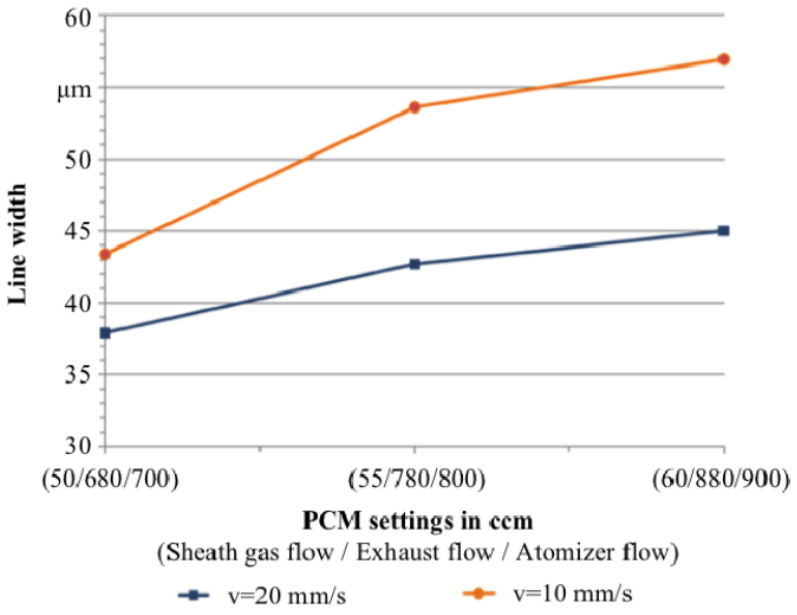

Figure 8: Line width relationship with flow settings [33]

Verheecke et al. [34] also studied aerosol jet printing with a pneumatic atomizer and developed a process window of the three gas flow rates to produce conductive lines with well-defined edges. A qualitative chart was developed to determine printed line quality attributes. They also developed a simple quantitative analysis to characterize line width

and edge smoothness. Mahajan et al. [35] systematically studied the relationship between process variables and silver line geometry and developed a simple process model. The effects of flow rate parameters and their effects on geometrical and electrical properties of aerosol jet printed lines were also investigated. The effect of independently increasing each of the process variables on printed line geometry is summarized in Table 1. The operability window and process regime for AJP are shown in Figure 9.

Process Variable	Line Width	Line Thickness
Focusing Ratio	Decreases	Increases
Nozzle Diameter	Increases	Decreases
Carrier Gas Flow Rate	Remains the Same	Increases
Stage Speed	Decreases	Decreases

Table 1: Effect of process variable on printed width and thickness [35]

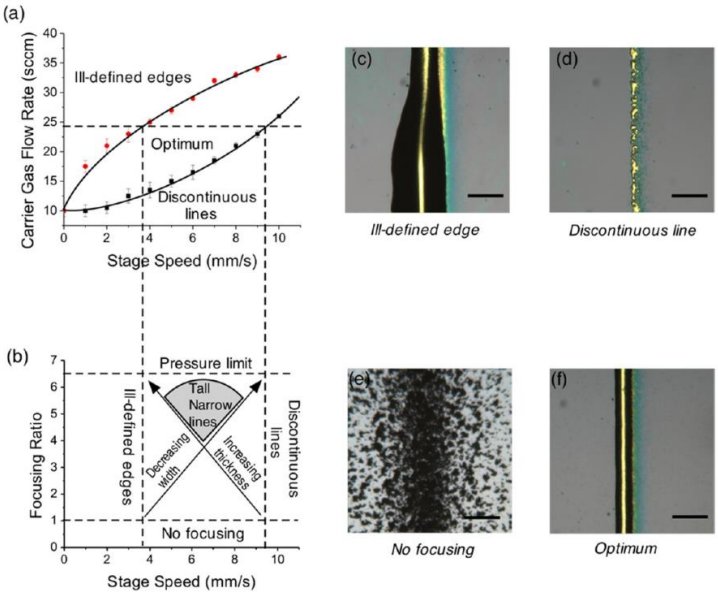

Figure 9: Aerosol Jet Processing Window [35]

Moreover, Seifert et al.[36] compared three basic deposition patterns between inkjet and aerosol jet printing and investigated their shape, width, and electrical conductivity

difference. Several characteristics between inkjet printing and AJP are summarized in Table 2.

Table 2: Characteristic comparison between Inkjet printing and Aerosol Jet printing [36]

characteristic	IJP	AJP
ink flexibility concerning particle material, particle loading, particle size, ink viscosity, and ink surface tension	↓	↑
ink consumption, including dead volume of the deposition system and "overspray"	↓	↑
suitability for thin layer deposition (considering a certain ink formulation as demonstrated in this contribution)	↓	↑
suitability for thick layer deposition (considering a certain ink formulation as demonstrated in this contribution and only one pass)	↑	↓
achievable layer thickness and layer width range (considering one nozzle and one pass)	↑	↓
edge sharpness of deposited layers	↑	↓
deposition velocity (in principle, based on the deposition mechanism comparing drop-on-demand IJP and AJP)	↓	↑
scalability of the deposition system, especially toward large area processing	↑	↓
flexibility concerning substrate materials and substrate topology (e.g., 3D substrates)	↓	↑
system costs considering single-nozzle deposition systems with similar features (e.g., concerning axis accuracy, etc.)	↓	↑

Although these studies addressed the concern of line quality, they were limited to qualitative descriptions of printed lines. In order to monitor, optimize, and eventually control the AJP process, it is critical to establish quantifiers for printed line quality. In this thesis, an image-based method was developed to extract several geometrical quantifiers, including line width, overspray, continuity, and density from microscope images.

2.3 Summary

In Chapter 2.1, we review current popular printed electronic technologies and discuss their basic working principles and applications in both research and industrial fields. Among these printed electronic technologies, AJP shows several unique benefits such as fine feature size, wide material selections, and conformal printing. It is also a digital manufacturing process that can direct fabricate different device design with CAD file. Therefore, it has been selected as our platform to develop applications in advanced sensing and manufacturing. However, there exists challenges in current printed electronic technologies and some of the challenges are specifically identified in the AJP process. Chapter 2.2 reviews current issues and state-of-art solutions in ink dispersion stability, ink substrate mismatch, and quality control.

CHAPTER 3. RESEARCH METHODOLOGY

3.1 Exploratory Device Application

The first section of this research are explored two device applications that use the unique capabilities of AJP process. The first application is a carbon nanotube ammonia sensor. Carbon nanotube (CNT) is a promising material for gas sensing due to its large surface area and high sensitivity and selectivity toward gas molecules. However, the manufacturing process suffers from the non-uniform drying effect (coffee ring effect) of CNT solutions, which is a major hurdle for a CNT-based sensor to be fabricated at an industrial scale. The AJP process provides an opportunity to eliminate the coffee ring effect due to very small sized droplets forming from the atomization process. The droplet size in the AJP process is usually around 0.001-0.005 pl. In contrast, the inkjet process usually has droplet sizes around 1-80 pl. By precisely controlling the substrate temperature, an AJP printed droplet can evaporate efficiently to minimize the coffee ring effect. Although the AJP process has advantages in reducing coffee ring effect, the droplet output volume changes when printing large sensor arrays, which results in variation in the sensing film thickness and resistance.

The second application is a printed 3D transmission line. The traditional desired fabrication for transmission line is the photolithography process. It is an expensive and complex process, and it is limited in material and fabrication facilities. In recent years, researchers have reported using inkjet printing for fabricating a 25 GHz transmission line. However, a fabrication limitation was found when fabricating transmission line structures at a D-band frequency (110 GHz and 170 GHz). At D-band frequency, the surface

roughness is comparable with the skin depth of printed conductors, which leads to large signal loss in the transmission. The AJP process can print 10-20 μm features with uniform layer thickness, which enables the opportunities to fabricate transmission line structure in D-band frequency. However, the control of the printed line morphologies is a challenge at the sub-100 μm printing. Overspray and edge roughness needs to be minimized along with precise line width control. Without comprehensively understanding the relationship between machine parameters and line morphologies, the yields of the device are very low.

Through the fabrication of the two novel devices above, we demonstrated that the AJP process: 1) lacks tools to monitor the stability of the process; and 2) lacks a knowledge base on the relationship between process parameters and printed line quality. Therefore, we developed a set of tools using industrial engineering knowledge to overcome the identified problems, which leads to our next research task.

3.2 Process Monitoring of AJP

The quality control issues of AJP have been brought up in several pieces of literature as discussed in the literature review. Several research groups have investigated the relationship between process parameters and line morphologies through a trial and error method, the design of experiments, and computational fluid dynamic simulation. However, these investigations usually assume that the underlying atomization process is stable and its droplet output is constant over time. However, it has been observed through experiments in fabricating exploratory devices that the status of the atomization changes over time. Furthermore, different inks result in a different atomization status profile due

to the ink viscosity, vapor pressure, and other physical properties. It is difficult to reuse the optimal parameters from the literature. What's worse, the parameters identified from previous experiments may have a different printing result. These drawbacks make operating the AJP printer heavily experience dependent and require immediate parameter adjustment from the operator. Furthermore, current assessments of printed line morphology are qualitative, not quantitative. In order to facilitate the modeling and process optimization, a quantitative method that characterizes printed line qualities is essential. To develop monitoring and quality assessment tools for the AJP process, a systematic approach was used.

First, a vibration-based atomization process monitoring platform was developed for observing the atomization status from vibration signal. An aerosol particle analyzer was used to measure the particle size distribution and mass density for validating the effectiveness of the previous vibration based monitoring platform. From the atomization process monitoring, the process time window can be estimated for different inks and machine conditions. This also serves as a benchmark that ensures the stability of the atomization process when conducting design of experiments to find optimal machine parameters.

An image-based method for line feature extraction was also developed for establishing quantitative output. Three major features are evaluated: line width, line edge roughness, and overspray index. Different device applications require different printed line conditions. For example, the line width is critical for strain sensor application because it directly affects the conductivity of the sensor. On the other hand, thin film transistor usually involves tiny gap (<30 μm) between source and drain electrodes which requires

minimizing the overspray index to prevent potential short circuit. The image-based line feature extraction method not only provides the quantitative outputs that facilitate building the optimization models but also has the potential to be integrated into the AJP process to provide real-time quality information. Once we can effectively monitor the atomization process, the droplet output variation can be minimized. Optimization of the AJP machine parameters can be evaluated through a design of experiments method. From here, two important factors are investigated, 1) the stable process time from atomization monitoring, and 2) the machine parameters that meet the target line width or minimize the overspray.

3.3 Novel Processing Methods

Although aerosol jet printing has demonstrated its capabilities in various flexible electronic applications. There is still a need to develop a new processing method of AJP for emerging areas such as nanocomposite fabrication, 3D printing, and biomedical applications. In the third task of this research, two novel processing methods are introduced to further extend AJP capabilities to new research areas. In the first section, we introduce a facile method that integrated printed sensors into 3D printing objects. 3D printing has drawn a lot of interest in both industry and academia in recent years. This capability brings freedom to the process of designing and fabricating complex geometric structures. However, 3D printing applications are mostly limited to passive mechanical components without built-in functionality. However, there are some challenges that hinder the integration. A major challenge of depositing conductive inks onto 3D printed parts is the need for a high level of surface roughness. For most 3D printing processes, especially the extrusion-based process such as FDM, small ‘trenches’ are formed in the

direction the printer is moving across the surface. When liquid inks are used, the ink spreads into the trenches under the capillary effect and causes wicking. Additional surface polishing is usually required before depositing conductive inks. Another challenge in using conductive inks is the elevated sintering temperature required for most situations. Most polymeric materials have heat deflection and glass transition temperatures that are below the optimal sintering temperature required for the printing process. Lower sintering temperatures result in high electrical resistivity of printed features, which is undesirable for most applications. We developed a facile method called the print-stick-peel (PSP) process that overcomes the above-mentioned challenges. The PSP process does not require any fabrication on the target 3D-printed substrate, so it circumvents the fabrication challenges of surface roughness and sintering temperature. The printed patterns are first printed on a low surface energy substrate that has a high glass transition temperature. Then the printed patterns are sintered at a desired temperature. Finally, the conductive patterns are transferred on using the self-adhesion of 3D-printed structures or additional adhesives. This new method takes advantage of both AJP and 3D printing. It also provides a practical manufacturing technique for making multifunctional smart structures.

In the second section, a novel dual material fabrication method was developed for conductive tailorable nanocomposite fabrication. Conventional methods for manufacturing nanocomposites require dispersing conductive nano-fillers (e.g CNT and carbon black) into polymeric solutions. However, the process is a challenge because even a small percentage of CNT would greatly increase the viscosity of the polymeric solution. Worse yet, dispersion-based fabrication often yields a heterogeneous distribution of

CNTs in the polymer matrix due to its tendency to agglomerate in the solution. Performance improvement with inserted CNTs is limited by the low loading and poor homogeneity of the polymer matrix. This represents the current bottleneck in creating high-performance conductive nanocomposites. We demonstrate a novel fabrication method of conductive nanocomposite that is based on dual-material AJP (DMAJP). The demonstrated DMAJP fabrication method of nanocomposite bypasses the challenging dispersion process that hinders conventional fabrication methods when using commercially available CNT and polymer solution products as raw materials. In addition, atomization, aerosol mixing, and aerosol deposition are all potentially scalable. Thus, this relatively facile, cost-effective fabrication method is a promising option that can be adopted by industry level, full-scale manufacturers. Moreover, the additive nature of AJP grants it unique advantages over existing methods. Such advantages include the ease of patterning, affiliation with mass customization, high feature resolution, and designable, varying intra-part CNT loading levels, etc.

In summary, the research structure of this thesis is depicted in Figure 10. Starting from exploratory device applications, two novel devices were fabricated to demonstrate the unique capabilities of the AJP process. At this stage, key challenges in process control were also identified. The next stage was to develop process monitoring tools and apply process optimization methods to overcome the identified limitations. Finally, two novel process methods were developed to extend the AJP capabilities into emerging advanced manufacturing areas.

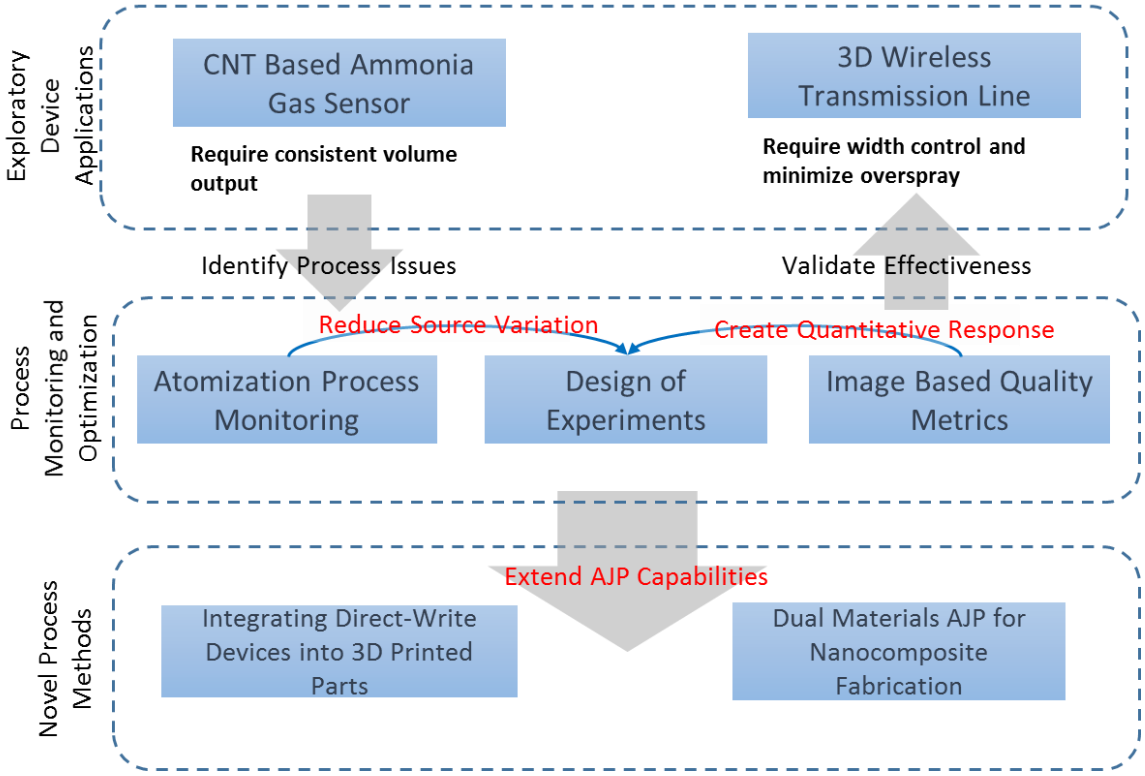

Figure 10: Thesis Research Structure

CHAPTER 4. EXPLORATORY DEVICE APPLICATIONS

4.1 Overview

In chapter 4, two exploratory device applications are presented. The first application is a carbon nanotube-based (CNT) ammonia gas sensor printed using the AJP process. The benefit of using the AJP process for printing CNT-based material is that it can dramatically minimize the coffee ring effect, which renders uniform printed sensing film. However, there are a quality issues when printing multiple layers that take a longer time. We identified the root cause for this problem, which is the instability of the atomization process. In Chapter 5, we developed a vibration-based online monitoring method to address this problem. The second application is a high frequency D-band transmission line fabrication. The dimension of D-band transmission line is usually less than 50 μm which is challenging for traditional printed electronic methods. We successfully fabricated a multilayered D-band structure with the minimum dimension of 10 μm using the AJP process. It is still a challenge to control AJP printed line width with such a small tolerance. Other fabrication challenges, such as overspray and edge roughness, also need to be considered. We adopted a design of experiment (DoE) method to investigate the relationship between process parameters and printed line quality and a way for the printed process to be effectively controlled. Detail results for quality index and the DoE method will be discussed in Chapter 5.

4.2 Carbon Nanotube-based Ammonia Gas Sensor

4.2.1 Introduction

Ammonia gas sensing is required for many applications, including industrial monitoring, environmental control, and toxic gas detection on the battlefield. In the past decade, carbon nanotubes (CNTs) became a promising sensing material for researchers due to their excellent electrical and mechanical properties, and in particular, their large surface area that can increase the contact of gas molecules. Gas sensors based on CNT sensing film can provide high sensitivity, high resolution, and fast response compared to traditional semiconductor gas sensors.

Although CNTs possess many superior properties for gas sensing, the transducer industries have not yet widely adopted their use because of the complexity of the manufacturing process of CNT-based gas sensors. Currently, there are two major methods for employing CNT as a gas-sensing layer. The first is an as-grown method to directly grow CNTs on the sensing platform through chemical vapor deposition (CVD). The CVD method consists of complex and time consuming processing steps. And, because of its production rate, it is hard to meet industry demands. The other method is direct depositing the CNT solution through a micro-pipettor, spray coater, or inkjet printer. This depositing method is simple and scalable. However, there are issues in terms of repeatability due to the drying mechanism involved in the solution process. The drying step causes a phenomenon called the coffee ring effect. The coffee ring effect is a pattern left by a puddle of particle-laden liquid after it evaporates, and is so named because it resembles the characteristic ring-like deposit left by a wet coffee mug. The pattern forms

because of a capillary flow induced by the differential evaporation rates across the drop. These drawbacks result in variations in device performance and properties from batch to batch, making sensor characterization difficult. Therefore, several researchers have put their efforts towards reducing the coffee ring effect by, for example, using surface treatment, changing solution content, or manipulating particle shape, etc. However, these methods cannot fundamentally solve the drying problem because there are many different substrates and nanoparticle solutions available in the application. The AJP process provides an opportunity of eliminating the coffee ring effect because of the small size of the droplets it forms in the atomization process. The droplet size in the AJP process is usually around 0.001-0.005 pl. In contrast, the inkjet process usually has droplets sizes around 1-80 pl. By precisely controlling the substrate temperature, an AJP printed droplet can be evaporated efficiently to minimize the coffee ring effect. Although the AJP process has advantages in reducing coffee ring effect, the droplet output volume is not stable. It has been observed from our past experiments that the droplet output volume drifts when printing large sensor layouts. CNT-based sensors require multiple passes to deposit sensing materials. Therefore, a long processing time is needed. This results in variations in the sensing film thickness and resistance. Monitoring the atomization process provides information about the duration of a stable processing time, which can reduce variations in performance. In this section, a CNT-based sensor was fabricated and performance was demonstrated. The printed sensors show excellent sensing properties for ammonia gas and should be able to detect very low concentrations of ammonia.

4.2.2 Experiment Setup

The electrodes for the sensor platform were fabricated with a micro-fabrication technology placed on a silicon wafer. First, the photo-resist (SU8) was spin-coated on the substrate to define the electrode area after photolithography. Then the adhesion layer and the gold electrode layer were sputtered on the wafer. Finally, the electrode arrays were fabricated with a lift-off technique. The gap distance between electrodes was ~15 μm. An image of the sensor platform is shown in Figure 11.

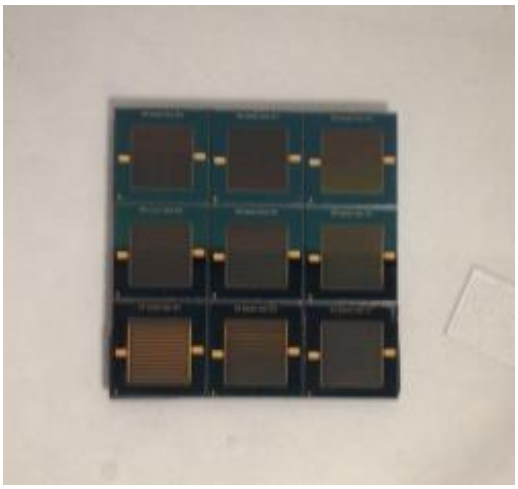

Figure 11: Interdigital sensor platforms on silicon wafers

The dispersion of carbon nanotubes was prepared using the following steps. Poly(m-aminobenzene sulfonic acid) single wall nanotubes (SWNT-PABS) was used for the gas sensing material. SWNT-PABS is a water-soluble nanotube-polymer compound, formed by covalently bonding the polymer (PABS) to SWNTs via amide functionalization. The SWNT-PABS in powder form was purchased from Carbon Solutions Inc., Riverside, CA. The aqueous dispersion of SWNT-PABS was prepared by dispersing ionic water with a concentration of 5mg/ml. Subsequently, the suspension was sonicated using an ultrasonic

bath for four hours. The SWNT-PABS dispersion was deposited onto the electrode area by the AJP process. A uniform network of SWNT-PABS bridged the electrode gap after the solution evaporated.

4.2.3 Results and Discussion

4.2.3.1 The Coffee Ring Effect

The coffee ring effect is undesirable for devices fabricated by a solution method. It is very difficult to eliminate by traditional solution casting methods. The AJP process provides an opportunity to eliminate the coffee ring effect because the atomization process produces small sized droplets. By precisely controlling the substrate temperature, an AJP printed droplet can evaporate efficiently and minimizes the coffee ring effect. Therefore, the printed SWNT-PABS can form a homogeneous network between electrodes. Figure 12 shows the difference between the SWNT-PABS ink on the wafer after evaporation by using an inkjet and AJP process. Severe agglomerated particles are observed on the substrate that used the inkjet method. On the other hand, the AJP printed sensing film shows a homogeneous distribution of the SWNT-PABS network.

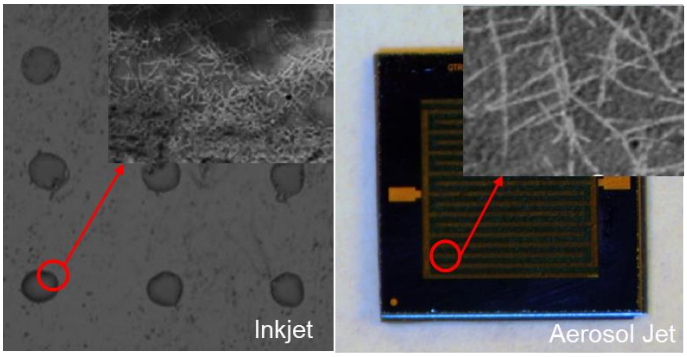

Figure 12: Comparison of coffee ring effect between inkjet and aerosol jet

4.2.3.2 Layers and Resistance

To study the effect of printed layers on the electrical performance, 10 samples with different printed layers were prepared. Figure 13 shows the electrical resistance of the sensors by different numbers of SWNT-PABS printed layers. The electrical resistance ranges from 10^6 to 10^2 ohms. The resistance decreased significantly with the increase in the number of printed layers. After 12 printed layers, the resistance is around 800 ohms and there is no significant resistance decrease when depositing more layers. The variation of the resistance also increases with more printed layers. That occurs because multiple layers require longer processing time, which exceeds the ideal process time. Therefore, the droplet output was degraded resulting in resistance variation.

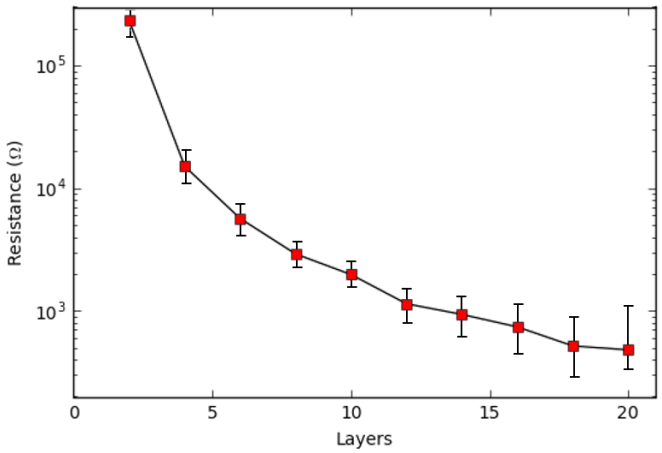

Figure 13: Resistance versus a different number of printed layers

4.2.3.3 Sensor Performance

To demonstrate the performance of the SWNT-PABS gas sensor, we examined the response of the sensors to different concentrations of NH_3. The resistivity response of the gas sensors was tested with a data acquisition board (NI-9219) (National Instruments

Corp.), which sent the resistance reading to a computer and displayed it in a LabVIEW program. Different concentrations of NH_3 gas in parts per million (ppm) range was released into the testing chamber. The resistance of the printed sensor increased along with each step increase in the NH_3 concentration as shown in Figure 14.

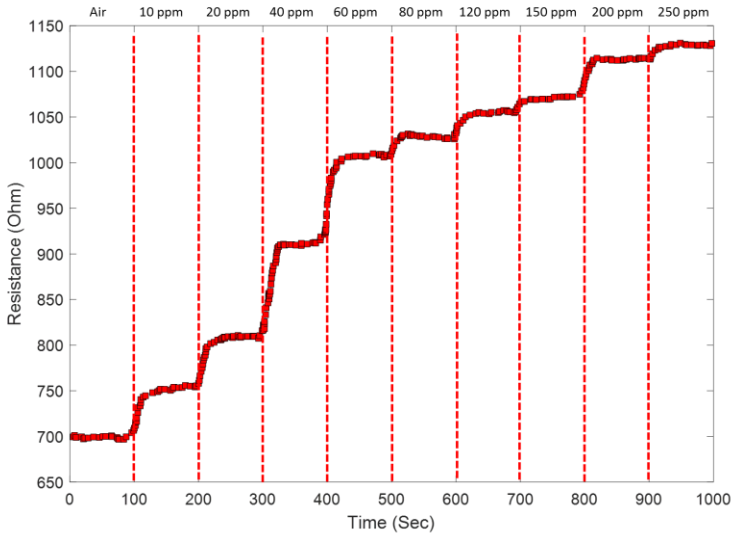

Figure 14: Resistance response in different ammonia gas concentrations

The baseline resistance is measured under dry compressed air and the recorded resistance is around 700 ohms. The resistance increased to 1100 ohms when the NH_3 concentration was 200 ppm. The sensors showed a fast response time and recovery time that was around 90 seconds. The sensitivity of the sensor is determined by a function of deviation of resistance change upon baseline resistance as shown in equation 1:

$$S = \frac{R_g - R_0}{R_0} \tag{1}$$

where S is the sensitivity, R_g is the sensor's resistance under NH_3 and R_0 is the sensor's resistance under dry air. Figure 15 shows the sensitivity under different NH_3

concentration. The sensitivity shows an almost linear response at concentration range 10 ppm to 100 ppm. At a higher concentration range (>100 ppm), the sensitivity is saturated.

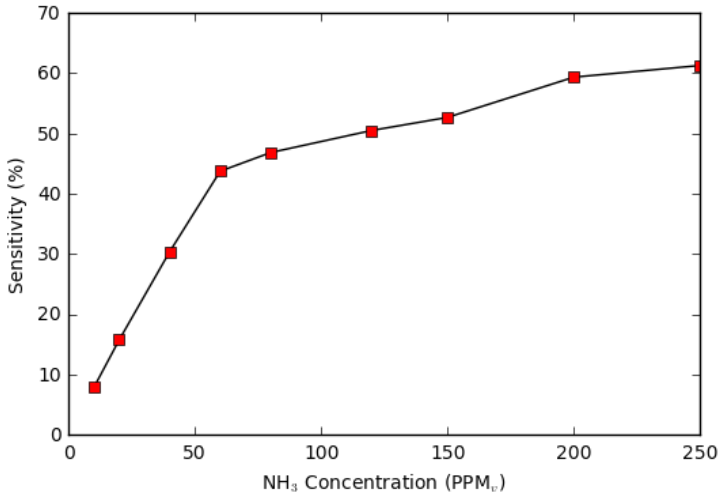

Figure 15: Sensitivity of gas sensor in different ammonia concentration

4.2.4 Conclusion

We demonstrated a reliable approach to fabricating ammonia gas sensors with SWNT-PABS. The sensor shows excellent sensitivity toward low concentration NH_3 gas. The variation in sensor performance regarding resistivity was reduced by 48% by controlling the printing in the best operation window. The response of the fabricated sensors was rapid and reversible. The sensors could be useful for various applications. This process of printing reliable sensors has the potential to be scaled up and meet the industrial requirements.

4.3 Low-Loss 3-D Multilayer Transmission Lines and Interconnects Fabricated by AJP

4.3.1 Introduction

Additive manufacturing technologies have been progressively expanded into RF applications during the last decade. Up to now, additive technologies have been reported in literature for the fabrication of low-frequency passive circuits, as well as active components, including antennas [37], [38], inductors [39], and sensors [40]. Packing technologies in 3D structures for multichip modules are extremely important in millimeter (mm)-wave systems. With the development of advanced monolithic microwave integrated circuits (MMICs), there is optimism about being able to achieve the heterogeneous integration of different technologies (logic, memory, RF, analog, MEMS, etc.), which are enabled by high-performance and compact system-in-package or system-on-package (SOP) solutions.

However, there are several challenges remaining in the formation of via-holes, substrate thickness uncertainty, and misalignment of multilayer stacks that limits the applications in single-layer interconnections. There is little comprehensive research on vertical interconnections through the use of additive manufacturing. Liang et al. [41] reported on a microstrip line (MS) structure with vertical transition through vias with a diameter of 2 mm. Lopes et al. [42] reported on a 3D packaging structure by a combination of FDM and microdispensing to achieve crossover interconnection.

On the other hand, mm-wave and sub mm-wave applications, where accuracies down to 10-20 μm are typically required [43], place strict constraints on acceptable tolerances of

the printing technologies. To date, the minimum linewidth of inkjet printing is around 25 μm due to nozzle technologies [44]. However, there are bottlenecks in finding ways to reduce the dimension of the nozzle. What is more, the clogging issue that happens during the operation of inkjet printers is disrupting mass manufacturing processes. Although some reports have solved some of the fabrication issues, so far there isn't any literature that addresses all of the stringent requirements [45, 46]. Therefore, highly accurate and cost-effective fabrication of mm-wave circuits by additive printing technology is still very challenging.

AJP provides an alternative method in overcoming these limitations, providing fine resolution, multifunction for multilayer stacking, self-alignment, and wide material options. AJP has been proven effective in fabricating passive electronic components such as resistors, capacitors, antennas, sensors, and thin-film transistors. Components can also be printed onto 3D surfaces, eliminating the need for a separate substrate, and thereby reducing the size, thickness, and weight of the end product [47].

In this section, the AJP technique is used to demonstrate 3D multilayer transmission lines and interconnects with embedded vias up to 40 GHz with a high resolution. Dual materials, i.e., silver ink and polyimide, are printed with AJP to form a complete 3D structure. The materials and fabrication process are reported. This work demonstrates the feasibility of RF/mm-wave multilayer front-ends with vertical interconnects through multilayer stacking by the AJP printing technique.

4.3.2 Fabrication

As one of the additive manufacturing fabrication methods, AJP can dramatically reduce costs compared with traditional lithography methods. The AJP-based fabrication is carried out under atmospheric conditions, thus, eliminating the need for expensive clean room facilities and expert laborers, all of which have major impacts on the total cost. Besides, it uses an additive fabrication process that deposits materials only on desired areas, thus, reducing waste produced in traditional IC and microelectromechanical system fabrication. The general operation principle of the aerosol jet process is already described in Chapter 2. AJP is compatible with a wide range of materials options, including dielectric, semiconductive and conductive inks. The other unique capability is that AJP can process dual materials with a single machine setup. In addition, AJP also provides a high level of accuracy with layer thickness control and designers do not need to rely on the available substrates in the market. This gives much more flexibility to design 3D structures on demand, e.g., creating non-uniform thickness substrate, vias, and cavities. Furthermore, this machine benefits multilayer printing in terms of its inherently accurate alignment function that can be controlled within 1 μm.

A silver nanoparticle suspension in hydrocarbon solvent was purchased from UT Dots with 25–60 wt% silver nanoparticle in hydrocarbon solution. The polyimide is 15%–16% pyromellitic dianhydride-co-4, 4’-oxydianiline (poly) in N-methyl-2- pyrrolidone (NMP) solution, and additional NMP solution is mixed into this solution with 2:1 ratio. After fully curing, the dielectric constant of polyimide is 3.5 and the loss tangent is 0.008. The minimum feature sizes and the thickness accuracy by AJP are 80 μm with polyimide and 10 μm with silver ink. Each printed layer is 0.65 ± 0.05 μm. The surface roughness of

polyimide does not increase linearly along deposition layers. When printing a polyimide layer with a thickness of less than 5 μm, the surface roughness was less than 0.5 μm, while the surface roughness was approximately 2 μm for 60 μm-thick polyimide.

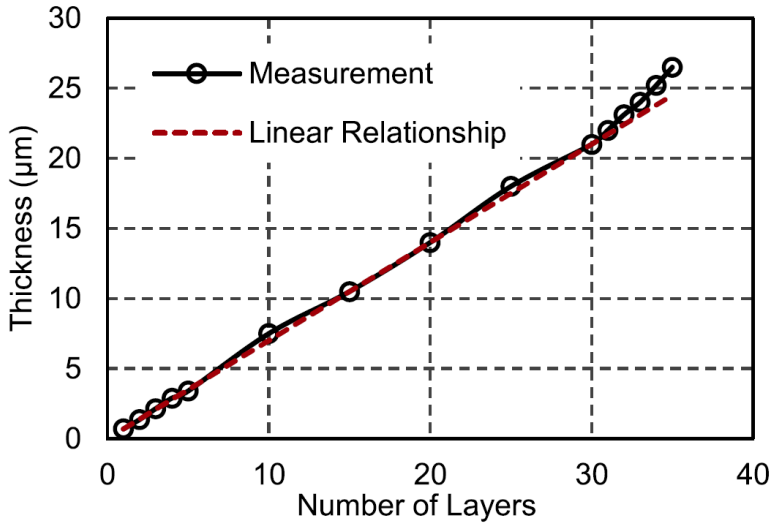

Figure 16: Relationship between the thickness and the number of printed layers

Figure 16 shows that the linear relationship between the thickness of the polyimide and the corresponding number of layers cannot be kept beyond 30 layers. This is because the thick sample prevented the solvent from escaping. Therefore, a process to fully cure the sample is required with each 20 μm polyimide (30 layers). On the other hand, a detailed curing condition analysis for the silver ink is given here since the resistivity of the silver ink determines the final RF performance. The silver ink could be either cured in an oven or by the laser embedded in the AJP system for consecutive printing tasks. In this work, the curing step was performed in an oven. Its sheet resistance was measured by a four-point probe method with a Keithley 2400 source meter. The relationship between the sheet resistances of the silver ink versus various numbers of layers at a curing

temperature of 150 °C is given in Figure 17 (a). It indicates that the resistance became relatively stable after 60 minutes of curing. Figure 17 (b) shows the relationship between the sheet resistance and the temperature after 60 minutes of curing, and it was found that the silver ink became fully cured when the temperature was higher than 150 °C. These curing tests set the curing conditions: the samples were kept in an oven at a temperature of 200 °C for an hour for the circuit fabrication. After the silver ink was fully cured, the sheet resistance was found to be 0.03 Ω/□. The conductivity of the silver ink is 5.13×10^6 S/m, which is less than 10% of that of the copper. The interconnects with a feature size of 10 μm on the LCP substrate and nonplanar plastics ABS are also shown in Figure 18. This indicates that such a fine feature size pattern has great flexibility on a number of substrates. The printing time depends on the pattern area. For the conductive traces, it takes ∼1 min/layer. For the substrate by polyimide and the ground by silver ink, it takes ∼5 min/layer. Figure 19 shows via-holes formed by AJP with a hole pattern in AutoCAD. First, a layer of silver ink was printed. Then 100 μm-thick polyimide was printed layer by layer with the via-hole area empty. Afterward, the silver ink was deposited into the via-hole area to fill the vias. It indicates that the outer diameter of the holes is close to the pattern as 500 μm with a deviation of less than 2%. The overspray of the polyimide merges vias, and the inner diameter of the vias is 150±10 μm. The inner diameter of the vias depends on the thickness of the deposition and printing parameters such as printing speed, temperature, and sheath gas flow rate. These are the reasons that it is necessary for a processing control approach to achieve the vertical interconnection when the width of interconnection is in the order of 10 μm.

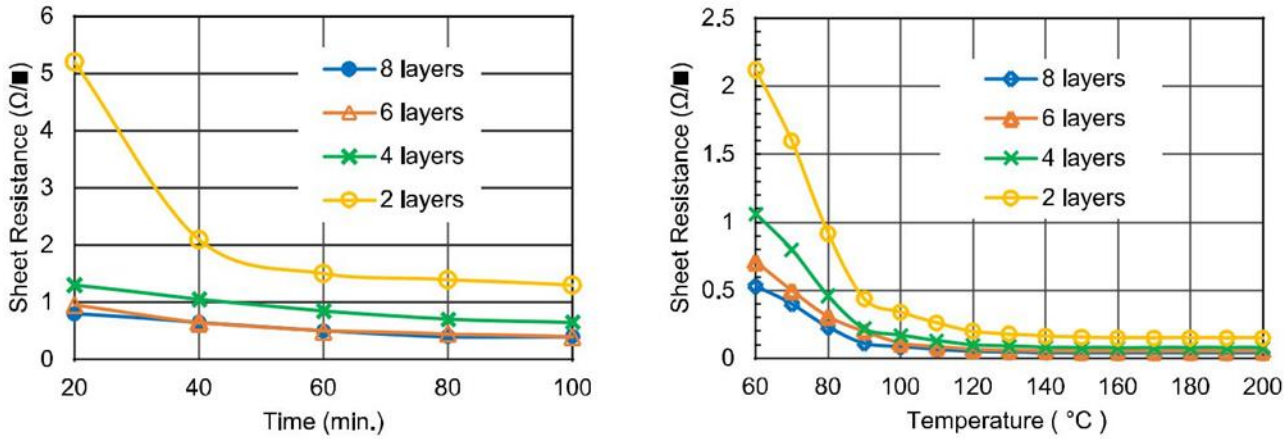

Figure 17: (a) Sheet resistance of the silver ink with a various number of layers versus the curing time at a temperature of 150°. (b) Sheet resistance of the silver ink with a various number of layers versus the curing temperature after 60 min of curing

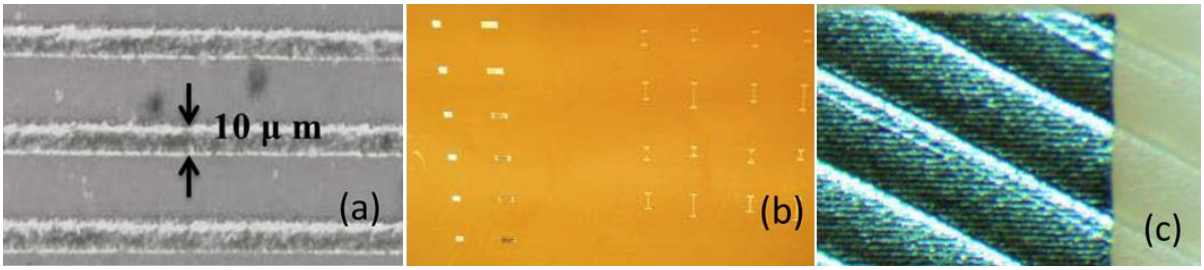

Figure 18: Photographs of the printed single-layer silver ink transmission lines and the printed pattern on (a) glass [48], (b) LCP [48], (c) ABS

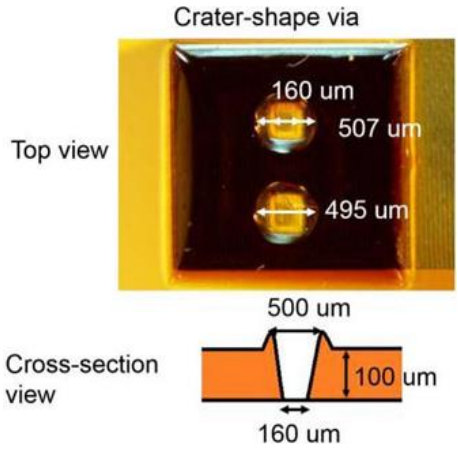

Figure 19: Microscope image of the hole formed by the AJP technique

4.3.3 Design of Transmission Line

To measure samples with RF probes, a CPW-to-MS-to-SL transition was designed. Multiple layers were stacked for interconnect routing, and the structure was detailed (See Figure 20 (a). The whole structure consists of five layers, including two transitions: CPW-to-MS and MS-to-SL. The dimension values of CPW, MS, and SL are calculated by the LineCalc in Agilent advanced design system (ADS). In the CPW-to-MS transition section, the width of the CPW signal strip (90 μm) is gradually increased to match the width of the MS (110 μm). At the same time, the gap between the ground planes and the signal line is widened to retain a 50Ω characteristic impedance to avoid sharp discontinuities and minimize reflections [49]. This transition is a planar transition with the signal line continuing on the same plane. To provide vertical interconnection, the MS-to-SL transition is developed. Instead of the 90° vertical via conventionally deployed in [50] and [51], the proposed one in Figure 20: (a) Multilayer interconnect structure. (b) Details of the vertical transition from SL to MS line consists of an inclined metal sheet tapering from 110 μm (the width of the MS signal line) to 19 μm (the width of the SL signal line).

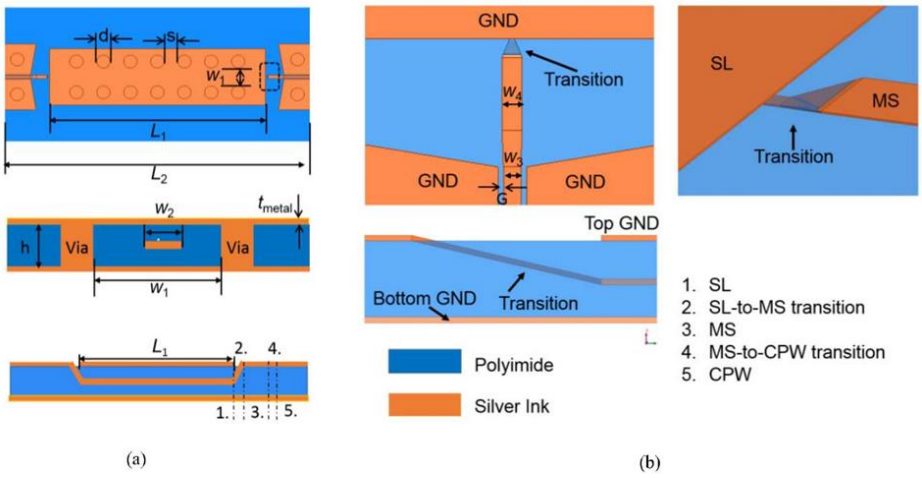

Figure 20: (a) Multilayer interconnect structure. (b) Details of the vertical transition from SL to MS line

The fabrication process to build this multilayer structure is described in Figure 21. First, a silver ink layer as layer 1 was printed as the bottom ground followed by layer 2 constituting polyimide. The two sides of layer 2 were 40 μm thick and served as the overall substrate for the MS and CPW. The recessed cavity in the middle formed half of the substrate for the SL part. When printing the recessed cavity, the slope at the edge of the two sides was naturally formed due to the overspray of the polyimide ink and the liquid status before curing. Then, layer 3 was printed with a uniform thickness and formed a continuous coverage over the slope. The signal line of the SL was sandwiched by layers 2 and 4. Accordingly, the MS-to-SL transition was embedded in the polyimide. As mentioned in the previous section, the minimum diameter of preprinted holes by polyimide is 160 μm, but in order to have a good match for the transition, the diameter has to be around 20 μm. Furthermore, to achieve a high aspect ratio, proper via metallization has to be achieved. With the capability of printing a nonplanar surface substrate by AJP, this 3-D transition was possible. Finally, layer 5 was deposited as the

top ground, filled the printed holes previously fabricated by silver ink, and connected with the bottom ground. After the deposition of each pattern is finished, the samples were kept in an oven at a temperature of 200 °C for an hour for the circuit fabrication.

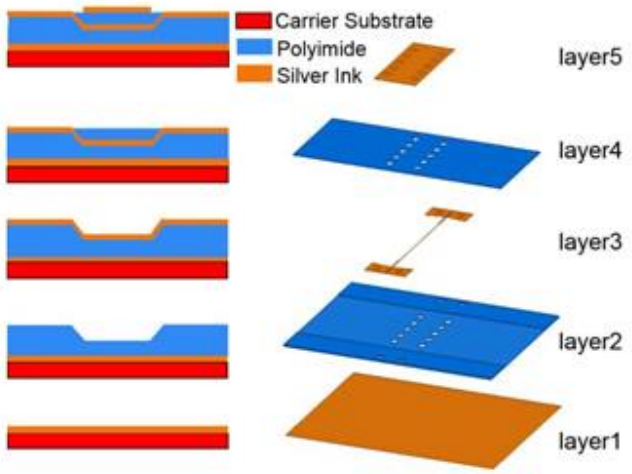

Figure 21: Fabrication process of the multilayer interconnect

The dimensions of the entire structure are summarized in Table 3 where *d* is the diameter of the vias connecting the top and bottom ground planes, and *s* is the spacing between the vias. The parallel-plate mode and the coupling of electromagnetic radiation onto digital/dc lines is suppressed with via fences connecting the two ground planes, which provides a natural shielding against incoming spurious signals in the circuit routing. A spacing of $s < 5d$ is required to prevent a potential difference from the ground planes [52], and W1 determines the frequency at which higher order modes will be excited. W2-W4 are the widths of the signal lines in SL, CPW, and MS, respectively, and G is the gap between the signal line and the ground for the CPW section. Note that the selected values of *d*, *s*, and *h* are based on the availability from manufacturing restrictions. The substrate thickness *h* is selected based on the maximum thickness without an internal curing step; *d*

and *s* are chosen to avoid the vias merged by polyimide printing. With the aid of these values, the characteristic impedance of the SL is calculated as follows [53]:

$$Z_0 = \frac{30\pi}{\sqrt{\varepsilon_r}} \frac{h}{W_e + 0.441h} \tag{2}$$

where W_e is the effective width of the center conductor and h is the height of the substrate. Z_0 is designed as 50 here.

Table 3: Summary of geometry

	Design (μm)	Fabrication (μm)	Deviation (%)
D	500	497±8	1.6
S	500	505±6	1.2
H	40	38±4	10
T	3.5	3±5	166.67
G	30	28±6	20
W1	1300	1295±8	0.615
W2	19	19±3	15.78
W3	90	88±4	4.44
W4	110	109±6	5.45
L1	8000	80000±10	0.12
L2	11400	11400±8	0.07

4.3.4 Fabrication Challenges

Interconnect techniques play a key role in microwave/mm-wave modules, especially as the frequency of operation increases. At higher frequencies, transmission lines and interconnection schemes that minimize crosstalk, insertion loss (IL), and radiation while maintaining wideband performance are required. As one of the most important transmission lines, Stripline (SL) provides better performance in terms of higher isolation and less crosstalk and radiation than its counterparts, e.g., Microstrip (MS) and Coplanar line (CPW), because of their nondispersive nature based on TEM mode and shielded

structure. Therefore, it is often required in the multilayer routing for microwave circuits. However, it correspondingly gives rise to tighter manufacturing tolerances for a dense design with smaller traces. Therefore, fabrication challenges added in precisely can control the line width as well as the line overspray.

4.3.5 Measurement

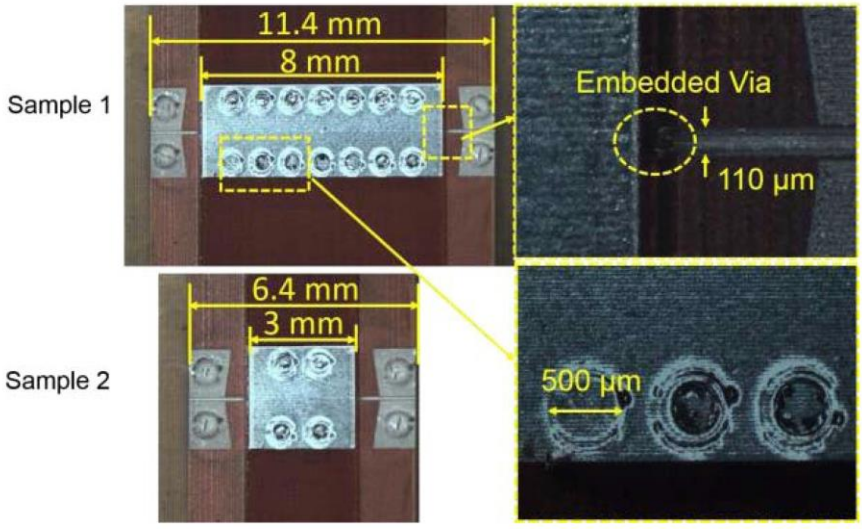

Figure 22: Fabricated prototypes and details of the vias

Figure 22 shows two fabricated samples for performance measurement. Sample 2 is used to de-embed the loss from CPW pads and transitions. An Agilent 8517B vector network analyzer is used to perform S-parameters' measurements and 250 µm pitch GSG probes are used with a SOLT calibration. The reference planes are located at the feeding CPW pads. The measured S-parameters of the fabricated prototypes are shown in Figure 23 along with the simulated results. A good match is achieved below 40 GHz for both

samples. The simulation is based on the designed dimensions with 1.5 μm surface roughness in ANSYS HFSS for all printed metal segments. Measurements show an IL of 1.2 dB at 1 GHz and 6.3 dB at 40 GHz for the 11.4-mm sample. Compared with the longer sample, the IL of the 6.4-mm sample is 0.9 dB at 1 GHz and 3.6 dB at 40 GHz. Note that this IL is a combination of the losses from the SL, CPW pads, MS lines, and transitions. Considering the shorter sample as a back-to-back configuration and the long side of the longer sample as the standard one with a delay line, the chain transmission matrices of the two samples can now be expressed by:

$$T_{\text{standard}} = (T_A) \cdot (T_{delay}) \cdot (T_B) \tag{3}$$

$$T_{\text{back-back}} = (T_A) \cdot (T_B) \tag{4}$$

$$T_{delay} = \begin{bmatrix} e^{-\gamma L} & 0 \\ 0 & e^{-\gamma L} \end{bmatrix} \tag{5}$$

where T_A , T_B , and T_{delay} represent the matrices for A, B, and delay of the SL in Figure 24 (a). Based on the very small fabrication errors (less than 5 μm) on the dimensions of the MS and CPW lines, the change in the characteristic impedance is negligible. Thus, assuming that where T_A , $T_{A'}$, T_B , and $T_{B'}$ are the same, the IL of the SL is extracted by subtracting the S_{21} of two prototypes and the result is shown in Figure 24 (b). For the AJP-fabricated SL, the extracted line loss is around 0.03 dB/mm at 1 GHz, 0.33 dB/mm at 30 GHz, and 0.53 dB/mm at 40 GHz. Compared with the measured loss of 0.62 dB/mm at 30 GHz on a 17.3-μm polyimide substrate and the calculated loss (with ADS LineCalc) of 0.2 dB/mm at 30 GHz based on a 40-μm-thick polyimide in [54], the AJP-fabricated SL compares very well providing almost identical loss values.

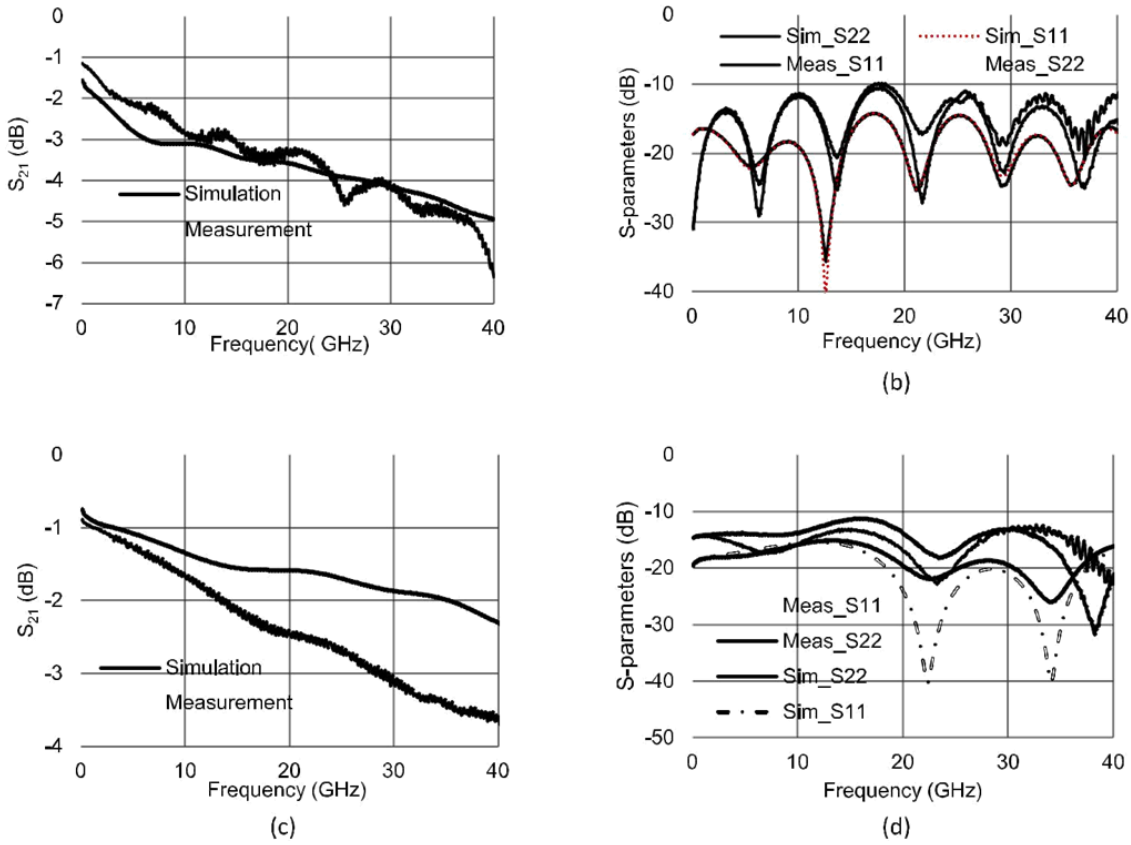

Figure 23: (a) and (b) Measured and simulated S-parameters of sample 1 with a total length of 11.4 mm. (c) and (d) Measured and simulated S-parameters of sample 2 with a total length of 6.4 mm

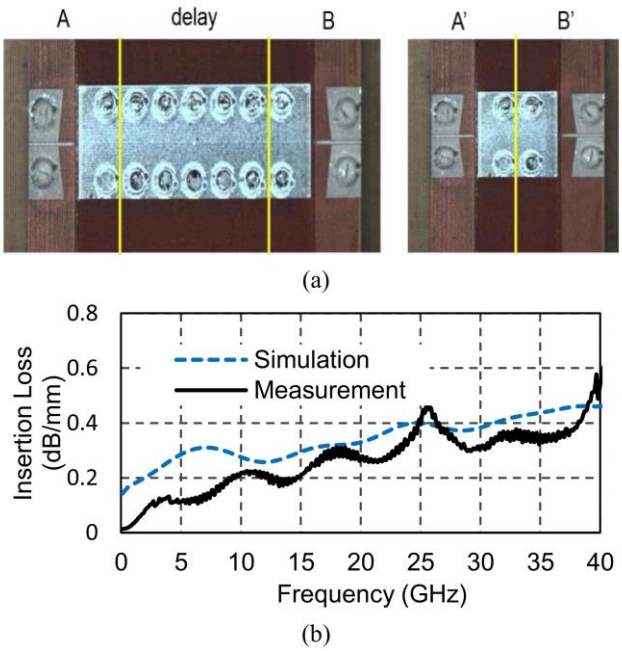

Figure 24: (a) Two samples with the de-embedded position marked in yellow. (b) Extracted IL of the SL

Using the measurements, the extracted results show deviation only from the simulation. Since the yield of each sample had a variation in the surface roughness, the less IL of the extracted SL does not mean it had less loss, but rather a deviation from the simulation. To reduce the IL, the surface roughness issue can be improved by using the silver ink with a dilution solvent, as well as further optimizing the fabrication parameters. The limited thickness of the lines is another reason for the high dc loss. The signal lines are around 2-µm thick and are limited by a high spatial resolution. While AJP is able to make the width of 20-µm-wide lines up to 10-µm thick, only one position short of the gap in CPW lines can cause the sample to fail. Thus, the lines are relatively thin here to guarantee a 30-µm-wide gap. The top and bottom grounds are up to 3.5-µm thick in order to improve the conductive loss. This thickness cannot be increased by AJP at this time because thicker silver ink has a higher surface roughness that is several times the skin depth [47].

However, compared with other reported works using additive manufacturing techniques, this provides an improved performance. A comparison of the printing resolution is listed in Table 4. While AJP provides a better resolution than inkjet printing, it is a competitive technique compared with other advanced fabrication processes [45] with regard to the simple fabrication flow.

Table 4: Printing resolutions by additive manufacturing technologies

	Technology	**Minimum Width**	**Minimum Slots**	**Thickness**
[55]	Inkjet Printing	118 μm	32 μm	118 μm
[56]	Inkjet Printing	100 μm	100 μm	5 μm
[57]	Inkjet Printing	59 μm	50 μm	N/A
[45]	CPLoP	5-70 μm	N/A	2 μm
This work	Aerosol Jet Printing	10 μm	10 μm	2 μm

4.3.6 Conclusion

Using AJP as a digital deposition method, printed multi-layer interconnects with vertical transitions are demonstrated and characterized up to 40 GHz for the first time. In this application, we assess the availability of the printed materials for RF applications, investigate the process conditions of various materials, and design multiple interconnects with vertical transitions. Multilayer interconnects are measured up to 40 GHz showing competitive RF performance. Fine-pitch size of a single line is demonstrated as small as 10 μm for silver ink and 80 μm for polyimide. With process control capability, both the completion rate and dimension deviation are improved. The embedded via with a slope achieved a width as small as 19 μm through a 20-μm-thick polyimide, and the proposed fabrication process indicates the potential to achieve higher aspect ratio embedded vias.

The polyimide-based SL loss is extracted to be around 0.33 dB/mm at 30 GHz and 0.53 dB/mm at 40 GHz. A good match is achieved from dc to 40 GHz as the accurate fabrication enables the 30 μm gaps with an error of less than 5 μm. This application paves the way for digital printing as a promising technology for mm-wave applications and indicates a fast and cost-efficient method to design complex 3-D structures in the future.

CHAPTER 5. PROCESS MONITORING OF AJP PROCESS

5.1 Overview

The aerosol jet printing (AJP) process is a multistage process that includes atomization, deposition and post-sintering. Process monitoring is a challenge because the print quality can be affected at different stages (atomization, deposition, and post-sintering). Printed line morphology is the most discussed quality response in literature on AJP. Several researchers have investigated the influence of process parameters at the deposition stage, as well as developing computational fluid dynamic models for deposition prediction. However, these investigations are based on the assumption that the source, or the atomization process, is stable over time. In reality, the atomization process drifts from time to time and the rate of drifting varies in relation to ink composition. This makes it difficult to reuse the optimal process parameters, or results from literature or past experiments. There is a need to develop a process monitoring technique that provides stable information about the atomization process. In this way, the subsequent process parameter optimization can be repeated and adopted for actual application. This chapter covers our attempt to develop a vibration-based atomization monitoring technique to provide real time information about the process stability. Then, an image-based quality index was developed to give quantitative quality output. Finally, a design of experiments of process parameters was conducted to build a process model and guidelines that can be used to predict printed line width and minimize printed overspray and edge roughness.

5.2 Vibration-Based Atomization Monitoring

Atomization is the very first stage of the aerosol jet printing process. At this stage, a functional ink is energized by outside energy sources, which excites the ink and generates aerosol droplets. There is still a lot to learn about the AJP process, but one certainty is that there isn't a single physical model that can be used to predict outcomes. There are several types of atomization processes based on different mechanisms, such as pneumatic atomization, electrostatic atomization, ultrasonic atomization, etc. In this thesis, ultrasonic atomization is used because it requires less material compared with other atomization techniques.

When a beam of ultrasound with sufficient intensity passes through the ink and is directed at the liquid-gas interface, ultrasonic atomization occurs. Ink droplets are ejected from the surface into the surrounding gas. The unique advantage of ultrasonic atomization over other atomization techniques is that the mist particle size distribution and mist density can be independently controlled. This is particularly important with printed electronics since both mist particle size distribution and density determine the output volume and overspray. The size of the droplets in the mist can be controlled by changing the frequency of the ultrasound. The mist density can be controlled by adjusting the air flow above the ink surface. This independent control cannot be achieved by other commonly used atomization techniques. Although ultrasonic atomization possesses a lot of advantages over other atomization methods, there is still a lack of a monitoring mechanism to ensure process stability.

During the printing process, atomized droplets are constantly delivered through carrier gas at a fixed flow rate. The output volume rate at the nozzle exit can be expressed by the particle volume density multiplied by the fixed gas flow rate

$$V = \rho F \tag{6}$$

where V is the rate of deposited volume on the substrate. F is the carrier gas volume flow rate. ρ is the volume density of the aerosol defined as the total volume of particles in unit volume. From the equation, volume density of the aerosol directly determined the rate of deposition volume. This volume determines the line width, thickness and other line morphologies.

Directly monitoring the effectiveness of ultrasonic atomization is challenging due to the complexity of liquid-gas interactions and flow dynamics. Traditionally, atomization stability and particle density can be characterized using the aerosol particle analyzer. However, particle analyzer requires a large dilution of gas, which cannot be integrated as an inline sensor while printing. The cost of the particle analyzer is another factor that needs to be considered. Therefore, a surrogate monitoring technique would be required to indirectly monitor the atomization process. For our work, we developed a vibration-based monitoring technique as an effective tool that can give a response similar to a particle analyzer.

Figure 25 shows the normal experimental setup for ultrasonic atomization. During the atomization process, the ink vial in the ultrasonic atomizer resonates with the ultrasonic energy source. The vibration signal can be represented as a mixture of various vibration sources that were applied on the ink vial. A general vibration model for ultrasonic

atomization can be describe as linear combinations of several independent vibration sources

$$x(t) = a_1 x_1(t) + a_2 x_2(t) + a_3 x_3(t) + \cdots + a_M x_M(t) \quad (7)$$

where $x_i(t), i = 1,2,\ldots,M$ is the time series of the i-th vibration source. The random noise is treated as one of the M sources here. The coefficient a_i determines the degree of participation or the normalized scale of each source to the mixture of vibration signal x. Vibration components are not easy to characterize one by one because of the complex liquid-gas interaction. An obvious vibration component in ultrasonic atomization is the vibration generator. Other components such as liquid film or bouncing droplets are also vibration components in the system.

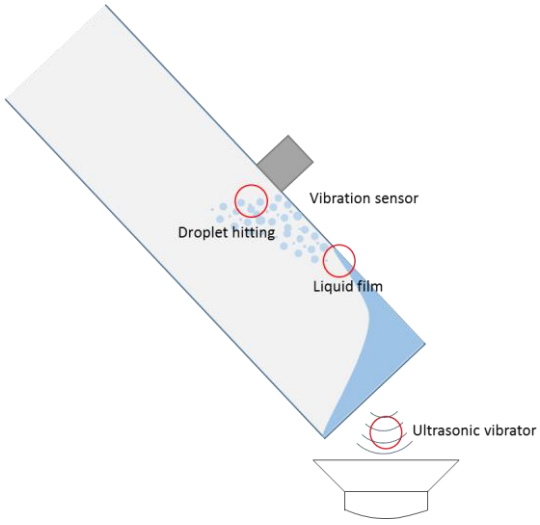

Figure 25: Vibration sources in ultrasonic atomizer

The atomization status can be categorized into three different states. At the first state, the ink vial contains the right amount of material and the vibration signal is steady. In the second state, the ink drops to a critical volume and the vibration signal starts to show

transient behavior. In the third state, the ink volume decreases to the level where no atomization has occurred.

The vibration signal amplitude decreases, but also shows steady behavior. Figure 26 is the schematic that shows the different atomization states.

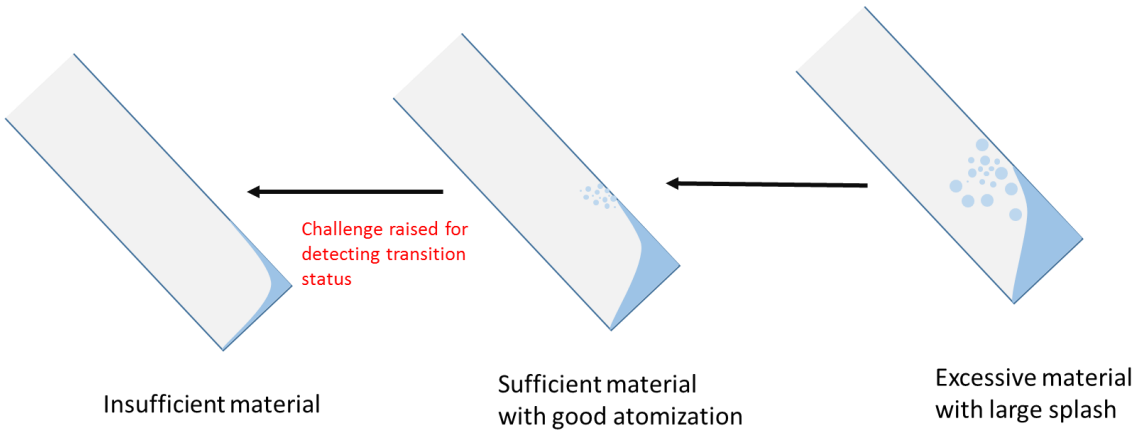

Figure 26: Vibration States (a) Insufficient material (b) Sufficient Material with good atomization (c) Excessive material with large splash

5.2.1 Monitoring Using Simple Signal Statistics

A simple approach to observing the vibration signal change is using time domain amplitude features. The following is a list of common features used for vibration monitoring:

1. Mean amplitude, $\bar{x}$ refers to average of vibration signal over a sampled interval.

$$\bar{x} = \frac{1}{T}\int x(t)dt \tag{8}$$

2. Variance amplitude, x_{Var} refers to variance of vibration signal over a sampled interval.

$$x_{Var} = \frac{\int (x(t) - \bar{x})dt}{T} \tag{9}$$

3. Root mean square amplitude, x_{RMS} is defined as the variance of the signal magnitude

$$x_{RMS} = \sqrt{\frac{1}{T}\int |\, x(t)\,|^2 \, dt} \tag{10}$$

where T is the sampled interval, and x(t) is the vibration signal.

4. Peak to Peak amplitude x_{pp} is the range of the vibration signal, $x_{\max}(t) - x_{\min}(t)$, which denotes difference between the maximum positive peak amplitude and the maximum negative peak amplitude.

Figure 27 shows the summary vibration statistics of acetone ink. It can be observed that the mean and variance changed at around the 1100 second. The physical explanation of this mean shift was investigated using the particle analyzer as shown in Figure 28. The change point of the mean indicates the atomization is going to diminish because the amount of ink is insufficient to have a stable liquid layer in the ink vial. The small amount of residual ink starts to bounce around in the vial and generates large and unstable vibration signals.

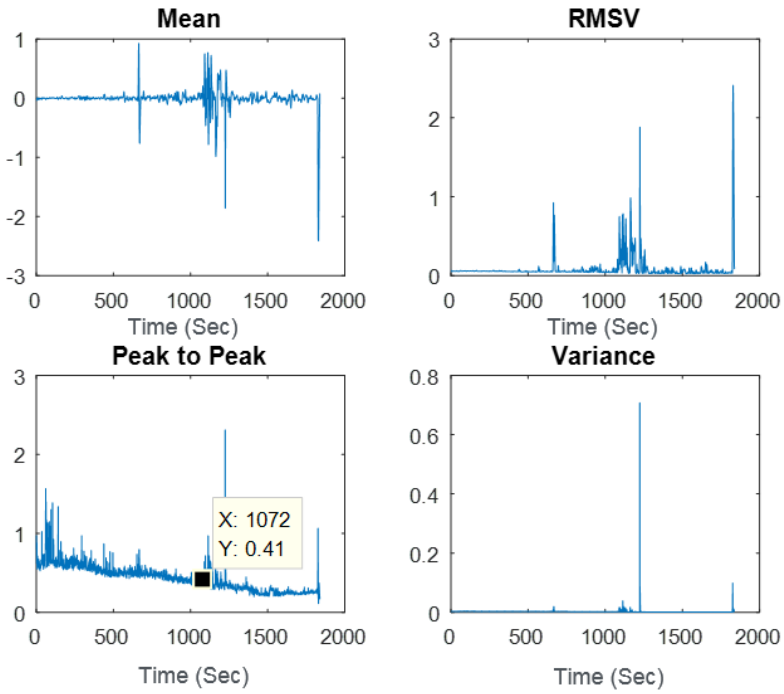

Figure 27: Summary of vibration statistics

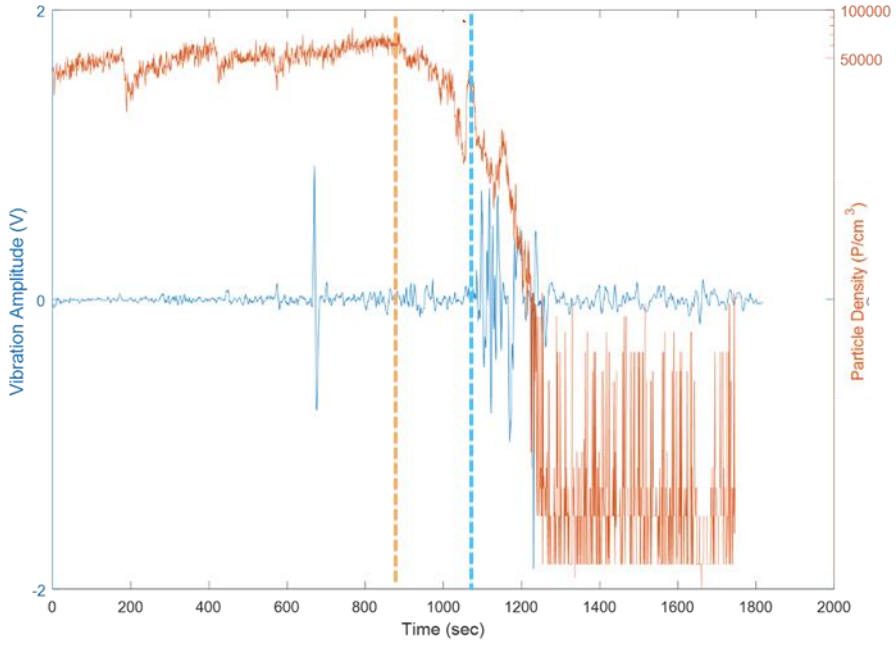

Figure 28: Vibration Mean Signal vs Particle Analyzer Signal

The time domain features can provide useful information when the atomization is near a diminishing point. However, there is a delay between the actual process shifting and the vibration signal as shown in Figure 28. The actual degradation observed from particle analyzer started around 850-second, which is 150 seconds earlier than the time of 1100s indicated from the mean signal. This time delay is undesirable for scheduling maintenance. The printed product may require re-printing if the maintenance does not perform on time. Therefore, a better signal processing technique is needed that provides a more accurate time estimation for particle density degradation. In the next section, we propose a wavelet-based signal processing method that enhances the resolution of the vibration signal. An Kalman filter-based technique is also carried out for online process change detection.

5.2.2 Signal Resolution Enhancement Using a Wavelet-Based Method

5.2.2.1 Continuous Wavelet Transformation (CWT) Using the Fourier Transformation Method

Wavelet analysis is one of the most powerful and widely applied tools in time-frequency transformations. Due to the nature of the manufacturing process, the signals are usually non-stationary. Traditional time-frequency domain methods such as Fast Fourier transformation (FFT) and Short-Time Fourier transformation (STFT) are limited because of their constant time and frequency resolution properties. On the other hand, the continuous wavelet transformation (CWT) is much better for analyzing nonstationary waveform signals in the time-frequency domain. It is different from FFT and STFT that allow clear localization on the time axis of the frequency components.

The basic idea of wavelet transformation is to decompose waveform signals into different numbers of components. In CWT, the transformation reflects the correlation between the analyzed continuous-time signal $x(t)$ and the wavelet function as defined by the following formula:

$$\begin{aligned} CW(a,b) &= \int_{-\infty}^{\infty} x(t)\psi_{a,b}^{*} dt \\ &= \frac{1}{\sqrt{a}} \int_{-\infty}^{\infty} x(t)\psi^{*}\left(\frac{t-b}{a}\right) dt \end{aligned} \tag{11}$$

where $CW(a,b)$ is a function of parameters a and b. Parameter a is the dilation of the wavelet. It is also called scale parameters in other literature. Parameter b is the position parameter that defines a translation of the wavelet and indicates the time location. Function ψ^{*} is the complex conjugate of the analyzing mother wavelet $\psi(t)$. The coefficient $1/\sqrt{a}$ is an energy normalized factor.

A wavelet function must satisfy the following criteria in order to be classified as a basic permissible wavelet:

1. The wavelet must have finite energy

$$E = \int_{-\infty}^{+\infty} |\psi(t)|^2 \, dt < \infty \tag{12}$$

2. The following condition must hold true

$$C_{\psi} = \int_{-\infty}^{+\infty} \frac{|\psi^{\wedge}(\omega)|^2}{\omega} \, d\omega < \infty \tag{13}$$

where

$$\hat{\psi}(\omega) = \int_{-\infty}^{+\infty} \psi(t) e^{-i\omega t} dt \tag{14}$$

is the Fourier transform of the $\psi(t)$ function and $\omega = 2\pi f$ is the circular frequency. This condition is defined as a condition of admissibility and can be interpreted as requirement that $|\psi(\omega)|^2$ decay endeavored to zero faster than$1/\omega$. In other words, the condition indicates that the wavelet has no zero frequency component, that is

$$\hat{\psi}(0) = 0 \tag{15}$$

Otherwise, the wavelet must have a zero mean value. In this case, C_ψ is called the admissibility constant. The value of C_ψ depends on the chosen wavelet. When the wavelet is a complex wavelet, the Fourier transform must have both a real component and a value of zero for negative frequency.

From CWT we could obtain a two dimensional scalogram $E(a,b) = |CW(a,b)|^2$ that represents the energy distribution of signals for used scales a and position b. The CWT can be seen as a transform that converts the waveform from time domain to scale-time domain. And the scale can be converted to a frequency value called pseudo-frequency. This value depends on the center frequency of the applied wavelets and the scale value a, that is

$$f_a = \frac{f_c}{a} \tag{16}$$

Where f_a is the pseudo-frequency associated with the wavelet at a scale. f_c is the characteristic frequency of the mother wavelet at scale $a = 1$ and time position $b = 0$.

There are several algorithms that can efficiently calculating CWT. One of the algorithms is using FFT algorithm.

If we define

$$\psi_a(t) = \frac{1}{\sqrt{a}}\psi\left(\frac{t}{a}\right) \tag{17}$$

and

$$\psi_{ab}(t) = \frac{1}{\sqrt{a}}\psi\left(\frac{t-a}{a}\right) \tag{18}$$

then the CWT transformation can be written in an alternative form

$$C_W(a,b) = \int_{-\infty}^{\infty} x(t)\psi_{ab}^*(t)dt = \int_{-\infty}^{\infty} x(t)\psi_a^*(b-t)dt \tag{19}$$

that means the CWT can be seen as a convolution of the waveform signal and the designed wavelet function. Consequently, CWT can also be expressed in the form of inverse Fourier transform

$$C_W(a,b) = \frac{1}{2\pi}\int_{-\infty}^{\infty} \hat{x}(\omega)\hat{\psi}_{a,b}^*(\omega)d\omega \tag{20}$$

where

$$\hat{\psi}_{a,b}^*(\omega) = \sqrt{a}\hat{\psi}^*(a\omega)e^{i\omega b} \tag{21}$$

and

$$\hat{x}(\omega) = \int_{-\infty}^{\infty} x(t)e^{-i\omega t}dt \tag{22}$$

represent the Fourier transform of the analyzed signal $x(t)$.

In most signal processing cases, the signal is digitalized and therefore discrete. If the input signal $x(n)$ contains N samples, the discrete version of the CWT convolution can be expressed as

$$W_a(b) = \sum_{n=0}^{N-1} x(n)\psi_a^*(b-n) \tag{23}$$

In order to obtain the CWT at different time location *b* at each value of the scale *a*, a fast discrete Fourier transformation can be used to calculate the circular convolution

$$\sum_{n=0}^{N-1} x(n)\psi_a^*(b-n) = \frac{1}{N}\sum_{k=0}^{N-1} \hat{x}(k)\hat{\psi}_a^*(k)e^{\frac{i2\pi kb}{N}}, \qquad b = 0,1,2,...,N-1 \tag{24}$$

the discrete Fourier transform for the waveform signal is given by

$$\hat{x}(k) = \sum_{n=0}^{N-1} x(n)e^{-\frac{i2\pi nk}{N}}, \qquad k = 0,1,2,...,N-1 \tag{25}$$

and $\hat{\psi}_a$ is the discrete Fourier transform of the mother wavelet ψ_a which can be expressed as

$$\hat{\psi}_a(k) = \sum_{n=0}^{N-1} \psi_a(n)e^{-i\frac{2\pi}{N}nk}, k = 0,1,2,...,N-1 \tag{26}$$

where *k* is an index of frequency.

Assuming that the signal is sampled at frequency $f = f_s$, the sampling period is $\Delta t = 1/f_s$. In order to obtain the unit energy for each scale *a*, the wavelet function is normalized as follows

$$\hat{\psi}_a(a\omega_k) = \sqrt{\frac{2\pi a}{\Delta t}}\hat{\psi}(a\omega_k), \tag{27}$$

where

$$\omega_k = \frac{2\pi k}{N\Delta t} \tag{28}$$

Finally, the CWT can be expressed as the inverse Fourier transform

$$W_a(b) = \frac{1}{N}\sqrt{\frac{2\pi a}{\Delta t}}\sum_{k=0}^{N-1}\hat{x}\left(\frac{2\pi k}{N\Delta t}\right)\hat{\psi}^*\left(\frac{a2\pi k}{N\Delta t}\right)e^{\frac{i2\pi kb}{N}} \tag{29}$$

5.2.2.2 Signal Processing and Monitoring Using a Continuous Time Wavelet

The vibration signal consists of several different vibration sources. As discussed before, it is hard to distinguish different vibration components in the atomization system. The challenge here is how to decompose a single channel signal into different components without the knowledge of the signal source. Decomposition methods such as empirical mode decomposition (EMD) and wavelet transformation are the most popular methods for single channel signal separation. Wavelet decomposition can be seen as a series of bandpass filters that provide multi-resolution on different frequency bands. At high frequencies, the wavelet reaches a high-time resolution, but has a low-frequency resolution. Conversely, at low frequencies, a high-frequency resolution and a low-time resolution can be obtained. In CWT, the frequency range is determined by the scale parameters. Low-scale parameters correspond to more contracted wavelets that are sensitive to rapidly changing details or high frequency components. High-scale parameters, on the other hand, correspond to more stretched wavelets, which are sensitive to slowly changing, coarse features or low-frequency components. In the atomization system, the low-frequency components are usually created by liquid film vibration and large droplet splashing. They are not directly related to the actual atomization status.

High-frequency components are related to the high frequency aerosol bursting and the resonant vibration from the ultrasonic vibrator. Under this observation, it is expected that aerosol bursting will decrease when the atomization process diminishes and the energy contribution from the high-frequency components are reduced, correspondently. We expected to observe the atomization status changes by monitoring the energy density at a low-scale (high-frequency) level.

Parseval's theorem suggests that the proportion of the spectral energy density can be calculated by summing the square of the spectrum amplitude across all frequency components. That is,

$$E_a = \frac{\sum_{t=1}^{n} Y_a(t)^2}{n} \tag{30}$$

where $\boldsymbol{Y_a}(t)$ is the decomposed vibration signal for scale parameter a and n is the number of samples in each sampling interval.

Based on above description, the proposed method for processing our vibration signal is depicted in Figure 29.

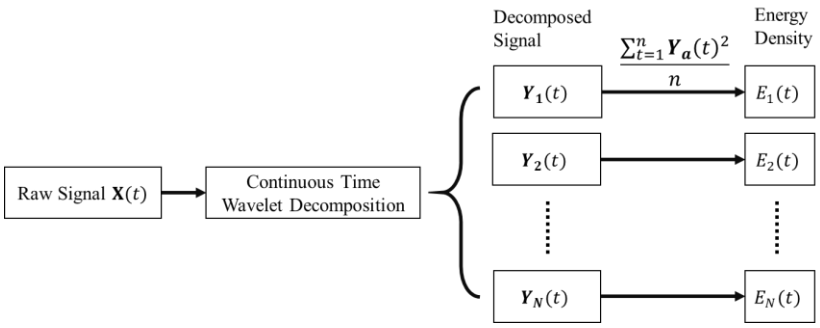

Figure 29: Schematic of vibration data processing procedure

In the first step, the raw signal vector $\boldsymbol{X}(\boldsymbol{t})$ in a sample interval t is decomposed using CWT using Fourier transformation at different scale level $a \in \{1, N\}$ to generate N decomposed signal vector $\boldsymbol{Y}_{\boldsymbol{a}\in\{\boldsymbol{1},\boldsymbol{N}\}}(\boldsymbol{t})$. For each decomposed signal vector in a sampling interval t, the corresponding energy density $E_{a\in\{1,N\}}$ is calculated using equation x. Figure 30 shows the energy density plot for 32 decomposition scale levels. It can be seen that the energy density signal shows a decreasing trend for scale levels 1 to 16. Scale levels 5 to 16 show an inconsistent trend and larger variation in the signal. In order to enhance the monitoring profile resolution, we select a signal from 1 to 4 to reconstruct the monitoring profile. The reconstruction procedure can be done by adding a decomposed signal between 1 and 4. The result is shown and compared with particle analyzer data in Figure 31. The time delay that was originally found when using time domain features is clearly reduced.

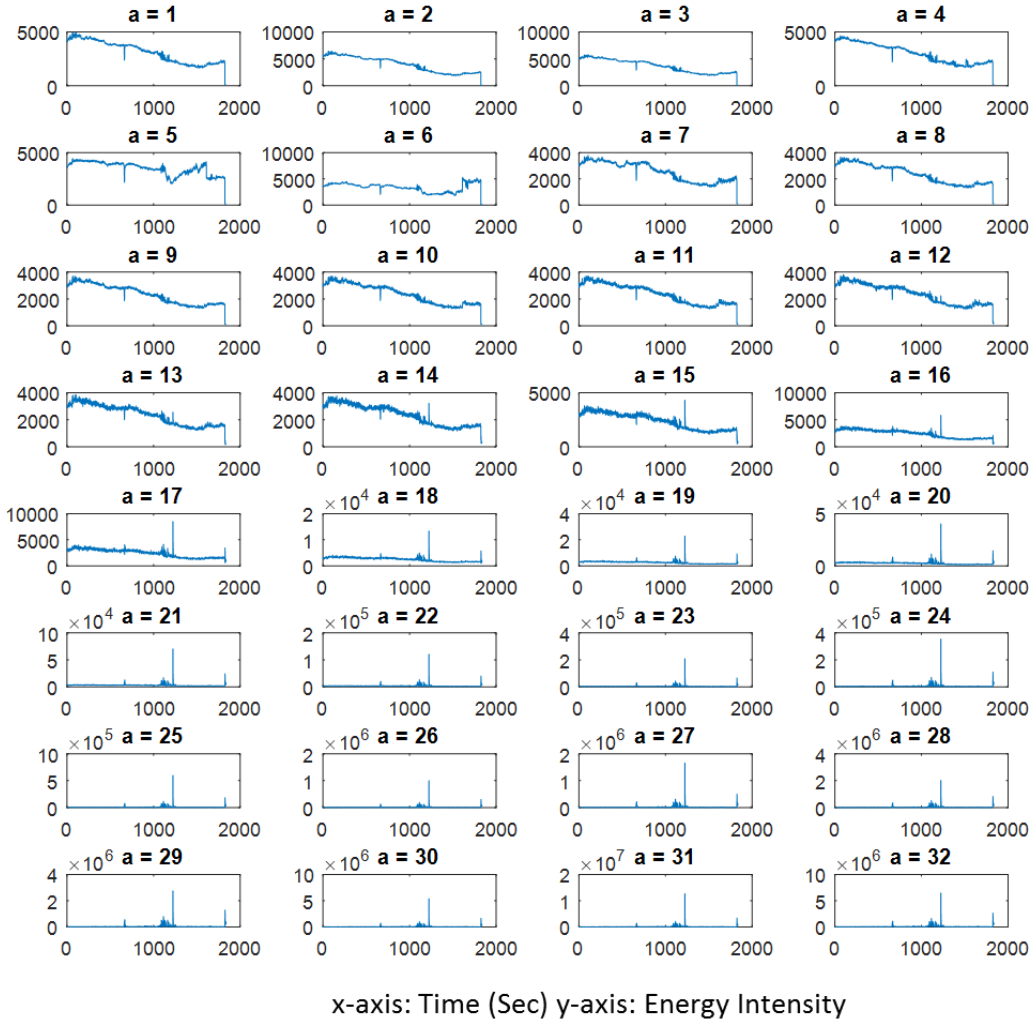

Figure 30: Energy intensity signal over time for different decomposition scale levels

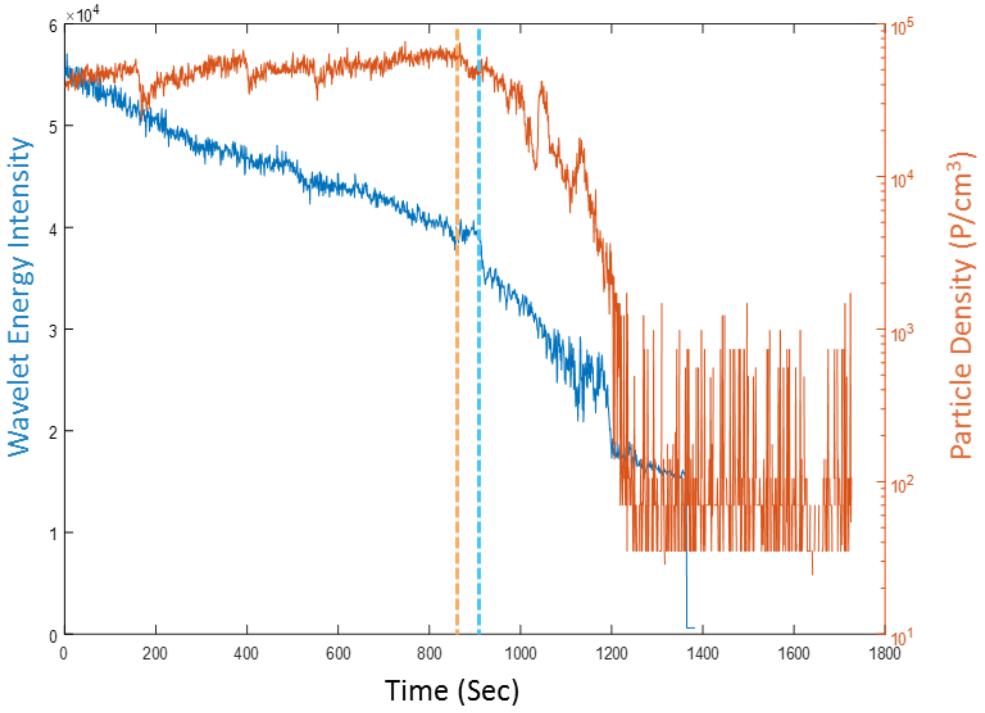

Figure 31: Reconstructed energy intensity signal after removing low-frequency components versus particle density

5.2.3 Online Process Change Detection Using Kalman Filter

In the previous section, the energy intensity signal extracted via wavelet method shows a downward trend with slope change near the process shift point indicated from the particle analyzer signal. The status of the atomization cannot be directly observed from the vibration signal, but may can be considered as hidden states and inferred from the energy intensity signal. The hidden states represent the underlying atomization process and the observable states are vibration signals we monitored. The Kalman filter is a popular technique to infer hidden states in streaming data through a given state space model. Therefore, this section is focused on developing an online status detection model using a Kalman filter. The innovation of the prediction error of the Kalman filter can be used as

the monitoring statistic. Using a simple cumulative control chart (CUSUM), we can develop an online monitoring framework for monitoring and detecting the process shifting. A general Kalman filter is described in the following section.

5.2.3.1 Kalman Filter

Considered the extracted energy intensity signal at time k as x_k , $0 < t < \infty$. We assume that x_k can be expressed by the linear combination of preceding energy intensity signal as

$$x_k = Ax_{k-1} + w_{k-1} \quad (31)$$
$$z_k = Hx_k + v_k \quad (32)$$

Where x_{k-1} and x_k are the model estimates in the previous and present state, respectively; A represents the transition model linking x_k and x_{k-1}; z_k is the observation at a given state; w and v are assumed to be Gaussian random variables that represent the process noise $N(0,Q)$ and measurement noise $N(0,R)$. H relates the state to the observation z_k. The Kalman filter is implemented in two step. The first step is called time update step. In this step, the linear state transition model propagates the estimate of the previous state and its uncertainty to provide prior estimates of the present state of the model and its uncertainty. These can be expressed as

$$x_k^- = A\hat{x}_{k-1} \quad (33)$$
$$P_k^- = AP_{k-1} + w_{k-1} \quad (34)$$

where $\hat{x}_{k-1}$ is the posterior estimate of the variable in the previous state. x_k^- is the prior estimate of the present state. P_{k-1} is the posterior uncertainty of the previous state and P_k^- is the prior uncertainty for the present state. The second step is called measurement

update step. Here, the prior estimates and their uncertainties are updated with the new observation via a linear combination of the prior model estimate and a weighted difference between the observation and prior estimate of the model state. The weights are defined as Kalman gain (K)

$$\hat{x}_k = x_k^- + K_k(z_k - Hx_k^-) \quad (35)$$

$$P_k = (1 - K_k H)P_k^- \quad (36)$$

$$K_k = P_k^- H^T (HP_k^- H^T + R)^{-1} \quad (37)$$

where $\hat{x}_k$ is the posterior estimate of the state. The difference between the observed value and predicted value (posterior estimate) is called residual which can be calculated as

$$e_k = x_k - \hat{x}_k \quad (38)$$

If the atomization process is in good condition and stable, the Kalman filter estimation is a good representation of the energy intensity signal. In this case, the residual e_k corresponds to the process noise w_k and does not give a large value. If the process starts to shift to another atomization status, the residual value is going to change because the model cannot adapt and represent the current dynamic of the system. Therefore, the atomization process can be detected by monitoring the residual value of the Kalman filter fitting.

5.2.3.2 Online Monitoring of Residual using CUSUM Control Chart

CUSUM chats is a widely used statistical method for online change detection of process mean shift. The CUSUM chart can be formulated as a sequence of tests, where each test is a sequential probability ratio test (SPRT). If X_k has the density f $f(x_k \mid \theta)$, where θ is

the process parameter, then the CUSUM chart for detecting a change in θ from the in-control value θ_0 to some out-of-control value θ_1 accumulates the terms

$$z_k = \ln \frac{f(x_k \mid \theta_1)}{f(x_k \mid \theta_0)} \tag{39}$$

and signals at sample k if the CUSUM statistics

$$C_k = \max(0, C_{k-1}) + z_k \tag{40}$$

exceeds the pre-defined control limit h. The starting value for the CUSUM statistics usually taken as $C_0 = 0$.

5.2.3.3 Result of Online Detection using Kalman Filter and CUSUM Control Chart

Figure 32 (a) shows the energy intensity signal with Kalman filtered signal. The Kalman filter parameters Q and R were estimated using maximum likelihood method from the first 60 seconds of the energy intensity signal. Figure 32 (b) shows the residual of the Kalman filtered signal. The residual shows zero mean behavior at the early stage, which corresponds to stable atomization. When the energy intensity signal starts to deviate from the original trend, the atomization status changes as discussed in the previous section. The corresponding residual also increases, which indicates the Kalman filter is an effective method to capture the linear dynamic changes of the atomization system. Figure 33 shows the CUSUM control chart of the Kalman filtered residual. The control limit h of the CUSUM control chart was chosen as 3σ from the first 60 seconds of the residual signal. Table 5: Comparison of Process Shift Time shows the out-of-control time of the CUSUM control chart and the experimental degradation time from the particle analyzer

of 5 samples. The result shows that CUSUM detect the process shift in under 30 seconds. It is a great improvement compared to the method using only simple statistics.

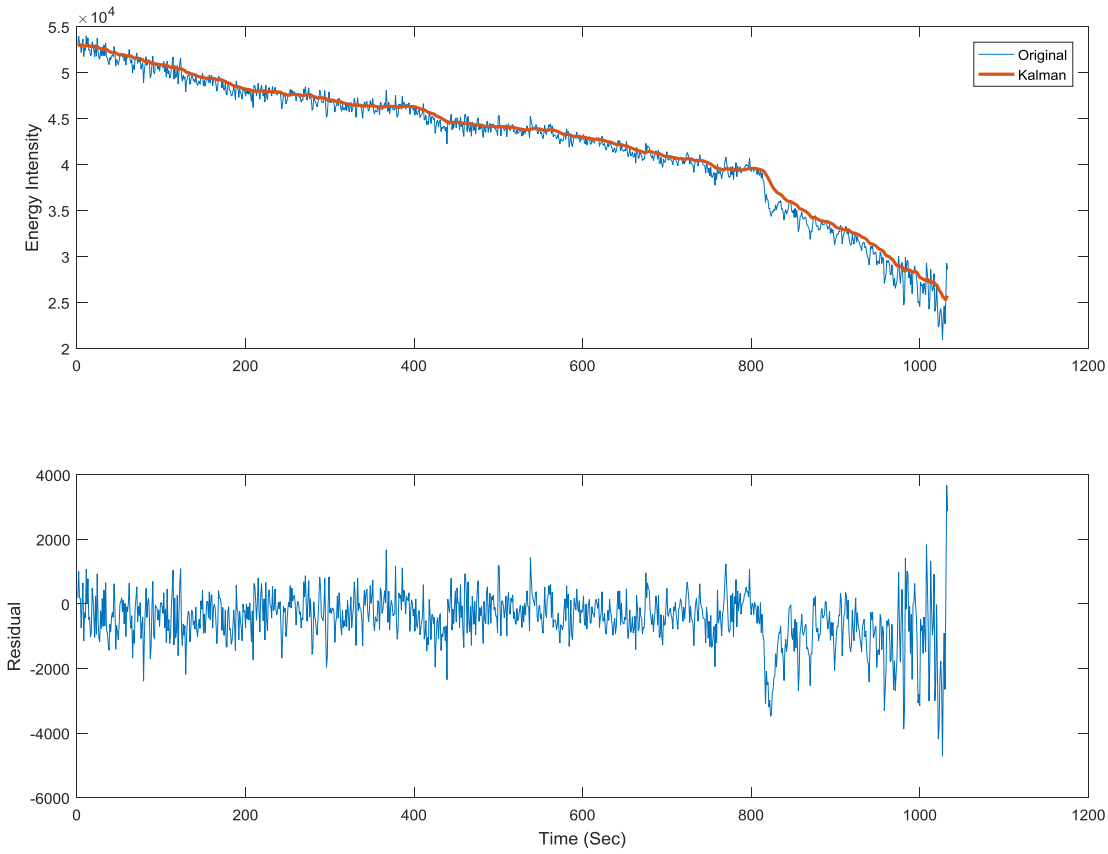

Figure 32: Kalman Filter Response and Residual

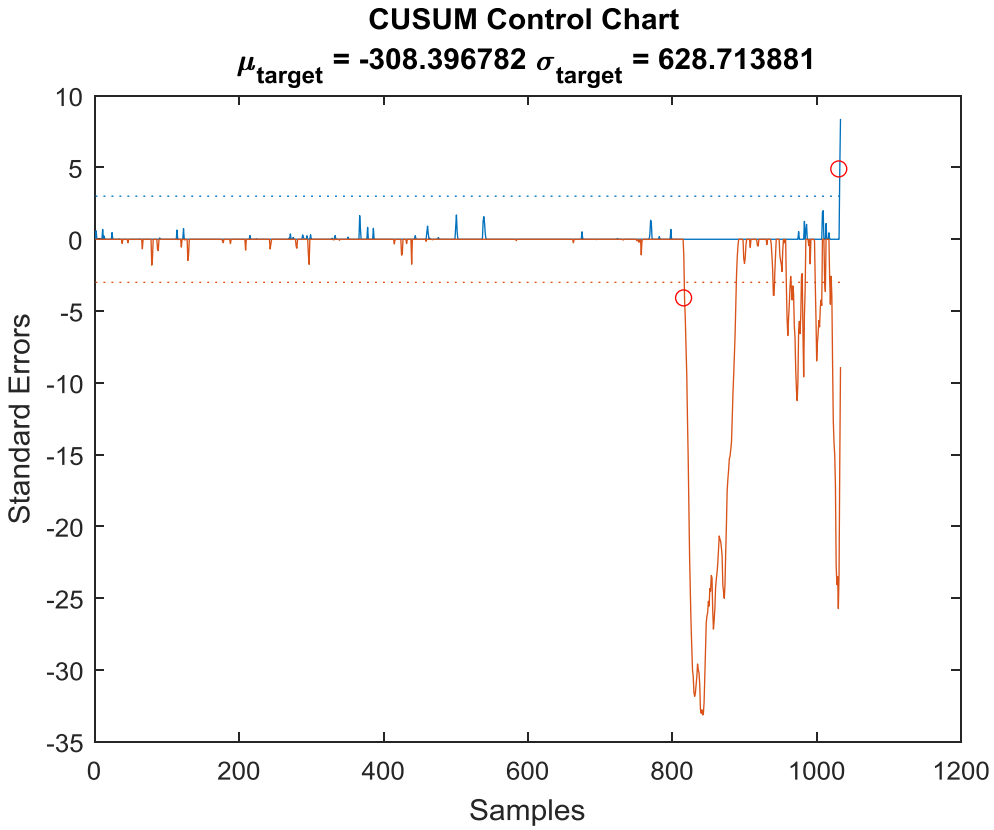

Figure 33: Online Change Point Detection Using CUSUM

Table 5: Comparison of Process Shift Time

	Process Shift Time (Sec)		
	Particle Analyzer	**Simple Statistics (Mean)**	**Kalman CUSUM**
Experiment 1	836	855(+19)	920 (+84)
Experiment 2	789	802(+13)	911(+122)
Experiment 3	812	830(+18)	908(+96)
Experiment 4	854	862(+11)	978(+124)
Experiment 5	837	855(+15)	942(+105)

5.2.4 Case Study: Variation Reduction in CNT Gas Sensor Fabrication

To demonstrate the effectiveness of the atomization monitoring method, we fabricated 20 CNT gas sensors using the same experimental setup described in Chapter 4. Each individual sensor was printed with 12 layers. The process time for each sensor was

around 18 minutes. These 20 sensors were divided into control groups and experimental groups, respectively. In the control group, 10 sensors were printed without considering the atomization status. That is, the AJP printer was running for 120 minutes without any maintenance. In the experimental group, the atomization process was monitored with the developed monitoring method. The printing process was paused and the CNT ink was replenished when the CUSUM exceeded the control limit. Figure 34 shows the comparison of resistance between the groups. It shows that the variation of the resistance was reduced around 48% when using the strategy of monitoring online with immediate maintenance.

Figure 34: Comparison of variance of resistance between batches with and without maintenance the process Figure 34 compares the resistance variation of 9 gas sensors with and without controlling the process window. With no control strategy, 9 gas sensors were printed continuously without maintaining the AJP machine. Each sensor was printed with 12 layers. The fabrication time for each individual sensor was around 18 minutes. Under a control strategy, the AJP machine was purged and the ink was replaced every 30 minutes. The variation of the resistance was reduced by 48% when adopting the maintenance strategy.

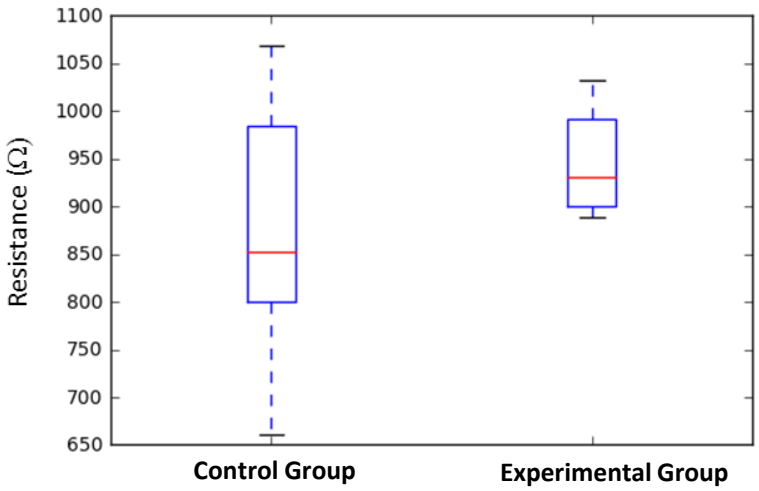

Figure 34: Comparison of variance of resistance between batches with and without maintenance the process time

5.2.5 Conclusion

In this section, we proposed a wavelet-based method for monitoring the atomization process status. Simple time domain features can only detect the atomization status when the atomization is almost diminished. A wavelet-based method is used to decompose the single channel signal into different components in several frequency bands. The energy of high-frequency components are calculated and accumulated to establish a new monitoring signal. The new signal reduced the delay time that was found when using time domain features and reveals features of particle density fluctuation that cannot be detected in the previous time domain method. A clear decreasing and degradation trend indicates the atomization is a non-stationary process because of constant material loss during the printing process. In the real application, the proposed method can help estimate the process window and establish the maintenance schedule. The real-time vibration data can also be used to ensure the stability of the AJP process.

5.3 Image-based Quality Metrics of AJP Printed Lines

In printed electronic applications, printed line morphologies are important factors that determine device performance, uniformity, and quality. Lines with consistent morphology yield good conductivity and a low chance for short circuiting. On the other hand, lines without consistent morphologies usually have unpredictable electrical resistance or even are non-conductive. Bad quality lines also reduce the completion rate of the product. Printed line is a natural quality index (QI) to describe the quality. However, it is difficult to incorporate real-time electrical resistance characterization into the printing process because most of the conductive inks require post sintering to activate the conductivity. Since the most direct way to extract the process information in real time during printing is through the image taken by an in-process camera, it is meaningful to develop a set of QIs that are based on the geometrical parameters of the line image. Several researchers have investigated the effect of the AJP process parameters on print quality. However, their methods employed offline characterization and the results are qualitative not quantitative. Imaged-based QIs in real time can give quantitative responses in different printing quality characteristics such as line width, overspray and edge quality. By investigating the relationships between QIs and process parameters, we are able to find the optimal setting to maximize the line quality and improve the robustness of printed lines as well as performance of the device.

5.3.1 Quality Indices from Image Analysis

Figure 35 shows different conditions of typical aerosol jet printed lines. Figure 35 (a) shows a high quality printed line that is straight, with consistent morphology, has no

bulging and has minimum overspray. Figure 35 (b) shows a printed line with an excessive bulging condition. The bulging yields inconsistent resistance from device to device, which makes it difficult to predict device performance in some applications. Figure 35 (c) shows a line with a large amount of overspray. Overspray could result in a short circuit when two parallel lines are closed. Figure 35 (d) shows a discontinuous line that is usually caused by a nozzle clogging or having insufficient materials. Images acquired from an optical microscope can be used to extract the conditions from a printed line. This section discusses image processing methods to capture three major geometrical quantifiers.

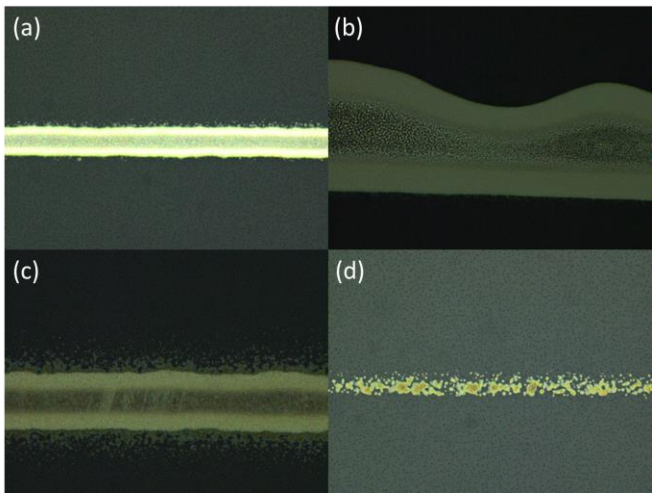

Figure 35: Printed line condition (a) Good Line (b) Bulging (c) Overspray (d) Discontinue

5.3.2 Image Analysis

Image analysis is implemented in Matlab. A code was developed to processing microscopic images of Aerosol Jet printed line and extract geometrical quality metrics

after pre-processing. A microscopic image of an Aerosol Jet printed line on polyimide film is shown in Figure 36.

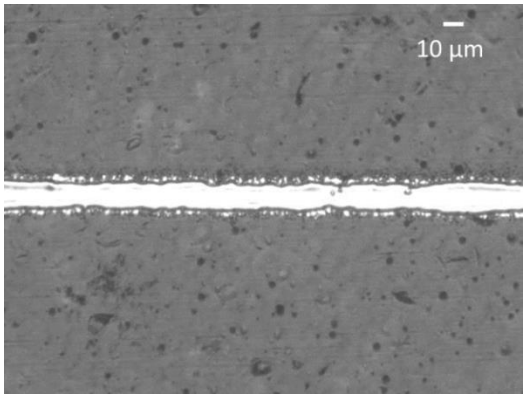

Figure 36: An example of Aerosol Jet printed lines

Overspray on both edges of the main line path can be observed. Overspray consists of discrete ink spots that do not contribute to the main line conductivity. Therefore, in the image analysis we remove the overspray by denoising. The flowchart of image analysis procedure is shown in Figure 37.

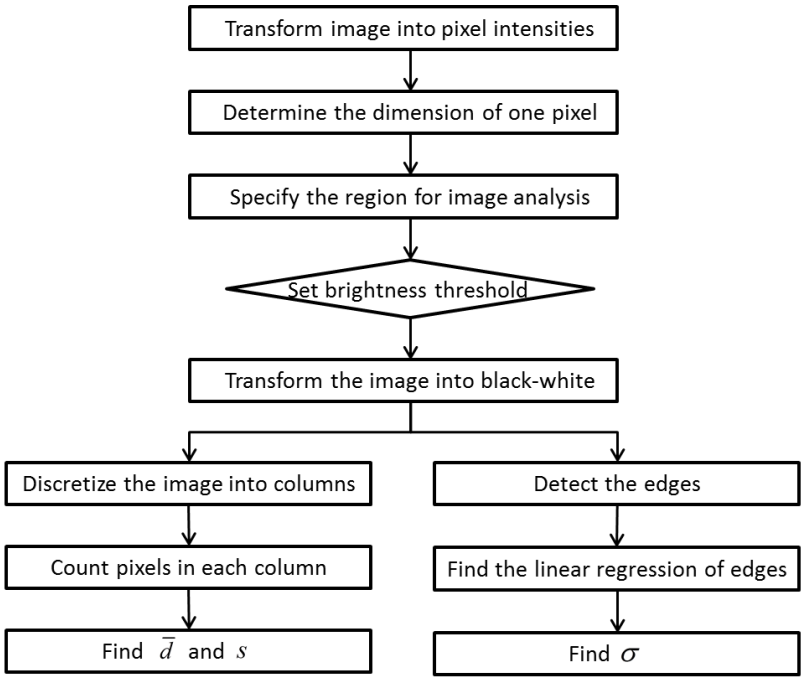

Figure 37: Flowchart of image analysis algorithm

In the example image, the 10 µm scale bar approximately consists of 25 pixels, meaning each pixel has a side length of 10 µm / 25 = 400 nm. The Image analysis procedure of the example image is shown in figure 38.

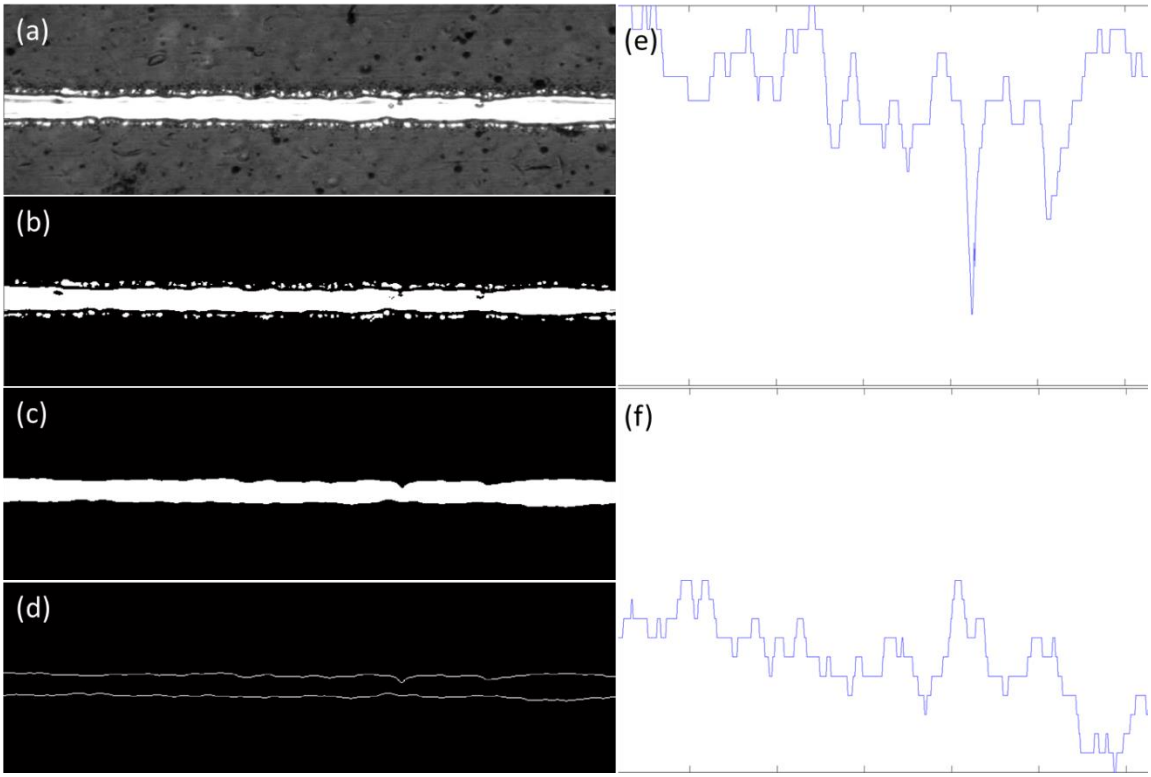

Figure 38: Image analysis of the example line image. (a) original image; (b) black-white image; (c) denoised image (main line); (d) outline of main line; (e) discretized upper edge; (f) discretized lower edge.

5.3.3 Geometrical Parameters

In the present study, we use three geometrical parameters, average line width (W), edge roughness (ER) and overspray index (OV), to describe the line image. The average line width is defined as

$$W = \frac{1}{L}\int_{x=0}^{L} d(x)\,\mathrm{d}x \tag{41}$$

;

.

The edge roughness is defined as the standard deviation of the signed distance $\delta(x)$, which is measured from the linear regression of edge points to the line edge.

$$ER = \sqrt{\frac{1}{2L}\int_{x=0}^{L}\left(\delta_{upper}^{2}(x)+\delta_{lower}^{2}(x)\right)\mathrm{d}\,x} \tag{42}$$

We define overspray index (OV) as the logarithmically-weighted distance between each overspray point and its corresponding upper and lower line edges.

$$OV = \frac{\int_{x=0}^{L}\ln\left(\theta_{upper}(x)\right)+\int_{x=0}^{L}\ln\left(\theta_{lower}(x)\right)}{2L} \tag{43}$$

Figure 39 illustrates the definition of geometrical parameters in a sketched line image.

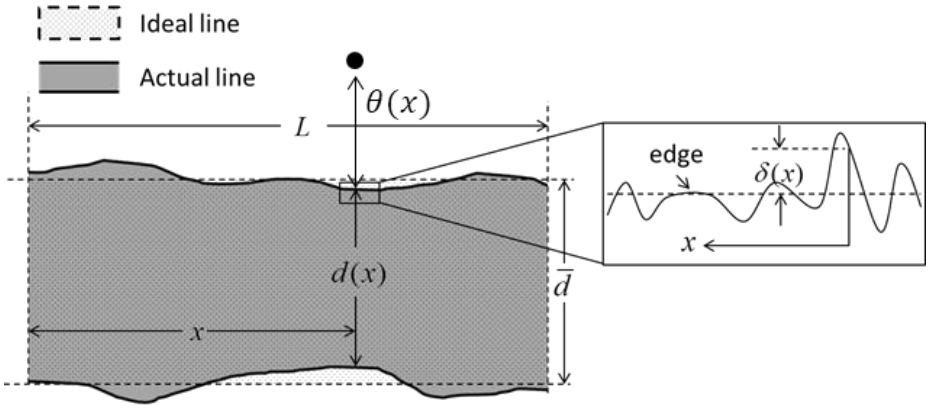

Figure 39: Definition of geometrical parameters in printed line image

Note that all three geometrical parameters are measured in a top-down microscopic image of printed line. Theoretically, the resistance of a printed line is determined not only by the line geometry in x-y plane, but also by the thickness profile in z direction. However, the thickness profile is not measurable during Aerosol Jet printing process since current measuring techniques are too slow comparing to the printing process and can only apply

to fully cured ink. In the present study, we assume all lines have a similar thickness profile for simplicity.

5.3.4 Result and Discussion

5.3.4.1 Sample Preparation and Measurement

All 10mm conductive line samples were printed in a single pass with a 150 μm nozzle on polyimide substrate. The distance from the nozzle to the substrate was 4mm. The substrate temperature was controlled at 60°C with a heated platen. Stage speed was kept at 3mm/s. Nitrogen was used as the carrier and sheath gas. Experiments were conducted with atomizer gas and sheath gas flow rates, ranging from 15 to 20 standard cubic centimeters per minute (sccm) and $50 - 60$ sccm, respectively. The printed lines were activated by sintering in an oven at 250 °C for 30 minutes. Silver nanoparticle ink (Cabot Corporation) was used and heated to 30°C during the printing process for stability. Printed line images where examined and captured with an alignment camera system built with an aerosol jet vision module. Two points of electrical conductivity were measured with an NI 9219 universal data acquisition module. The maximum resistance that could be measured was 1.05 kΩ with a 24-bit resolution.

5.3.4.2 Relationships Between Quality Metrics and Performance

The results of experiments are listed in Table 6. The parameters are:

- F_a: aerosol gas flow rate;
- F_s: sheath gas flow rate;
- W: average line width;
- ER: line edge roughness;
- R: resistance of a 5mm line.

The controllable parameters were F_a and F_s. The quality metrics, L_W and L_{EQ}, were measured from line images. The performance parameter, *R*, was measured offline after thermal sintering.

Table 6: Quality metrics and resistance under different process setting

Sample #	F_a (sccm)	F_s (sccm)	W(μm)	ER	R (Ω)
1	15	50	10.3	0.0275	161
2			10.5	0.0446	150
3			10.6	0.0513	154
4	20	50	12.9	0.0642	126
5			12.7	0.0735	139
6			12.2	0.1025	144
7	15	55	14.1	0.0631	121
8			14.4	0.0742	121
9			14.8	0.0398	102
10	20	55	15.2	0.0649	92
11			15.0	0.0720	104
12			15.3	0.1312	111
13	15	60	15.8	0.0596	88
14			16.6	0.0827	91
15			17.2	0.1098	86

The relationships between the resistance of a printed line and two quality metrics were investigated. Figure 40 indicates the relationships between resistance and line width, and between resistance and normalized standard deviation of line width.

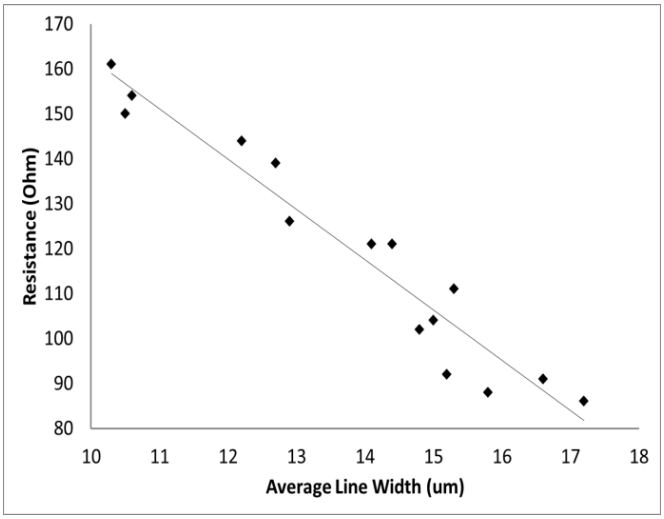

Figure 40: Relationships between resistance and quality metrics

The second quality metrics, edge roughness, does not appear to be directly related to the resistance of the printed line (Figure 41). However, it may have interaction effects with the other quality metrics.

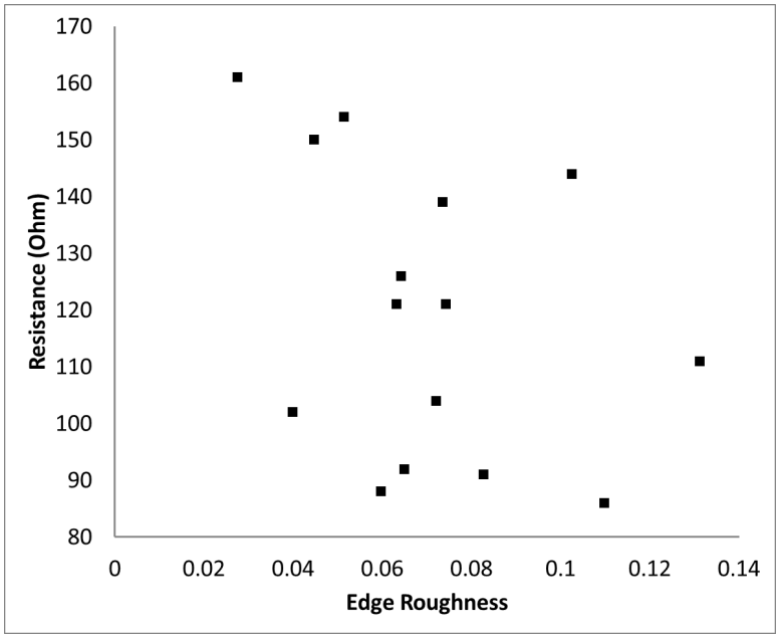

Figure 41: Resistance vs. edge roughness

5.4 Design of Experiment of AJP

The design of experiment (DOE) approach is widely used for optimization of a complex manufacturing process involving multiple variables. DOE analysis facilitates the identification of important process variables. In the AJP process, there are three major process parameters that were identified in literature as relevant to line morphologies:

- Carrier gas flow rate (sccm)
- Sheath gas flow rate (sccm)
- Platen translation speed (mm/sec)

Although these parameters have been discussed frequently, a systematic study with these parameters using the DOE method was not found. Moreover, the range of each parameter was arbitrarily selected. The interaction between each parameter was not considered in the experiment design. We see the need to perform a more detailed experiment design to investigate the parameter effects.

In past experiences we observed that the line morphologies are nonlinear responses when adjusting parameters. Traditional designs, such as factorial designs, are limited to the first order relation between process input and output. It may not be sufficient to capture the curvature of responses. Therefore, experimental design for second or higher order is required to investigate the relationship between parameters. Central composite design is a popular experimental design for building a second order model for the response variable without the need to use a complete three-level factorial experiment.

Table 7: The result and the design table for three factors CCD

			Factor 1	Factor 2	Factor 3	Response 1	Response 2	Response 3
Std	Run	Space Type	A:SH	B:CA	C:SP	W	ER	OV
4	1	Factorial	80	20	4	104	0.432444	0.9
18	*2*	*Center*	*55*	*16*	*7*	*37*	*0.0124482*	*0.09*
1	3	Factorial	30	12	4	21	0.148797	0.41
7	4	Factorial	30	20	10	79	0.0174739	0.04
19	5	Center	55	16	7	39	0.0193255	0.08
11	6	Axial	55	12	7	12	0.1225	0.34
17	*7*	*Center*	*55*	*16*	*7*	*32*	*0.0113771*	*0.09*
2	8	Factorial	80	12	4	12	0.0492873	0.44
14	*9*	*Axial*	*55*	*16*	*10*	*37*	*0.0110951*	*0.23*
5	10	Factorial	30	12	10	23	0.0204568	0.2
16	*11*	*Center*	*55*	*16*	*7*	*35*	*0.001*	*0.11*
15	*12*	*Center*	*55*	*16*	*7*	*34*	*0.0012*	*0.1*
3	13	Factorial	30	20	4	139	0.0380692	0.02
6	14	Factorial	80	12	10	14	0.118954	0.52
13	15	Axial	55	16	4	52	0.0248699	0.28
20	*16*	*Center*	*55*	*16*	*7*	*45*	*0.002*	*0.1*
9	*17*	*Axial*	*30*	*16*	*7*	*54*	*0.0103302*	*0.14*
8	*18*	*Factorial*	*80*	*20*	*10*	*96*	*0.910936*	*0.84*
12	19	Axial	55	20	7	87	0.0614729	0.68
10	20	Axial	80	16	7	55	0.341603	0.76

5.4.1 Experimental Design and Central Composite Design (CCD)

To find the relationship between printed parameters and the line morphologies, three factors CCD were carried out as shown in Figure 42. For three factors and two levels, the total number of experiments was 20, determined by the expression: 2^n ($2^3 = 8$ factor points) $+2n$ ($2 \times 3 = 6$ axial points) $+6$ (center points) as shown in Table 7. The second

order polynomial model was analyzed using the Design-Expert software package.

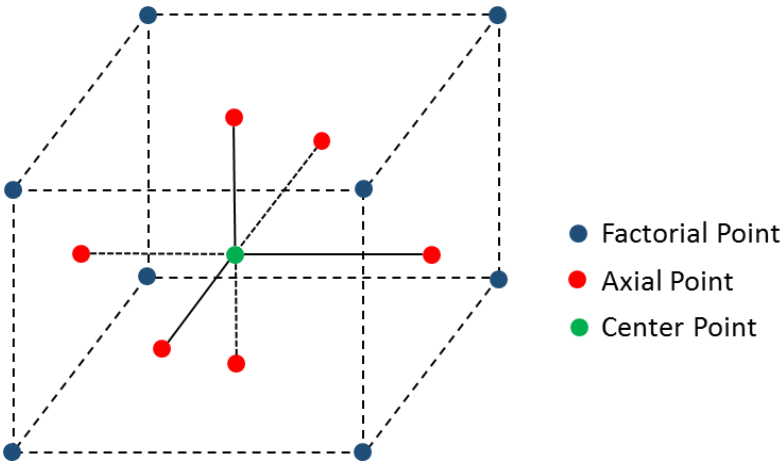

Figure 42: Three factors central composite design

The second order polynomial model is a regression model coded according to the following equation:

$$x_i = \frac{X_i - X_{i0}}{\Delta X_i} \tag{44}$$

where $x_i$is the coded value of the *i*-th independent variable, X_i is the value of the *i*-th independent variable, X_{i0} is the value of *i*-th independent variable at the center point, and ΔX_i is the step change value.

A general second order polynomial model can be expressed as

$$Y = b_0 + \sum_{i=1}^{k} b_i x_i + \sum_{i=1}^{k-1} \sum_{j=2}^{k} b_{ij} x_i x_j + \sum_{i=1}^{k} b_{ii} x_i^2 + e \tag{45}$$

where Y is the predicted response, b_0 and the intercept term, b_i represents the linear effect, b_{ij} represents the squared effect and b_{ii} is the interaction effect. The expression of

the three factors polynomial model can be approximated by the quadratic polynomial equation as follows

$$Y = b_0 + b_1X_1 + b_2X_2 + b_3X_3 + b_{11}X_1^2 + b_{22}X_2^2 + b_{33}X_3^3 + b_{12}X_1X_2 + b_{23}X_2X_3 + b_{13}X_1X_3 \quad (46)$$

where Y is the predicted response, b_0 is a constant, $b_1, b_2$and b_3 are linear coefficients, b_{12}, b_{13} and b_{b23} are the cross-product coefficients, and b_{11}, b_{22} and b_{33} are the quadratic coefficients.

5.4.2 Effect Analysis of Process Parameters

5.4.2.1 Line Width

Table 8 shows the ANOVA table for printed line width (L_W). The terms of carrier gas (B), printing speed (C), and the square of sheath gas flow rate (A^2), and the interaction of BC are significant. This result indicates the line width is primarily influenced by the carrier gas flow rate and printing speed. The carrier gas determines the amount of material that is delivered to the deposition nozzle. The relationship between the carrier gas and the line width is not linear. The printed speed contributes less to the line width compared to carrier gas. From our past experience, the printed speed can only change the line width within 10 μm. The sheath gas flow rate has contributed even less to the line width. This is also confirmed from our past experimental experience. The sheath gas can only slightly adjust the line width in the range of 5 μm.

The predicted R-Squared of 0.8915 is in reasonable agreement with the adjusted R-Squared of 0.9536. Adequate precision measures the signal to noise ratio. A ratio greater than 4 is desirable. The ratio of 29.591 indicates an adequate signal that also reveals that

the model can be used to navigate the design space. Figure 43 shows that the response surface is based on the regression model (4.1).

Table 8: ANOVA for line width response

Source	Sum of Square	df	Mean Square	F Value	p-value	
Model	98.35564181	5	19.67112836	79.0121	9.3568E-10	significant
A-SH	*0.776704292*	*1*	*0.776704292*	*3.11975*	*0.0991348*	
B-CA	*89.71899822*	*1*	*89.71899822*	*360.37*	*2.178E-11*	
C-SP	*1.55E+00*	*1*	*1.55E+00*	*6.23289*	*0.0256357*	
BC	*1.797904181*	*1*	*1.797904181*	*7.22156*	*0.0176912*	
A^2	*4.510273794*	*1*	*4.510273794*	*18.1162*	*0.0007983*	
Residual	3.485488931	14	2.49E-01			
Lack of Fit	*2.795938322*	*9*	*0.310659814*	*2.25263*	*0.1922772*	*not significant*
Pure Error	*0.689550609*	*5*	*1.38E-01*			
Cor Total	101.8411307	19				
Std. Dev.	0.498962419		**R-Squared**	0.96578		
Mean	6.727402431		**Adj R-Squared**	0.95355		
C.V. %	7.416865925		**Pred R-Squared**	0.89513		
PRESS	10.68020962		**Adeq Precision**	29.5912		

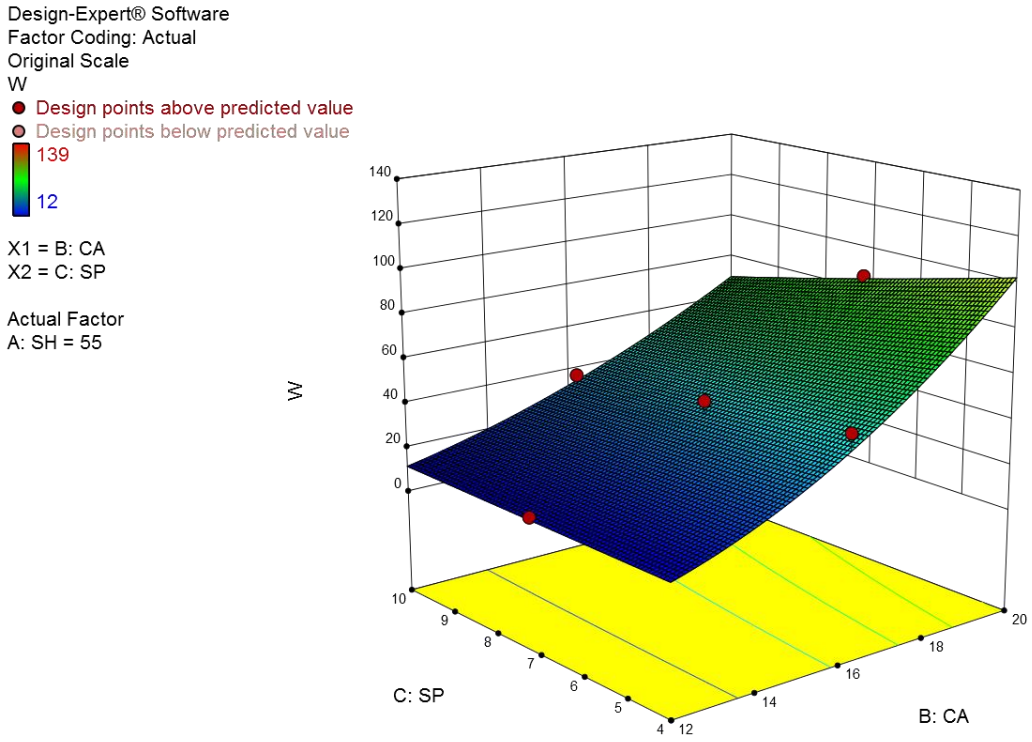

Figure 43: Response surface of line width in carrier gas flow rate and printing speed interaction

5.4.2.2 Overspray

Table 9 shows the ANOVA table for the overspray index, and the terms of sheath gas (A) and the square of carrier gas (B^2), and the interaction of AB. The model indicates the overspray is mainly controlled by the sheath gas. The interaction between sheath gas and the carrier gas means the overspray cannot be minimized by simply increasing the sheath gas. A large sheath gas with a large carrier gas makes the flow speed of the exit aerosol too fast. The high speed particles cause a large splash-type overspray on the substrate. On the other hand, a large sheath gas with a small carrier flow will cause back flow in the

system. In this case, no material can be delivered. From our past experiments and the literature, the optimal sheath gas to carrier gas ratio is around 3.

The predicted R-Squared of 0.6967 is in reasonable agreement with the Adjusted R-Squared of 0.7705. The adequate precision ratio of 29.591 indicates an adequate signal that also reveals that the model can be used to navigate the design space. Figure 44 shows the response surface based on the regression model.

Table 9: ANOVA for overspray response

Source	**Sum of Square**	**df**	**Mean Square**	**F Value**	**p-value**	
Model	1.2462575	4	0.311564375	16.9453	1.9497E-05	significant
A-SH	*0.70225*	*1*	*0.70225*	*38.1938*	*1.761E-05*	
B-CA	*0.03249*	*1*	*0.03249*	*1.76706*	*0.2036115*	
AB	*2.21E-01*	*1*	*2.21E-01*	*12.0258*	*0.0034436*	
B^2	*0.290405*	*1*	*0.290405*	*15.7945*	*0.0012217*	
Residual	0.2757975	15	1.84E-02			
Lack of Fit	*0.2752475*	*10*	*0.02752475*	*250.225*	*4.143E-06*	*significant*
Pure Error	*0.00055*	*5*	*1.10E-04*			
Cor Total	1.522055	19				
Std. Dev.	0.135596829		**R-Squared**	0.8188		
Mean	0.3185		**Adj R-Squared**	0.77048		
C.V. %	42.57357264		**Pred R-Squared**	0.69667		
PRESS	0.461679884		**Adeq Precision**	14.6648		

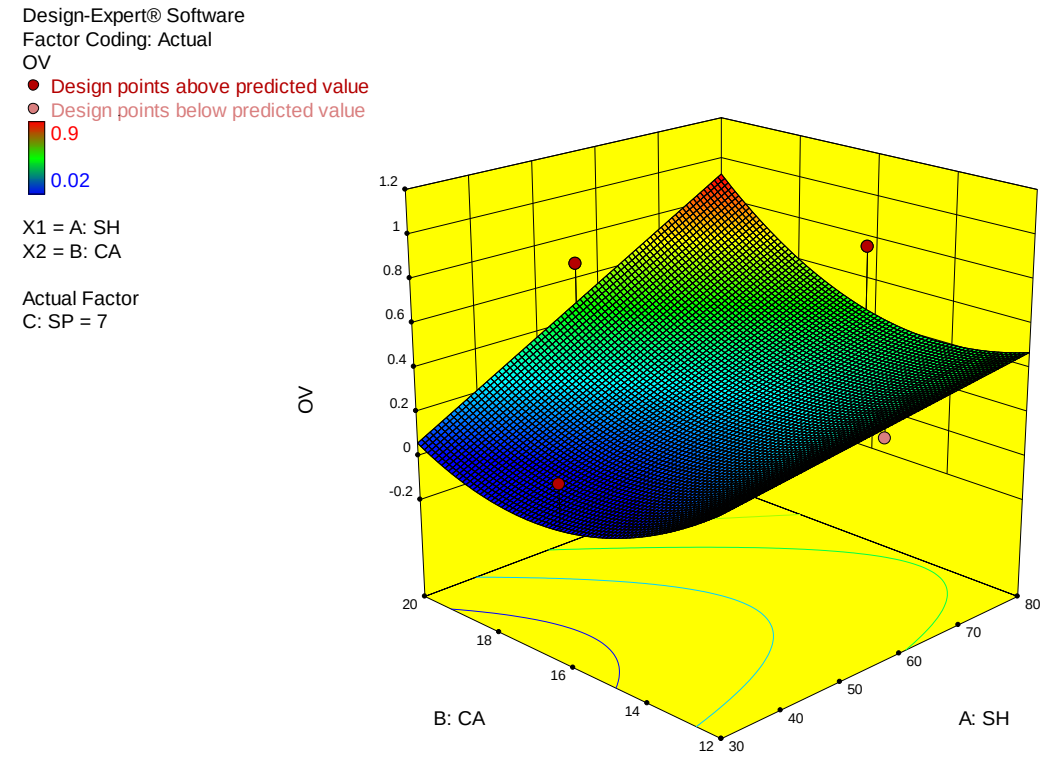

Figure 44: Response surface of overspray index in sheath gas flow rate and carrier gas flow rate interaction

5.4.2.3 Edge Roughness

Table 10 shows the ANOVA table for the edge roughness index. In this case, only sheath gas (A), carrier case (B), their square A^2, B^2 and the interaction term AB are significant. The edge roughness is primarily dominated by the sheath gas flow rate. However, there is a working region where the sheath flow rate is less than 60 sccm. The higher sheath gas flow rate causes a high speed aerosol stream in the nozzle channel, which eventually leads to undesired turbulence at the nozzle exit. Therefore, the deposited line has a large variation in line width and edge roughness.

The predicted R-Squared of 0.5519 is not as close to the Adjusted R-Squared of 0.7847 as one might normally expect. This may indicate a large block effect. Things to consider are model reduction, response transformation, and outliers. By removing two outliers from the original data. The predicted R-squared is 0.6832, which is close to the adjusted R-Square of 0.7847. The adequate precision ratio of 29.591 indicates an adequate signal that also reveals that the model can be used to navigate the design space. Figure 45 shows the response surface based on the regression model.

Table 10: ANOVA for edge roughness resposne

Source	**Sum of Square**	**df**	**Mean Square**	**F Value**	**p-value**	
Model	0.99	9	0.11	12.75	0.0002	significant
A-SH	*0.33*	*1*	*0.33*	*37.65*	*0.0001*	
B-CA	*0.055*	*1*	*0.055*	*6.35*	*0.0304*	
C-SP	*3.81E-04*	*1*	*3.81E-04*	*0.044*	*0.8381*	
AB	*0.19*	*1*	*0.19*	*22.43*	*0.0008*	
AC	*0.066*	*1*	*0.066*	*7.59*	*0.0203*	
BC	*0.016*	*1*	*0.016*	*1.81*	*0.2087*	
A^2	*0.088*	*1*	*0.088*	*10.11*	*0.0098*	
B^2	*0.05*	*1*	*0.05*	*5.73*	*0.0377*	
C^2	*3.01E-03*	*1*	*3.01E-03*	*0.35*	*0.5684*	
Residual	0.087	10	8.66E-03			
Lack of Fit	*0.076*	*5*	*0.015*	*7.01*	*0.026*	*significant*
Pure Error	*0.011*	*5*	*2.16E-03*			
Cor Total	1.08	19				
Std. Dev.	0.110648979		**R-Squared**	0.84134		
Mean	0.252516259		**Adj R-Squared**	0.78468		
C.V. %	43.81855635		**Pred R-Squared**	0.55188		
PRESS	0.484130518		**Adeq Precision**	11.7658		

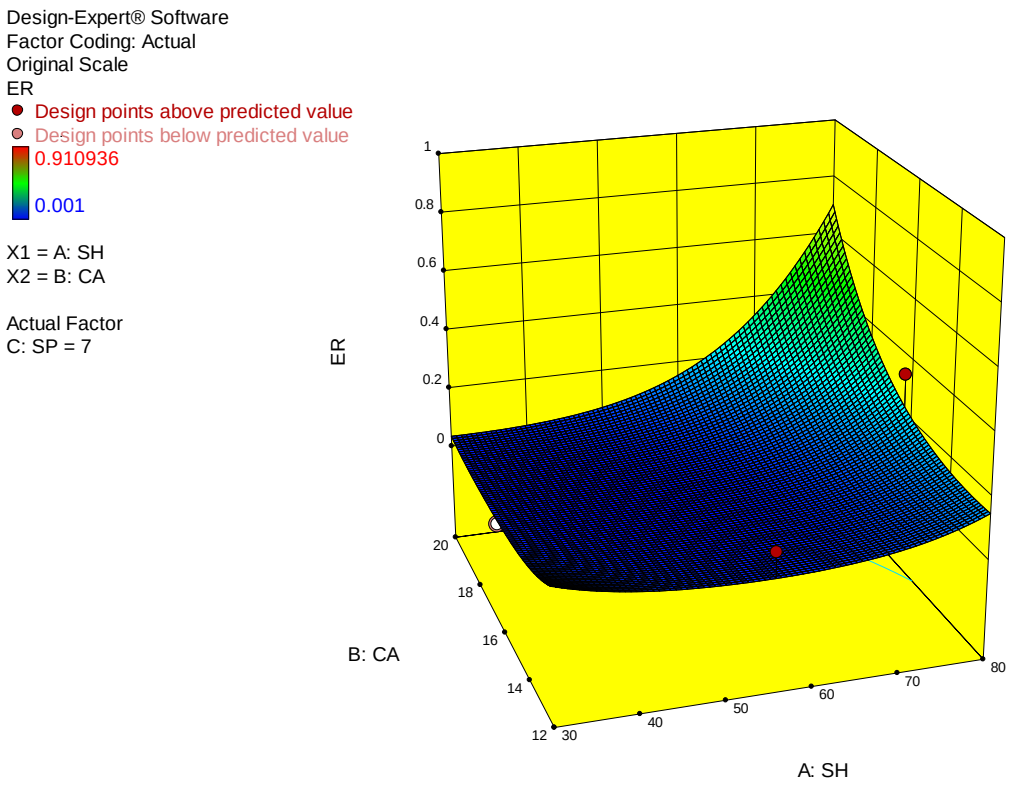

Figure 45: Response surface of edge roughness in sheath gas flow rate and carrier gas interaction

5.4.3 Case Study: Dimension Control of Printed 3D Transmission Line

In chapter 4, we discussed the manufacturing challenges of fabricating 3D transmission lines. Due to the D-band frequency requirement, the conductive circuit design of the transmission lines are all in sub-50 μm range. Furthermore, registration between multiple layers is also a key challenge. Therefore, understanding the relationship between process parameters and a creating process model is critical. The DoE is used to find optimal process parameters for desired line width with minimal overspray and edge roughness.

Table 11: Summary of geometry shows the fabrication geometries from 20 samples before and after process optimization. The maximum dimension deviation was reduced from 10 μm to 5 μm. Minimize overspray is also critical in this case study. The sub-50um structures can be shorted easily with small overspray, which fails the entire sample. We can effectively control the overspray by fine-tuning the parameters, based on the relationship derived from DoE. Before we start to control the overspray and edge roughness, 2 out of 5 samples work properly, while 4 out of 5 samples are functional when applying the control strategy. This yields a 10% increase in the completion rate.

Table 11: Summary of geometry after optimal parameter control

		After optimal parameter control		**Before optimal parameter control**	
	Design (μm)	**Fabrication (μm)**	**Deviation (%)**	**Fabrication* (μm)**	**Deviation* (%)**
d	500	500±5	1	497±8	1.6
s	500	500±3	0.6	505±6	1.2
h	40	38±2	5	38±4	10
t	3.5	3±0.5	14.29	3±5	166.67
G	30	30±2	6.67	28±6	20
W1	1300	1300±5	0.38	1295±8	0.615
W2	19	19±1	5	19±3	15.78
W3	90	92±2	2.22	88±4	4.44
W4	110	110±5	4.55	109±6	5.45
L1	8000	8000±5	0.06	80000±10	0.12
L2	11400	11400±5	0.04	11400±8	0.07

5.4.4 Guideline for Printed Line Optimization

Several guidelines for optimizing the printed line can be summarized from the DOE results.

1. The line width is primarily controlled by the carrier gas flow rate. The operation should start from adjusting the carrier flow rate to the point that the printed line width is closed to the target line width.
2. Once the printed line width is closed to the target width (±10 μm). The line width can be fine-tuned by controlling the sheath gas flow rate.
3. The best sheath-to-carrier gas ratio is around 3:1. The overspray and edge roughness can be adjusted by varying the sheath gas flow rate.
4. Overspray decreases to a minimum as the sheath gas flow increases. This is because the aerosol flow is collimated. An optimally collimated flow also leads to well-defined edges and a small amount of edge roughness. However, increasing the sheath flow beyond the stability threshold results in excessive overspray.

CHAPTER 6. NOVEL PROCESS METHODS

6.1 Overview

Although aerosol jet printing has demonstrated its capabilities in various flexible electronic applications, there is still a need to develop a new processing method for AJP in emerging areas such as nanocomposite fabrication, 3D printing, and biomedical applications. In section 6.1, we introduce a facile method that integrates printed sensors into 3D printing objects. 3D printing has drawn a lot of interest in both industry and academia in recent years, because it brings flexibility to the process of designing and fabricating complex geometric structures. However, 3D printing applications are mostly limited to passive mechanical components without built-in functionality. There are some challenges that hinder integration. A major challenge with depositing conductive inks onto 3D printed parts is the need for a high level of surface roughness. For most 3D printing processes, especially the extrusion-based process such as FDM, small 'trenches' are formed in the direction the printer is moving across the surface. When liquid inks are used, the ink spreads into the trenches under the capillary effect and causes wicking. Additional surface polishing is usually required before depositing conductive inks. Another challenge in using conductive inks is the elevated sintering temperature required for most situations. Most polymeric materials have heat deflection and glass transition temperatures that are below the optimal sintering temperature required for the DW process. Lower sintering temperatures result in high electrical resistivity of printed features, which is undesirable for most applications. We developed a facile method called the print-stick-peel (PSP) process that overcomes the above-mentioned challenges. The

PSP process does not require any fabrication on the target 3D-printed substrate, so it circumvents the fabrication challenges of surface roughness and sintering temperature. The printed patterns are first printed on low surface energy substrate that has a high glass transition temperature. Then the printed patterns are sintered at a desired temperature. Finally, the conductive patterns are transferred using the self-adhesion of 3D-printed structures or additional adhesives. This new method takes advantage of both AJP and 3D printing. It also provides a practical manufacturing technique for making multifunctional smart structures.

In section 6.2, we introduce a novel dual material fabrication method that was developed for conductive tailorable nanocomposite fabrication. Conventional methods for manufacturing nanocomposites require dispersing conductive nano-fillers (e.g CNT and carbon black) into polymeric solutions. However, the process is a challenge because even a small percentage of CNT would greatly increase the viscosity of the polymeric solution. Worse yet, dispersion-based fabrication often yields a heterogeneous distribution of CNTs in the polymer matrix due to its tendency to agglomerate in the solution. Performance improvement with inserted CNTs is limited by the low loading and poor homogeneity in the polymer matrix. This represents the current bottleneck in creating high-performance conductive nanocomposites. We demonstrate a novel fabrication method of conductive nanocomposites that is based on dual-material AJP (DMAJP). The demonstrated DMAJP fabrication method of nanocomposites bypasses the challenging dispersion process that hinders conventional fabrication methods when using commercially available CNT and polymer solution products as raw materials. In addition, atomization, aerosol mixing, and aerosol deposition are all potentially scalable. Thus, this

relatively facile, cost-effective fabrication method is a promising option that can be adopted by industry level, full-scale manufacturers. Moreover, the additive nature of AJP grants it unique advantages over existing methods. These advantages include the ease of patterning, affiliation with mass customization, high feature resolution, and designable, varying intra-part CNT loading levels, etc.

6.2 A Facile Method for Integrating Direct-Write Device into 3D parts

6.2.1 Introduction

Printed electronics (PE) created with direct-write (DW) techniques have advantages in that they offer mass customization, flexibility, cost effectiveness, and are more environmentally friendly [58]. A wide range of applications, including thin film transistors, solar cells, radio frequency identifications (RFIDs), antennas, sensors and displays, have been demonstrated by using PE techniques [59-65]. Three-dimensional (3D) printing also brings freedom to the process of designing and fabricating complex geometric structures that are difficult to create using conventional manufacturing processes. However, 3D printing applications are mostly limited to passive mechanical components without build-in functionality. Sharing the same technical merits, printed electronics and 3D printing are natural allies in creating multifunctional devices such as those used for sensing, energy harvesting, actuating, and structural health monitoring in 3D smart structures.

With the rapid advancement of manufacturing technologies, researchers are exploring the idea of integrating DW devices into 3D printed parts to create all-printed smart structures [66]. Studies by Palmer, Medina, Lopes and Wicker offer demonstrations of integrating

stereolithography-based 3D printing and micro-dispensing DW techniques. Their work allows for embedding electronic components and deploying conductive interconnects for various prototype devices, including a power supply circuit [67], video camera and transmitter [68], and timer circuit [42, 69]. Castillo *et al*. [70], from the same research group, extended the work to include the creation of a conformal substrate used to fabricate an accelerometer helmet insert.

Other integration studies have provided examples of 3D substrates fabricated by a fused deposition modeling (FDM) process. Vogeler *et al*. conducted an initial study for direct depositing silver ink with an aerosol jet printer on FDM substrate [71]. With a similar approach, Optomec unveiled an FDM UAV prototype with an aerosol-jet printed antenna, sensors and interconnects [72]. Espalin *et al*. demonstrated embedding a copper wire conductor into FDM substrate through ultrasonic welding and joule heating for use in a cube satellite application [73]. In addition, Perez *et al*. integrated a syringe dispenser into a Polyjet printer for depositing a conductive paste with a high loading of metal [74].

One of the major challenges presented by depositing conductive inks onto 3D printed parts is the high level of surface roughness. For most 3D printing processes, especially the extrusion-based process such as FDM, small "trenches" are formed in the direction the printer is moving across the surface. When liquid inks are used, the ink spreads into the trenches under the capillary effects and causes wicking. Additional surface polishing is usually required before depositing conductive inks.

Another challenge in using conductive inks is the elevated sintering temperature required for most situations. Most polymeric materials have heat deflection and glass transition

temperatures that are below the optimal sintering temperature required for the DW process. Lower sintering temperatures result in high electrical resistivity of printed features, which is undesirable for most applications. Using specialized high temperature materials can overcome this issue [42, 67-70, 73]. However, there are only a few materials currently available in the 3D printing market (e.g. Somos ProtoTherm and Stratasys ULTEM). These materials are expensive and require a high-end 3D printer for processing. Alternative sintering methods using microwave [75], laser [76], and photonics [77] were developed to provide an instant source of local heating to prevent substrate damage. Table 12 summarizes the resistivity for these sintering methods. Because of insufficient penetration depth, higher resistivity values of the printed tests were observed for these alternative methods. It was also observed that the sintering performance of these methods is sensitive to the z-axis distance from an energy source to the substrate, which can vary significantly for 3D printed structures.

Table 12: Summary of resistivity of printed features using different sintering methods.

Sintering Method	Resistivity (ρ)	ρ/ρ_{Silver} ($\rho_{Silver}=1.59x10^{-8}$)
Thermal Sintering at 200°C	$3x10^{-8}$	1.89
[75] Microwave Sintering	$3x10^{-7}$	18.87
[78] Laser Sintering	$5.41x10^{-8}$	3.40
[79] Photonic Sintering	$5.60x10^{-8}$	3.52

Another important, but often overlooked, issue in depositing conductive ink during a 3D printing exercise is the extensive pause needed for the DW process during the layer-by-layer (LBL) fabrication. This pause can cause weaker interlayer bonding and yield structural weak points. Some DW processes, like aerosol jet printing (AJP) or inkjet printing, require raster filling to create a filled shape. Also, two or more repetitive layers

are usually required to achieve the desired thickness and conductivity. The ink deposition alone could take hours for devices with moderate geometrical complexity, which is usually followed by another lengthy sintering process.

In this study, we found an easier way to fabricate smart 3D objects using a print-stick-peel (PSP) process. The PSP process does not require any fabrication on the target 3D-printed substrate, so it circumvents the fabrication challenges of surface roughness and sintering temperature as mentioned above. In this method, conductive patterns are first printed on low surface energy substrates that have high glass transition temperatures such as polytetrafluoroethylene (PTFE) or perfluoroalkoxy alkanes (PFA). Then they are sintered at the desired temperature to obtain optimal conductivity. Using the interfacial adhesion strength difference between the DW-printed and 3D-printed substrates, the printed pattern can be easily transferred using the self-adhesion of 3D-printed structures or additional adhesives. Similar approaches are widely used for fabricating macro/nanoscale silicon-based devices onto flexible substrates[80, 81]. However, there are no demonstrations that transferring DW-printed functional devices to 3D-printed surfaces/structures is a workable solution. Using the PSP method does not directly deposit liquid inks on the surface. Instead, a thin metal structure is transferred in its solid form, which minimizes the adverse effect of the high surface roughness of 3D printed parts. In a more severe situation where the high surface roughness causes weak bonding between the DW printed pattern and the 3D printed substrate, a thin layer of adhesives can be used as filling material to smooth out the trenches and strengthen the bonding. The temperature incompatibility is also eliminated since the DW printed structures are sintered before being attached to the 3D printed part. In addition, the transfer method

allows both DW and 3D printing and fabricating to happen in parallel with each other. The pausing of the 3D printing process is only needed for transferring the sensor structures. Thus, the pausing time is significantly reduced and the interference of inter-layer bonding can be minimized. It should be noted that this approach also applies to other non-DW printing techniques for fabricating conductive features, such as screen and gravure printing. To demonstrate the effectiveness of this approach, printed strain gauges were integrated into 3D-printed parts fabricated by Polyjet® technology. The sensor's sensitivity, reliability, and its effect on mechanical properties of the base structure are investigated and discussed.

6.2.2 Experiments

6.2.2.1 Materials and Equipment

In this study, we demonstrate our method by transferring printed strain sensors into 3D-printed dog-bone coupons. The ink used to print the strain sensors was UTDAg Conductive Silver Nanoinks® (UT Dots, Inc.). The size of silver nanoparticles in the ink was about 10 nm. Silver concentration was 60 wt% in hydrocarbon solvent. The substrates for the strain sensor before transfer were polytetrafluoroethylene (PTFE) and perfluoroalkoxy alkanes (PFA) films (McMaster-Carr Supply Co.). As an optional adhesive layer, an ink of 5 wt% polyvinylalcohol (PVA)/water was used. An Optomec, Inc. aerosol jet printing (AJP) machine 300® was used to fabricate the strain sensors. The 3D-printed coupons were fabricated with a Stratasys Ltd. Connex 350® 3D printer. The 3D printing material used for fabricating the coupons was VeroClear® (a transparent resin), also from Stratasys.

6.2.2.2 Sample Preparation and Characterization

The designed and fabricated samples of strain sensors are shown in Figure 46. Five sensors were fabricated with a 300µm printing nozzle using three passes for each sensor. PTFE and PFA films were used as substrates for their low surface energy (PTFE: 20 mN/m, PFA: 16 mN/m) [82]. The printed sensors were sintered in an oven at 200°C for 30 minutes. After sintering, the thicknesses of the sensors were measured with a P-7 Stylus Profiler (KLA-Tencor) and the resistance values were measured by an EXTECH 65EA multimeter with flat clamps at two electrodes. When the surface on which the sensors are transferred do not have enough surface adhesion to bond the sensors, a polymeric adhesive layer is deposited on top of the printed conductive ink layers for ease of transfer. The procedure of sensor preparation is illustrated in Figure 47.

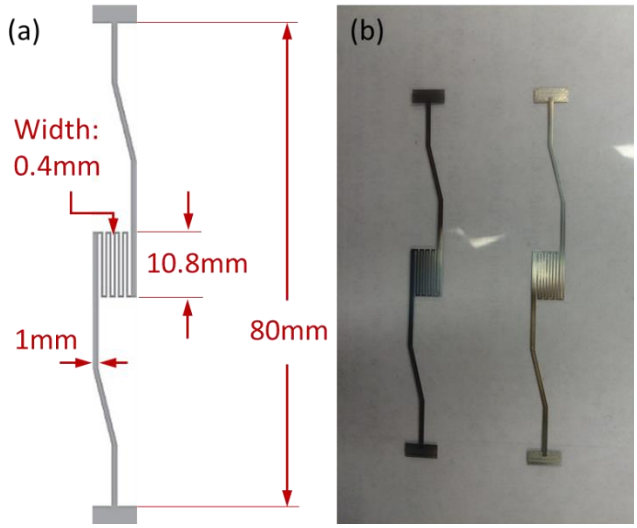

Figure 46: Printed strain sensors: a) dimensions; b) printed sensors on PFA film.

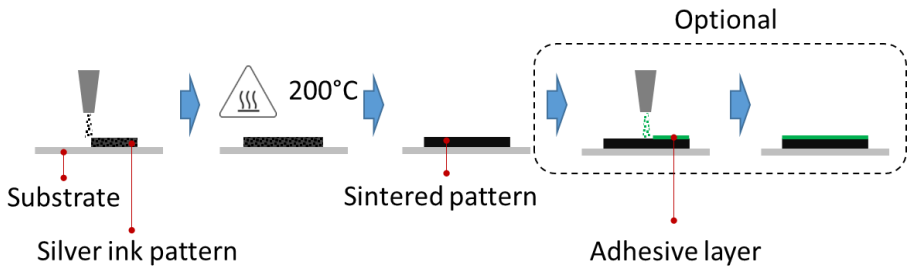

Figure 47: Procedure for preparing printed sensors.

The dog-bone shaped coupons were printed with the design shown in Figure 48. The printing procedure was paused when the thickness reached half of the total thickness and the sensors were transferred to the middle layer. When the sensor is transferred immediately after the 3D printing is paused, the adhesive layer is not required since the residual resin on the surface of the half-printed coupon is sticky enough to pull the silver pattern from the low-surface-energy substrate film. However, if there is a long idle time (>10 minutes) before the sensor is transferred, the additional adhesive layer can significantly improve the success rate of the sensor transfer. A polyvinyl alcohol (PVA) solution was used as the adhesive material in this experiment due to its solution processablilty and its compatibility with the aerosol jet printer. The adhesion strength between the printed silver pattern and the surface of VeroClear parts after transfer was previously investigated using ASTM D3359 standard tape testing. The adhesion strength of a transferred pattern without adhesive was 4B, whereas the adhesion strength of a transferred pattern with adhesive was 5B.

As shown in the coupon design, the lower half of the coupon has two apron stages at both ends to support electrodes. After the sensor transfer, the printing process resumed. The entire printed pattern was covered by the upper half of the coupon, except for the two

electrodes. The 3D printing was resumed at the same layer where it was paused. The sensor on the lower half of the coupon caused no observable interference with the printing process since the thickness of the printed sensor (~2µm) was only a fraction of the thickness resolution of the 3D printer (~16µm). The coupon preparation procedure is illustrated in Figure 49.

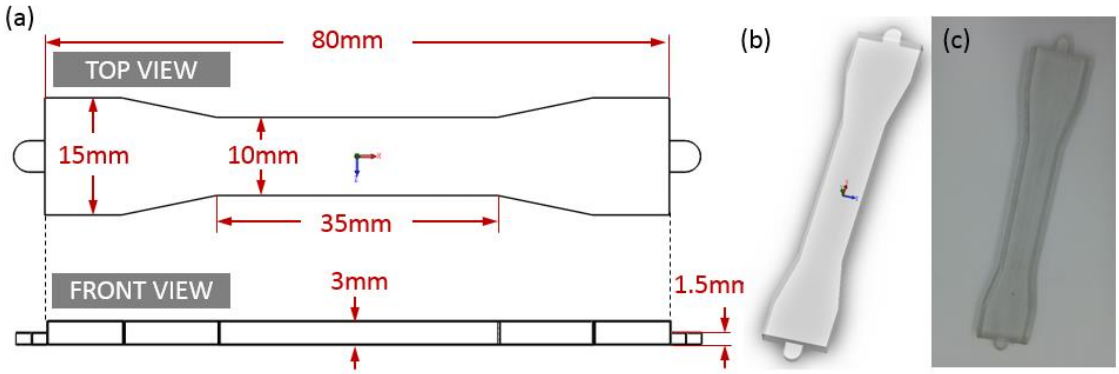

Figure 48: 3D printed dog-bone coupon: a) dimensions; b) Solidworks 3D design model; c) printed coupon.

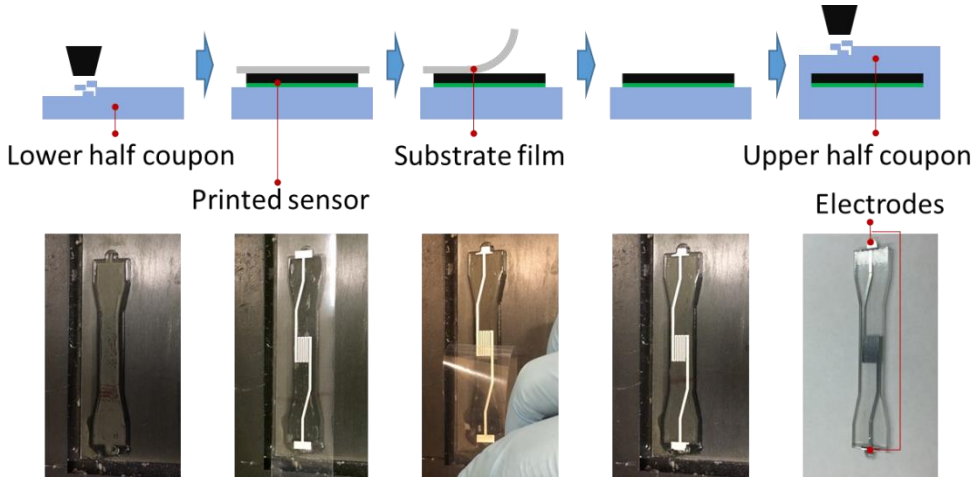

Figure 49: Preparation procedure of the 3D printed dog-bone coupon with printed strain sensor embedded. PFA film was used as substrate for its transparency.

The resistance of the five sensors was measured again after being transferred onto the 3D-printed coupons. The results are summarized in Table 13. Small increases in resistance of the sensor after transfer were observed for all five samples. This was expected since a 100% transfer rate cannot realistically be attained. The samples fabricated on the two different substrates showed no significant resistance difference. The samples with an adhesive layer (S3 and S5) had a slightly higher resistance than the other samples. However, the increase in resistance after the transfer was smaller for samples with an adhesive layer because they received a more thorough ink transfer.

Table 13: Summary of thickness and resistivity for five samples on different substrates with and without an adhesive layer.

Sample Number	**Substrate of Printed Pattern**	**Adhesive Layer**	**Thickness of printed Pattern (μm)**	**Resistance between Electrodes (Ohm)**	
				Before Transfer	After Transfer
S1	PTFE	No	2.15±0.07	8.8	9.7
S2	PTFE	No	1.89±0.11	10.3	10.9
S3	PTFE	Yes	2.81±0.13	12.8	13.0
S4	PFA	No	2.06±0.09	9.6	10.2
S5	PFA	Yes	2.63±0.11	13.4	13.5

Figure 50 shows the optical microscopy (OM) and scanning electron microscopy (SEM) images of the cross section of sample S5. According to the images, the thickness of the printed silver pattern remained the same after the upper half of the coupon was printed. The continuity of the coupon along with the thickness direction was intact except for the area where the printed pattern was located.

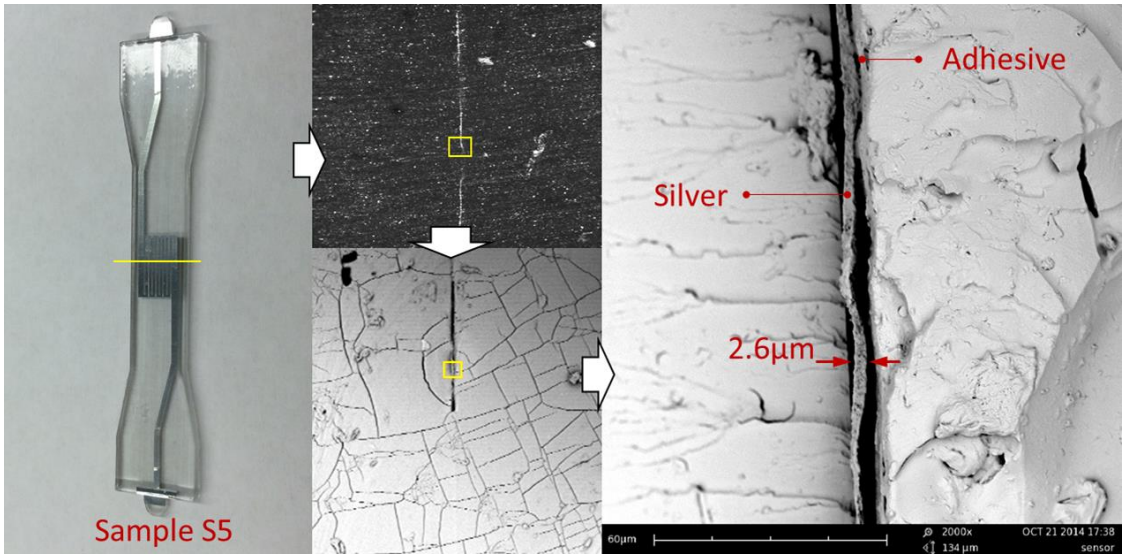

Figure 50: OM and SEM images of a cross section of coupon sample S5 showing the layer of embedded silver pattern.

6.2.2.3 Sensor Performance Test

Cyclic loading tests were conducted on S1-S4 samples to test the effectiveness and robustness of the embedded sensors fabricated with the new method. Two copper wires were attached to the electrodes at both ends of each sample using silver epoxy as the bonding material, as shown in Figure 51. The copper wires were connected to an analog data acquisition board (NI-9219) (National Instruments Corp.), which sent the resistance reading to a computer and displayed it in a LabVIEW program.

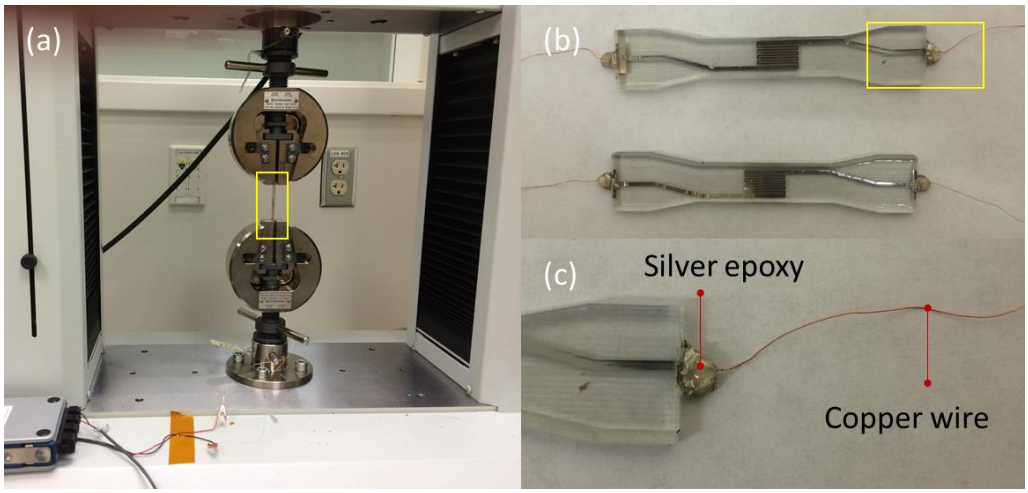

Figure 51: Experimental setup for cyclic loading test: a) a sample mounted on SHIMADZU precision universal tester with leads connected to NI-9219 analog data acquisition board; b) samples with wired electrodes; and c) zoomed view of a wired electrode.

The test cycle started at a relaxing state when the load upon the sample equaled zero. An extension force was then applied so that the distance between the two clamps increased at a rate of 0.5mm/s for 4 seconds. After the stroke reached the maximum (2mm), it changed and decreased at 0.5mm/s for 4 seconds until it was back to the relaxing state. All samples were preloaded for 100 cycles to allow granular boundaries in printed trace to form and stabilize. After the 100 initial "run in" cycles, each sample was tested for another 1500 cycles. The resistance of the printed strain sensor was recorded at a sampling rate of 20Hz, yielding 160 data points per cycle.

6.2.3 Results and Discussion

The electromechanical properties of the embedded strain sensor were assessed by the results of cyclic loading test. Figure 52 shows a constant peak-to-peak value of the printed strain sensor in sample S1, indicating that the sensor signal is very reliable and

repeatable. The maximum strain is over 4%, which is comparable to commercial metal foil strain sensors. The gauge factor (GF) was calculated by:

$$GF = \frac{\Delta R / R_0}{\varepsilon} \tag{47}$$

where GF is the gauge factor, ΔR is the change in resistance, R_0 is the initial resistance, and ε is the strain of the printed sensor. The transferred strain sensors had a reliable mean strain GF of about 11.4 ± 0.06 when strain is around 4%, which is much higher than the GF of commercial metal foil strain sensors (~2). The high GF of the transferred sensor occurs because the strain sensing mechanism of the aerosol printed sensor is different from that of the metal foil sensor. The resistance change of the printed sensor is mainly due to widened gaps and micro-cracks between grain boundaries of annealed silver nanoparticles when the sensor is under strain, while the resistance change of the metal foil sensor is due to the deformation of bulk metal. This mechanism is similar to that of the nanoparticle strain sensor, which has an even higher GF of around 100 [83]. The difference is that the grain size in aerosol jet printed trace is at a micro level because of sintering, not at a nano level as with the nanoparticle strain sensor. The GF of transferred samples are in the same magnitude of sensors that use silver nanoparticle as conductive materials [84, 85].

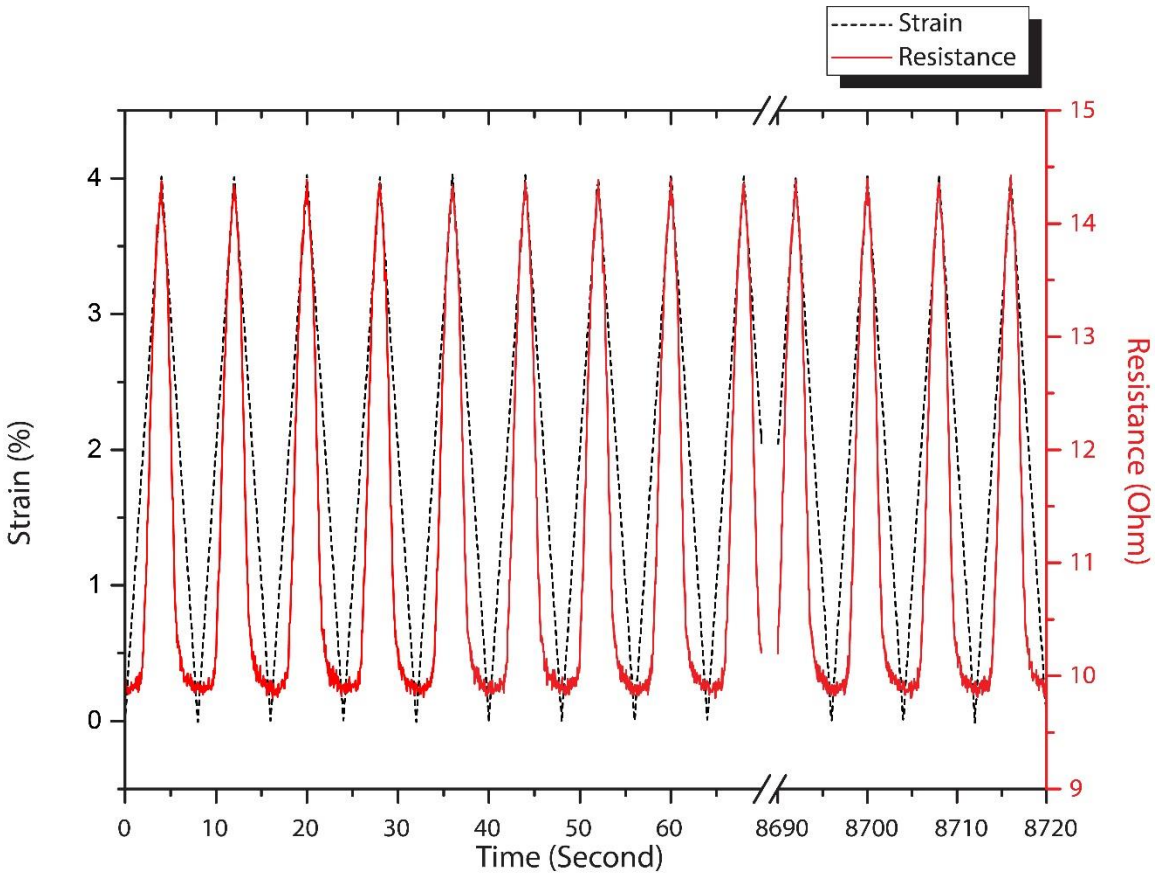

Figure 52: Cyclic loading test result of strain and resistance change as a function of time for sample S1. The resistivity change kept constant after1000 cycles.

One of the drawbacks of the resistance change is the nonlinear response to the strain change, i.e., the GF is not a constant at different strain levels. This effect is more obvious when the strain is at lower levels, as shown in Figure 53. Another drawback is that more micro-cracks may form during stretching, causing an increasing change in resistance over time. Therefore initial "run in" cycles are necessary for the cracks to form and stabilize.

The comparison of resistance change of four samples is shown in Figure 53. The results are mostly consistent with a smaller response for S3, where the adhesive layer was used. We believe the reason is that the adhesive layer hindered the growth of micro-cracks.

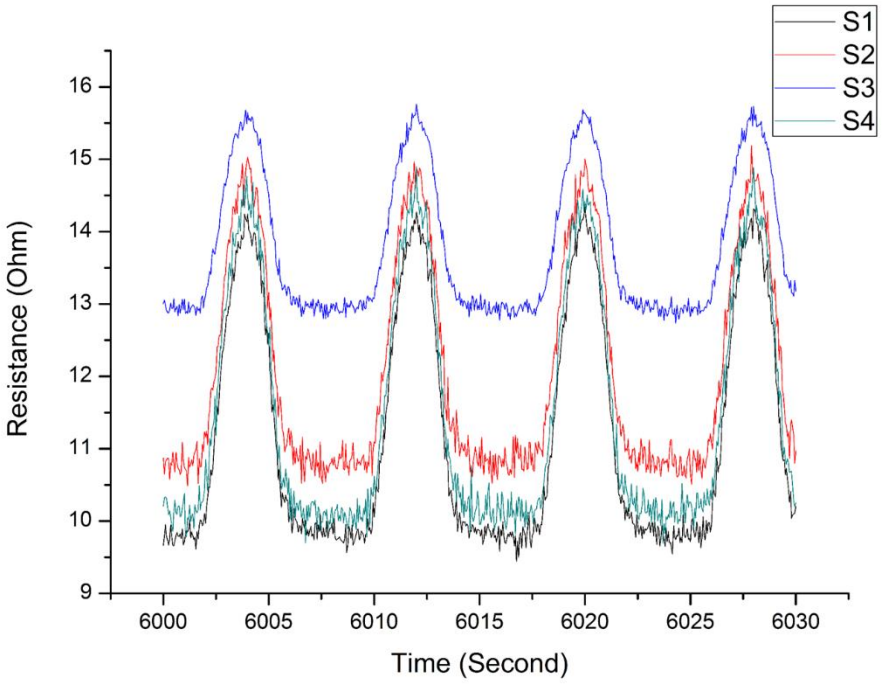

Figure 53: Resistance change of four samples. S1, S2, and S4 are comparable with small resistance variations. S3 has a smaller response due to the usage of an adhesive layer.

Other than strain sensors, the PSP transfer method also allows for integrating other functional devices into structures fabricated with 3D printing or other layer-by-layer (LBL) processes, such as the hand lay-up process for composites. It can also transfer printed devices into rubber-like materials to fabricate flexible electronics, provided that the local strain does not exceed the limit of printed traces. It is also possible to transfer devices onto curved surfaces. Figure 54 demonstrates a few applications using this transfer method including a) a pressure sensor transferred onto a 3D-printed aorta heart valve surface; b) strain sensors and an antenna transferred onto the internal surface of a prosthetic socket; and c) a strain sensor embedded into a 3D-printed rubber-like material (TangoPlus®, Stratasys).

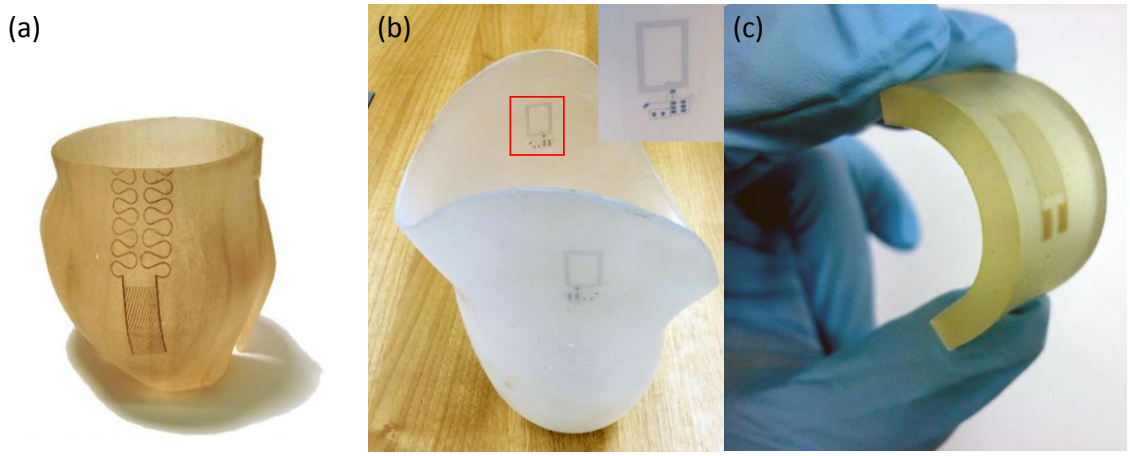

Figure 54: Applications of PSP transferred DW devices: a) a pressure sensor transferred onto a 3D-printed aorta heart valve; b) An antenna transferred onto the internal surface of a prosthetic socket; and c) a strain sensor embedded into 3D-printed flexible mater

Although most DW processes are at a relatively low production rate compared with industry level LBL manufacturing, the scalability of this PSP process is high due to the independency of the DW device preparation step. In other words, the DW process and 3D printing process can work in parallel instead of in a sequence. A continuous tape with repeated DW printed patterns can be prepared and stocked in advance for high speed LBL fabrication. With the help of automatic alignment and handling, which can be easily implemented in an industrial level manufacturing environment, the transferring step can be done in a short time. A schematic diagram of PSP-enabled continuous manufacturing for smart structures is shown in Figure 55.

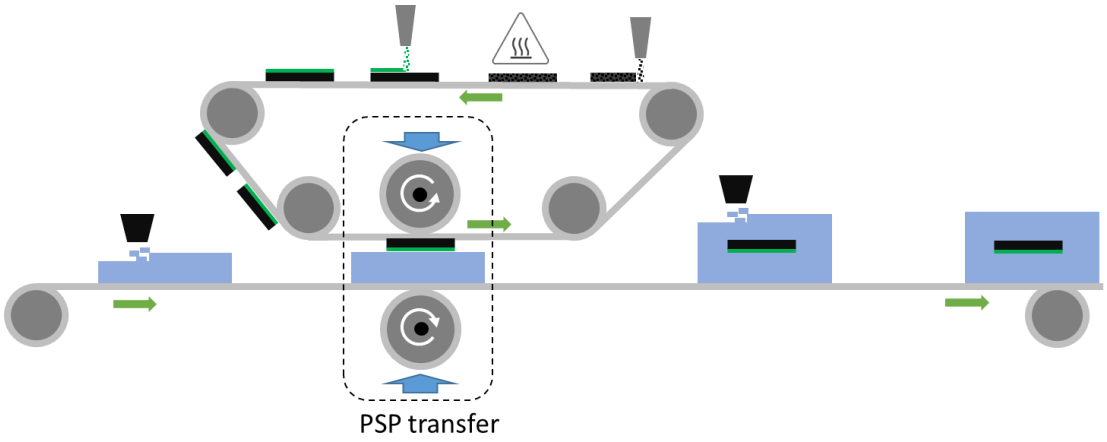

Figure 55: Schematic of the PSP-enabled continuous manufacturing for smart structures.

6.2.4 Conclusion

In this study, a facile print-stick-peel transfer method was developed and tested to integrate DW devices into 3D-printed structures. This method leverages a different adhesive force to the printed trace between the print substrate and the transfer surface to achieve pattern transfer during 3D printing. The repeatability and reliability of this method was validated by transferring aerosol jet printed strain sensors onto the intermediate layer of 3D-printed coupons. This method allows the printed trace to be embedded into the 3D-printed part or onto its surface, without affecting the integrity of the part. As the thickness of the aerosol jet-printed device is much smaller than the layer thickness of 3D printing, no pre-designed or prepared cavity is required. Both printed electronics and 3D printing technologies have high flexibility in terms of design and customization. This new method takes advantage of both and provides a practical manufacturing technique for making multifunctional smart structures. In addition, since

the DW device preparation is independent of the 3D printing process, the PSP transfer method has great potential for scalable manufacturing of smart structures.

6.3 Conductive-on-Demand: Tailorable Polyimide/Carbon Nanotube Nanocomposite Thin Film by Dual-Material Aerosol Jet Printing

6.3.1 Introduction

Carbon nanotube reinforced polyimide nanocomposites (PI/CNT) have great potential for use in the aerospace industry because of their high mechanical properties, electrical conductivity, high-temperature endurance, and resistance to ultra-violet (UV) decomposition[86, 87]. However, conventional fabrication methods of PI/CNT nanocomposites require dispersion of CNTs into the PI matrix, which is a challenging processing step because even a small percentage of CNT would greatly increase the viscosity of the polymeric solution [88-90]. Worse yet, dispersion-based fabrication often yields a heterogeneous distribution of CNTs in the PI matrix due to its tendency to agglomerate in the solution. Performance improvement with inserted CNTs is limited by the low loading and poor homogeneity in the PI matrix. This represents the current bottleneck in creating high-performance PI/CNT nanocomposites. Extensive research efforts have been dedicated to overcoming the difficulties in the dispersion of CNTs in a polymeric matrix. One of the most successful methods is to use chemical functionalization to increase interfacial interactions between the CNTs and the polymeric matrix [91, 92]. While the carboxyl groups introduced to the functionalized CNT do increase the homogeneity of CNT suspension, the strong mixed-acid treatment may breach the integrity of the pristine CNTs and compromise their mechanical or electrical

properties. Other covalent functionalization methods also have been investigated [93-97]. Similarly, those methods disrupt conjugation within the CNTs by converting side-wall carbons from sp2 to sp3 hybridization, which results in reduced electrical conductivity and mechanical properties. Alternatively, noncovalent functionalization methods, which use highly aromatic molecules to wrap CNTs, have proven quite effective [98-101]. High-performance PI/CNT with up to 9 wt% loading level has been fabricated using aromatic functionalization [102]. A variation to this method is first to disperse CNTs, pristine or functionalized, into a solution of certain precursor to PI, *e.g.* poly(amic acid) (PAA) [103-105] or polyisoimide (PII) [106, 107], then to synthesize the nanocomposite via *in situ* polymerization. The *in situ* polymerization process requires precisely controlled conditions for a series of reactions, which increases complexity, duration and cost of the fabrication of PI/CNT.

Some fabrication methods of PI/CNT that are not dispersion based have also been reported. The most studied technique of those is spray winding. The typical process is to spray PI or its precursor onto a CNT sheet that is continuously pulling out from a chemical vapor deposition (CVD) grown forest [87]. A more recent technique is direct infiltration of PAA solution into a CVD grown CNT sheet [108]. Those methods yield very high CNT loading levels and are capable of achieving a high degree of alignment. This results in stronger and more conductive nanocomposites than their low CNT loading level counterparts. However, those methods all require CVD to grow a CNT forest as the raw material. Due to the fact that most commercialized CNT products are in the form of powder or solution, the scalability of those fabrication methods is limited by the slow and costly CVD growth of the CNT forests.

In this section, we demonstrate a novel fabrication method of PI/CNT that is based on dual-material aerosol jet printing (DMAJP). Aerosol jet printing (AJP) is a branch of emerging additive manufacturing (AM) technologies. Developed in 2007 to fulfill the increasing demand for miniature and flexible electronics [109, 110], it atomizes solutions or suspensions into aerosols with a droplet size ranged from 0.5 to 3.0 μm. It then deposits the aerosol onto substrates with a focusing sheath gas flow [111]. With a similar working principle, our method aims to achieve good CNT distribution in the PI matrix by mixing aerosols of CNT suspension and PAA solution. The mixture of aerosols is deposited onto a heated substrate. The substrate is then put into an oven for curing. The detailed description of this method is presented in section 6.2.2.

The demonstrated DMAJP fabrication method of PI/CNT totally bypasses the challenging dispersion process that hinders conventional fabrication methods, while using commercially available CNT and PAA solution products as raw materials. In addition, atomization, aerosol mixing, and aerosol deposition are all potentially scalable. Thus, this relatively facile, cost-effective fabrication method is a very promising option that can be adopted by industry level full-scale manufacturing. Moreover, the additive nature of this fabrication grants it unique advantages over existing methods. Such advantages include the ease of patterning, affiliation with mass customization, high feature resolution, and designable varying intra-part CNT loading level, *etc.*

6.3.2 Experimental

6.3.2.1 Materials and Equipment

The multi-wall CNT ink used in this study was purchased from Nanostructured & Amorphous Materials, Inc. (product number: 8039RB). The specifications of this ink are 3 wt% multi-wall CNT (length: 100μm; diameter: 10-40 nm) in n-methyl-2-pyrrolidone (NMP) solvent. The PAA solution was purchased from Sigma-Aldrich Co. LLC. (product number: 575771). It is 12.0 wt% poly (pyromellitic dianhydride-co-4,4'-oxydianiline) amic acid solution with a mixture of 80% NMP and 20% xylene as solvent. To achieve the optimized atomization, the concentrations of the CNT ink and the PAA solution were adjusted to 1% and 10%, respectively, by adding pure NMP solvent (Sigma-Aldrich Co. LLC., product number: 328634). An AJP 300® aerosol jet printing machine (Optomec, Inc., Albuquerque, NM), modified to enable dual-material atomization and aerosol mixing, was used to demonstrate the fabrication method. A P-7 stylus profiler (KLA-Tencor, Milpitas, CA) was used to measure the thickness of the nanocomposite samples. A Ultra60® field emission scanning electron microscopy (FE-SEM) (Zeiss USA, Dublin, CA) was used for the microstructure characterization. A PE-25 plasma system (Plasma Etch, Inc., Carson City, NV) was used to etch the surface of the nanocomposite samples and expose more CNTs. A universal probe with RM3000® test unit (Jandel Engineering, Ltd., Linslade, UK) was used for the electrical characterization.

6.3.2.2 Preparation Process of PI/CNT Nanocomposites

The dual-material aerosol jet printing setup is depicted as a schematic in Figure 56. The Optomec AJP 300 printer originally had two separate atomization options, a Collison atomizer and an ultrasonic atomizer. Determined by the viscosity, the PAA solution was processed with the Collison atomizer and the CNT ink was processed with the ultrasonic atomizer. The built-in flow regulator can control the gas flow of either atomizer. To

enable simultaneous atomization of two different types of ink, another flow regulator (MKS mass flow controller, model: GE50A) was incorporated into the system. The two aerosol streams were mixed with a static mixer. The mixed aerosol was then transported to the deposition head and deposited to a glass substrate with the assistance of nitrogen sheath gas. Thin film rectangular samples with serpentine filling were printed (Figure 57(a) and (b)). To accommodate the size requirement of the tensile testing, the lengths of all samples were 20mm and the widths were 5mm. It took multiple layers of printing to achieve the desired thicknesses. After printing, the samples were cured in an oven. After curing, the samples were removed from the glass substrate in the form of freestanding thin films, as shown in Figure 57(c).

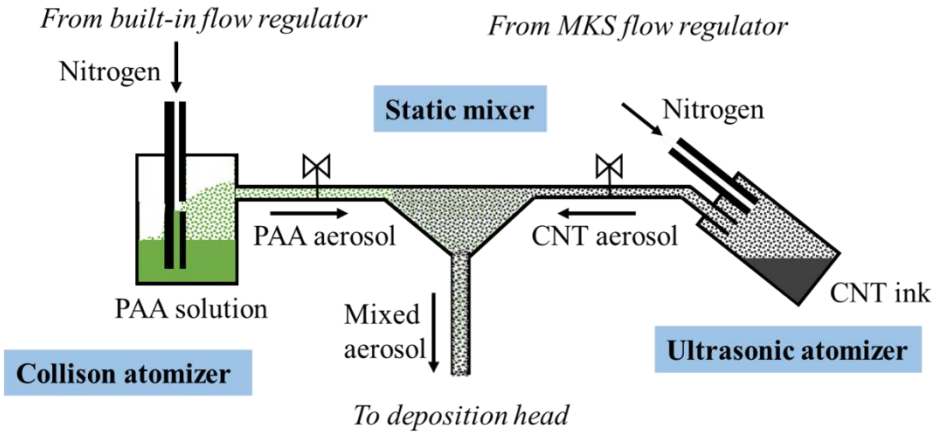

Figure 56: Schematic of dual-material aerosol jet printing

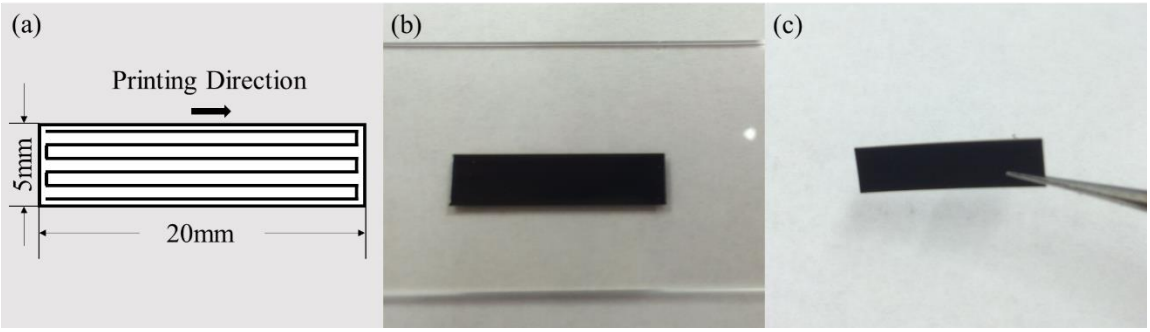

Figure 57: Dual-material aerosol jet printed PI/CNT nanocomposite thin film: (a) sample dimensions and the printing direction; (b) an as-printed nanocomposite sample; (c) a freestanding nanocomposite sample after removed from the glass substrate

A similar setup has been used to print composite interlayers of solid oxide fuel cells [112, 113]. Although the current setup and the previous setup share the same working principle, several differences exist. The older setup uses two Collison atomizers while the current setup uses both Collison and ultrasonic atomizers to provide the capability of processing low-volume/high-cost ink, such as the CNT ink. The aerosol streams were directly mixed with a "Y" connector in the previous setup, which, according to our preliminary investigation, may result in unmixed regions if the ratio of aerosols is not around 1:1. A static mixer was added in the current setup to achieve homogeneous mixing at any flow rate ratio. The previous setup controlled the gas flows in both atomizers with one single process control module. The current setup uses two individual flow controllers. The individual control of the two aerosol streams allows on-demand material mixing and *in-situ* adjustable mixing ratio.

The properties of printed nanocomposite films are determined in large part by the configuration of process parameters. Some of those process-property relationships were investigated in this study. A default setting was defined to avoid any confusion of the

process configuration setup. Any experiments designed in this study only varied one or a few parameters, while in all other processes the parameters were fixed. The default configuration setting, based on the prior knowledge of stable flow conditions of the AJP machine, is summarized in Table 14.

Table 14: Default configuration setup of process parameters

Process Parameter	Value
Total flow rate	100 sccm
PAA aerosol	50 sccm
CNT aerosol	50 sccm
Sheath gas flow rate	90 sccm
Printing speed	8 mm/second
Standoff distance	3 mm
Nozzle diameter	300 μm
Stage temperature	60 °C
Curing procedure	60min@120°C→60min@180°C→60min@220°C
Number of layers	30

6.3.3 Characterizations

6.3.3.1 Thickness

If the flow condition is kept constant during printing, the thickness of the printed PI/CNT film is determined by the amount of the mixed aerosol deposited per unit area. Intuitively, it should be proportional to the number of layers and inversely proportional to the printing speed. A set of samples was fabricated at different process configurations to confirm this assumption. The process configurations of each sample are shown in Table 15. Five replicates were fabricated and tested for each sample for the calculation of the standard deviation. All samples were tested with the profiler at a sweep speed of 100μm/s. The sweep direction was perpendicular to the printing direction.

Table 15: Samples for the thickness characterization

Sample Code	Number of Layers	Printing Speed (mm/s)
T1 (default)	30	8
T2	15	8
T3	45	8
T4	30	6
T5	30	10

6.3.3.2 Nanostructure

The CNT loading in the printed nanocomposite film is controlled by the mixing ratio of the CNT aerosol to the PAA aerosol. The ratio of CNT aerosol to the PAA aerosol is denoted as r. The CNT loading in the samples fabricated with the default $r=1$ is 3.22 ± 0.47 wt%. O_2 plasma was used to etch a thin layer of the polyimide on top of the nanocomposite thin films so that the structure of the CNTs can be exposed and visualized in the FE-SEM pictures. For most samples, the cycle time of the plasma etching was set to 300s. Particularly, one piece of the default sample was treated for 600s so the nanostructure at a greater depth could be observed. Three samples, S1-3 with r =0.5, 1, 5, respectively, were characterized to show the difference in CNT density (Table 16).

Table 16: Samples for the microstructure characterization

Sample Code	CNT Flow Rate (sccm)	PAA Flow Rate (sccm)	r
S1	25	50	0.5
S2 (default)	50	50	1
S3	100	20	5

6.3.3.3 Electrical Conductivity

The electrical conductivity of the printed PI/CNT nanocomposite film is determined by r. Seven nanocomposite samples with various r and one sample printed with only the CNT ink were fabricated for the characterization (Table 17). The four-point Kelvin method was used to measure the electrical conductivity. All measurements were conducted in the ambient environment.

Table 17: Samples for electrical conductivity characterization

Sample Code	CNT Flow Rate (sccm)	PAA Flow Rate (sccm)	r
C1	0	50	0
C2	25	50	0.5
C3 (default)	50	50	1
C4	75	50	1.5
C5	100	50	2
C6	100	25	4
C7	100	20	5
C8	50	0	∞*

* C8 is printed by the CNT ink only, which represents the theoretical limit of the conductivity of PI/CNT nanocomposite

6.3.3.4 Tailorability of Material Structures and Properties

A unique feature of this DMAJP method for the fabrication of PI/CNT is that it is possible to control the CNT loading at different regions of one nanocomposite film. This high customizability comes from the additive nature of the manufacturing method. During printing, with the flow rate of the PAA aerosol fixed at 50 sccm, the immediate loading of CNT can be controlled by in-situ changing the flow rate of the CNT aerosol. Since the CNT loading determines the electrical conductivity of the nanocomposite, this DMAJP method is essentially a "conductive-on-demand" fabrication of PI/CNT.

Three showcase examples were designed to demonstrate this conductive-on-demand capability, each representing a specific application. The first example was fabricated to have different CNT loadings at designated regions of the same nanocomposite thin film. This is achieved by changing the flow rate of the CNT aerosol while keeping the flow rate of the PAA aerosol constant. The design of this example is illustrated in Figure 58.

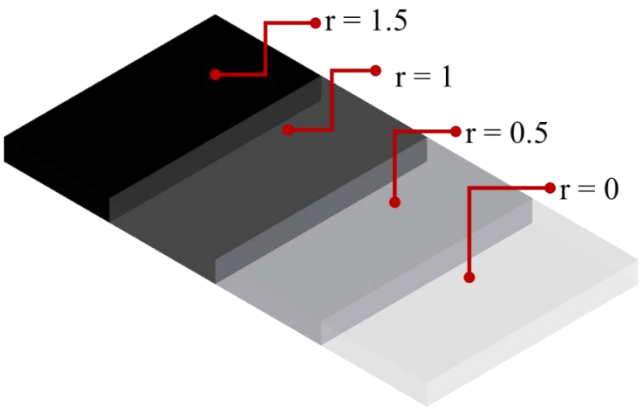

Figure 58: Design of printed PI/CNT film with different CNT loading regions

The second example was fabricated as a thin film circuit. Although the conductivity of PI/CNT nanocomposite normally is not an ideal material for circuitry due to the relatively low conductivity, this example aims to provide a manufacturing possibility for highly robust printed electronics, as the conductive trace is a fully integrated part of the substrate. This example also demonstrates the capability of free patterning of the conductive region with DMAJP. The design of this example is shown in Figure 59.

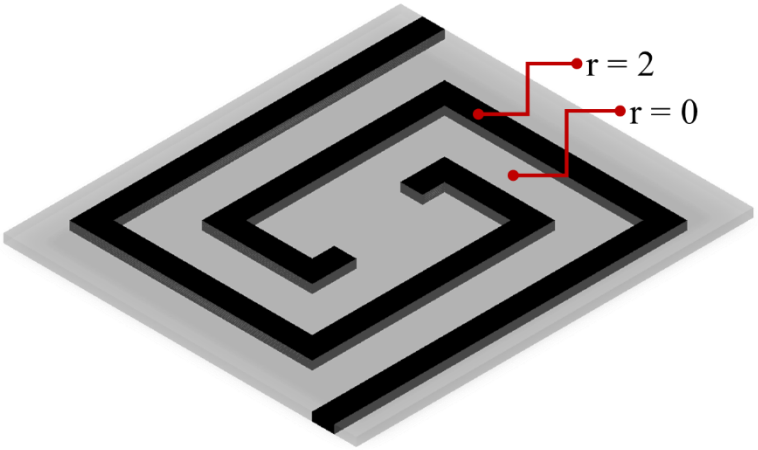

Figure 59: Design of printed PI/CNT film as an integrated circuit

The third example is to demonstrate the through-thickness conducting function, which can be used in multilayer circuit packaging. It provides conductive channels through the insulating layer without piercing the insulating layer. The design of this example is shown in Figure 60.

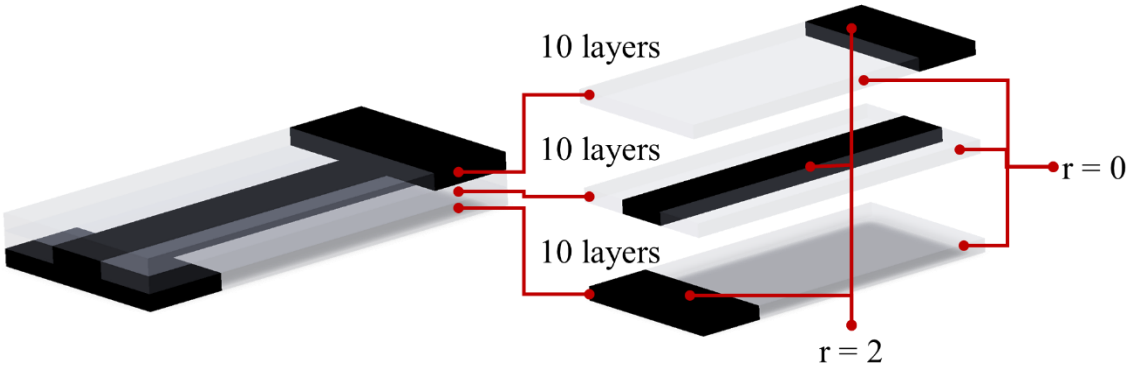

Figure 60: Design of printed PI/CNT film with through-thickness conducting function

6.3.4 Results and Discussion

6.3.4.1 Thickness

The results of thickness measurements of sample T1-5 are shown in Figure 61. The thickness of the printed PI/CNT film increases linearly with the number of layers and the inverse of printing speed if the flow condition is constant. To achieve any desired thickness, the number of layers can be used as a discrete tuning factor and the printing speed can be used as a continuous tuning factor. All samples have a similar degree of surface roughness, which may be caused by the printing path of the serpentine filling at the top layers. For a thicker sample (>40μm), the stage temperature needs to be raised for a timely solvent removal. Otherwise, the surface will have a smooth and curved profile due to the self-formation of the excessive solvent under the surface tension.

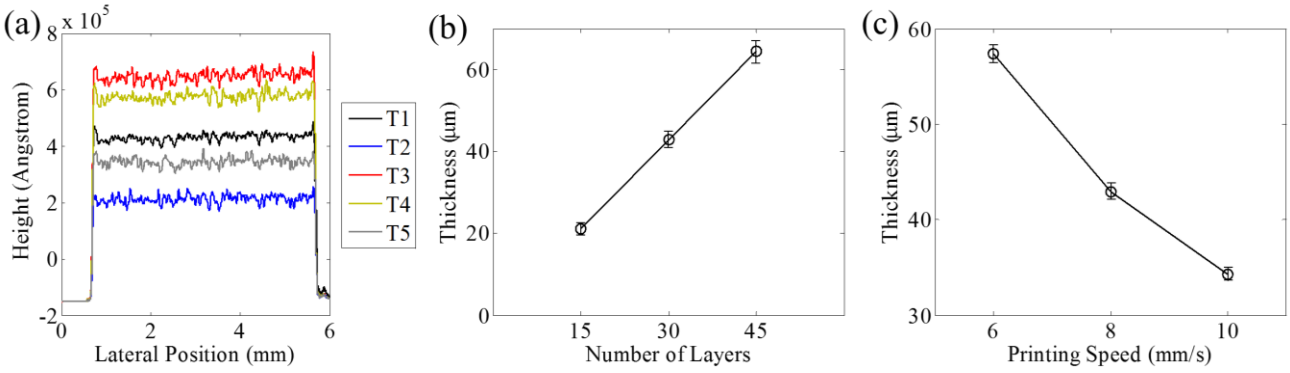

Figure 61: (a) The profiles of T1-5; (b) dependence of the thickness on the number of layers; (c) dependence of the thickness on the printing speed

6.3.4.2 Nanostructure

The SEM images of sample S1-3 are shown in Figure 62. Because the nanocomposite films were printed layer by layer, the CNTs tend to lie in one layer rather than go through multiple layers. At the low CNT loading in S1, CNTs are sparsely distributed with large pure polyimide areas in between. Since few effective conductive paths can be established at this low CNT density, the film is still an insulating material. At the higher CNT

loading in S2, the CNTs start to connect to each other and form a loose network, which suggests the percolation threshold is reached and the nanocomposite film is becoming conductive. At the very high CNT loading in S3, the CNTs form a dense network that is normally observed in buckypaper, a thin porous film formed by CNTs only [114]. The in-plane nanostructure of this high CNT loading printed film is similar to the nanocomposite that is fabricated by infiltrating buckypaper with polymeric resin [115, 116]. Figure 62(d) indicates that the dispersion of CNTs in the PI matrix is good in the through-thickness direction since similar densities of CNTs were observed at different depth in a crater created by the plasma etching.

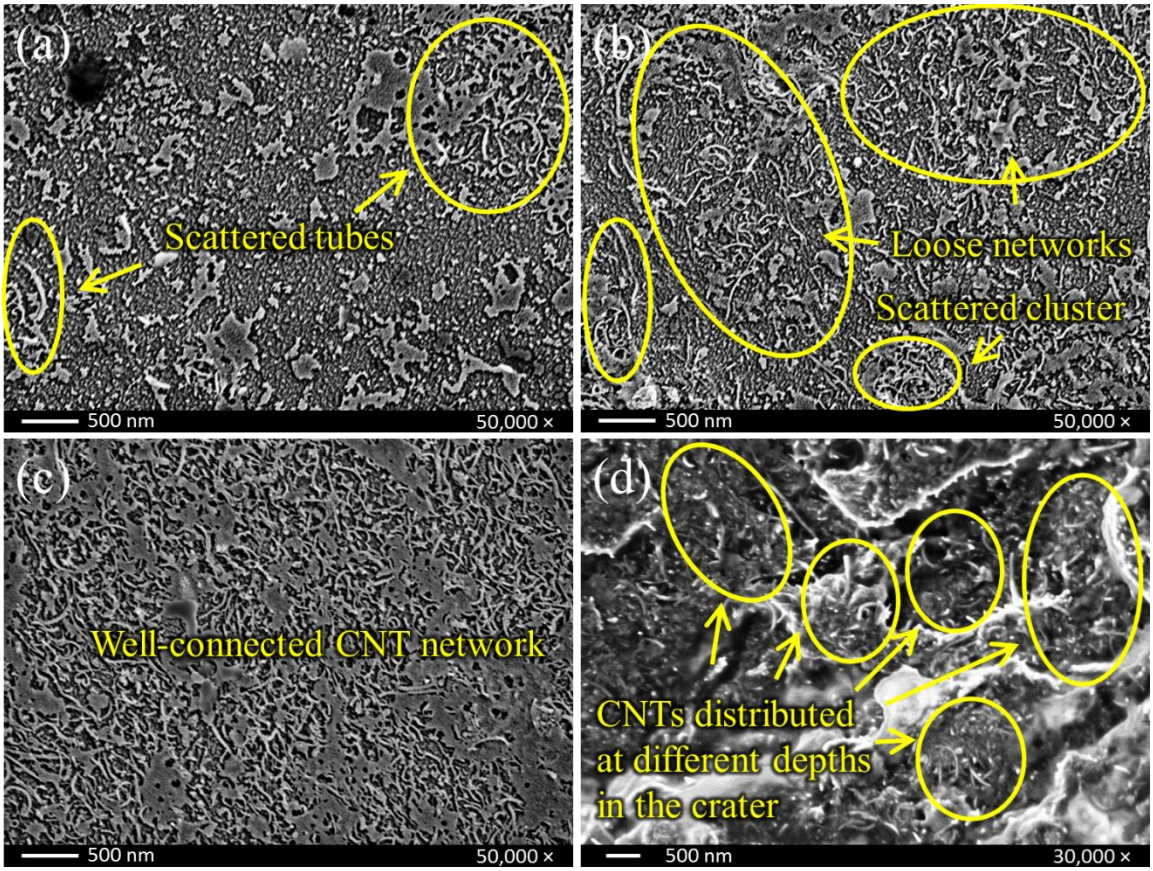

Figure 62: SEM images of PI/CNT nanocomposites: (a) S1: , 1.64 ± 0.27 wt%; (b) S2: , 3.22 ± 0.47 wt%; (c) S3: , 14.26 ± 2.81 wt%; (d) S2 with longer etching time for visualizing the distribution of CNTs inside the nanocomposite.

6.3.4.3 Electrical conductivity

The electrical conductivity of sample C1-8 is plotted in Figure 63. The conductivity of the PI/CNT nanocomposites increases with an increase in the CNT loading. The nanocomposite changes from insulating to conductive from 1.64 wt% to 3.22 wt% of CNTs, suggesting the percolation threshold is in between. This is consistent with the observation from SEM images. Beyond the percolation threshold, the conductivity of printed PI/CNT nanocomposites increases slowly as it approaches the conductivity of C8, the sample printed with the CNT ink only.

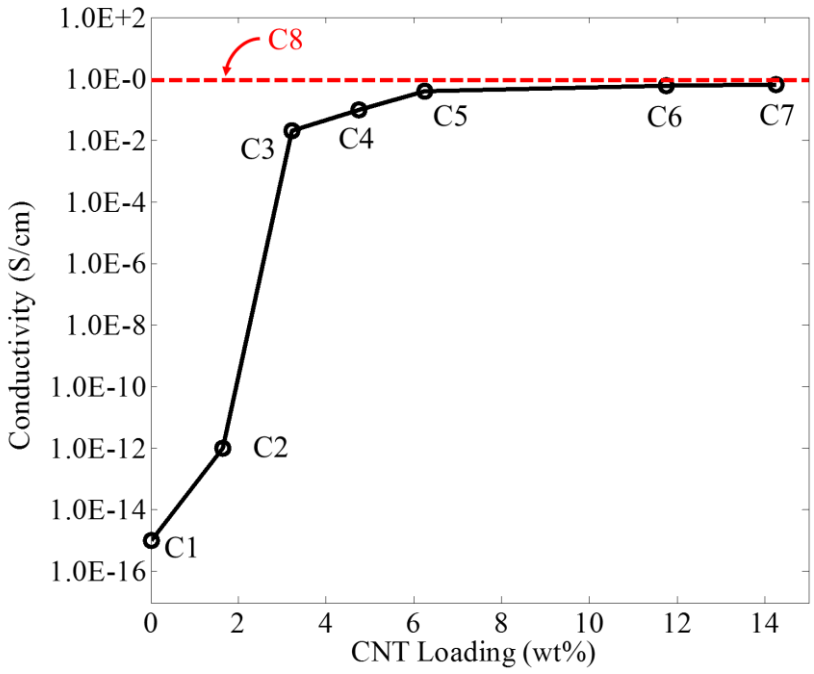

Figure 63: Dependence of electrical conductivity on the CNT loading in PI/CNT nanocomposites

6.3.4.4 Demonstration of customizability

The printed PI/CNT nanocomposite film with different CNT loading regions is shown in Figure 64(a). The flow rates of the two aerosols are plotted in Figure 64(b). The width of each panel was set to 5mm in this example. As the width of the printed line can be as thin as ~20µm, it is possible to print hundreds of tiny panels with a width less than 100µm and a small step size in the CNT to form a nanocomposite film with "quasi-gradient" conductivity.

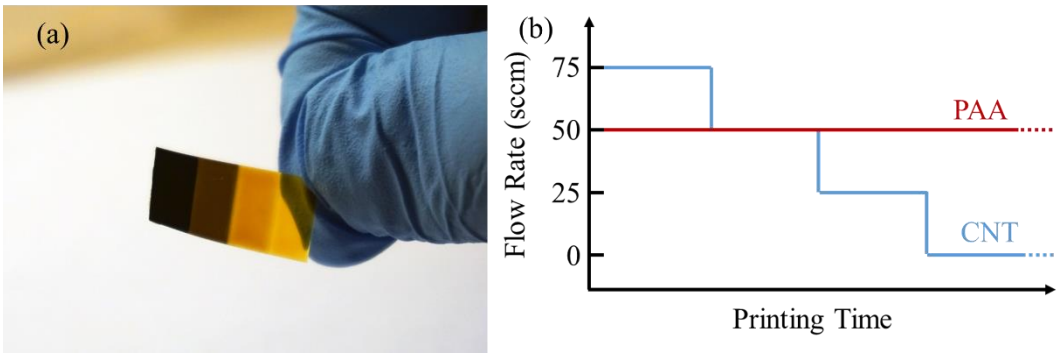

Figure 64: (a) A printed PI/CNT nanocomposite film with four different CNT loading regions; (b) The flow rates of the two aerosols during printing

The printed thin film circuit is shown in Figure 65(a). A simple circuit testing with a light-emitting diode (LED) was demonstrated (Figure 65(b)-(d)). As DMAJP is an additive manufacturing technology, the conductive pattern can be freely designed for other direct-write technologies such as inkjet printing [117] and dispenser printing [118]. An unrivalled advantage of DMAJP over other direct-write technologies is its ultra-high robustness. As the conductive path is built with the substrate instead of on the substrate, it can be bent, folded, stretched, washed, or even scratched with the substrate and remain conductive. In fact, the conductive path is even stronger than the substrate because of the CNT reinforcement. It is also important that this high reliability is achieved by a one-step fabrication without any post-processing.

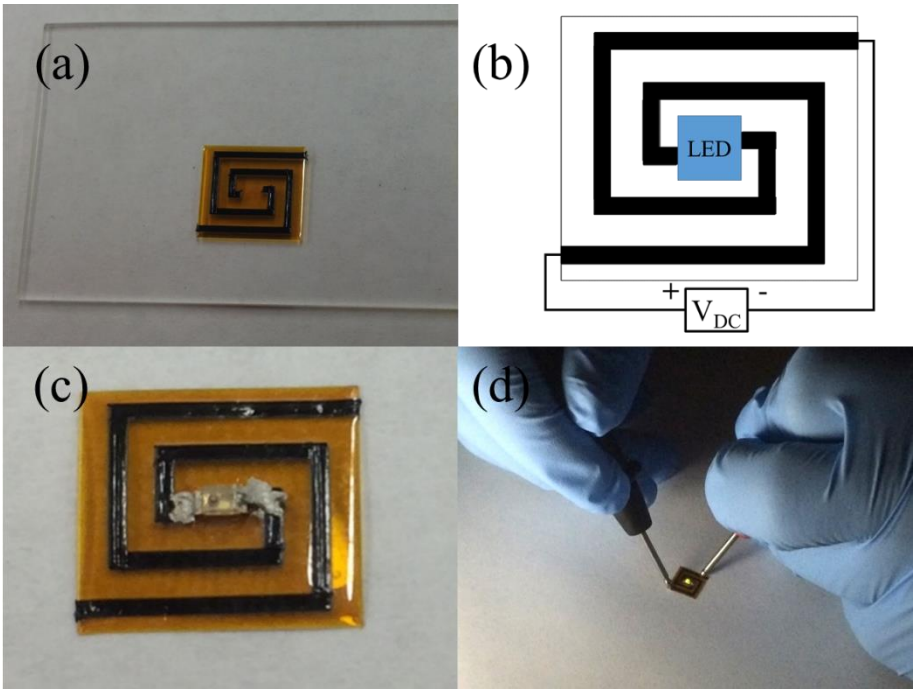

Figure 65: Demonstration of a printed PI/CNT nanocomposite circuit: (a) the as-printed nanocomposite circuit; (b) the schematic diagram of a simple circuit testing; (c) the freestanding nanocomposite circuit with an LED mounted with silver glue; (d) the LED lighted with a 60V_{DC} power supply

The printed nanocomposite film with through-thickness conducting function is shown in Figure 66(a). This was validated by demonstrating that a conductive path exists between point A and point B while point C is insulated, as shown in Figure 66(b)-(d). The through-thickness conducting function is useful in multilayer circuit design where interconnections between layers are desired. Currently, the interlayer connection is usually achieved through small vias [119, 120], which introduce mechanical weak spots in the substrate. Although these weak spots are negligible in conventional electronics, they become more significant in flexible thin film electronics as they are potential stress concentration locations under stretching. The through-thickness conducting channel built in the nanocomposite film has no such problem because the continuity of the film is intact.

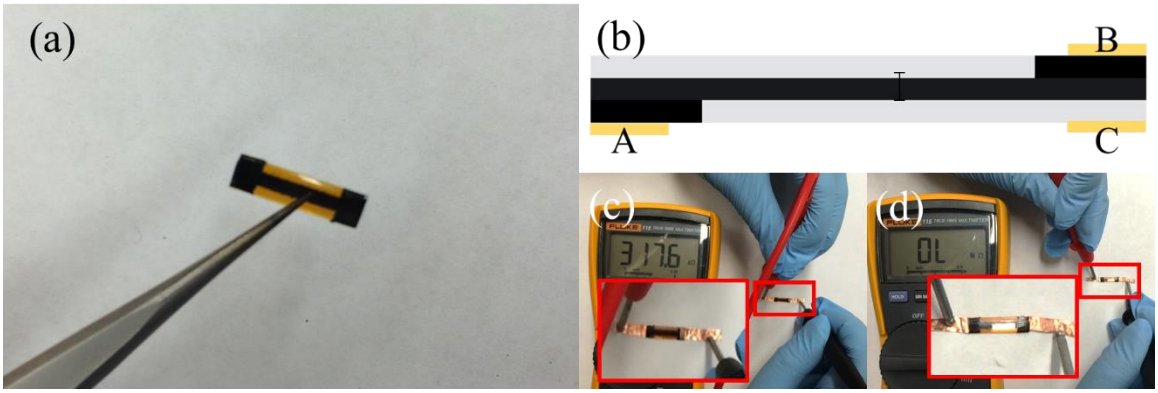

Figure 66: Demonstration of through-thickness conducting function: (a) the printed PI/CNT film with through-thickness conducting channel; (b) the locations of copper tape electrodes for validation (c) the resistance between electrodes A and B is RAB = 317.6 kΩ; (d) there is no conductive path between electrodes A and C

6.3.5 Conclusions

In this study, highly tailorable PI/CNT nanocomposite films were fabricated with a novel DMAJP process. The capability of freely changing the CNT loading during DMAJP is demonstrated. This unique feature allows nanocomposite films to have different conductivities at different regions, which enables many interesting functions such as gradient conductivity, built-in-substrate circuit, and through-thickness conductivity. Currently, this DMAJP method is demonstrated with a modified Optomec AJP300 machine designed to fabricate miniaturized printed electronics. Therefore, the product dimension and production rate are limited. However, the major stages, atomization, aerosol mixing, and aerosol deposition, are all scalable and the industrial versions of the components for larger scale production are commercially available. For example, wider printing heads, such as the 3mm wide printing head from Optomec, can replace the 300μm diameter nozzle used in this study for a larger printing area and a faster production rate. This study demonstrated that DMAJP is a facile, versatile, and

potentially scalable manufacturing process for PI/CNT nanocomposite films. The "conductive-on-demand" capability of DMAJP may enable many new designs of functionality for the new generation smart nanocomposites.

CHAPTER 7. CONCLUSTION AND FUTURE RESEARCH

7.1 Summary and Original Contribution

AJP possesses many advantages over other printed electronic technologies in terms of material varieties, feature size and non-contact process. It is also a relatively new technology for which the process control capabilities are still in the early stages. This obstacle has hindered AJP in scaling up for industrial applications. This thesis contributes and explores the AJP process in three major aspects. In the first sections of this thesis (Chapter 4), two exploratory device applications are selected to demonstrate the capability of AJP in device application. The challenge and limitation of current AJP processes such as the lack of quality assessment and control were also identified. In the first application, we demonstrated a novel gas sensor based on a carbon nanotube (CNT) material. CNT is a promising sensing material due to its large surface area and high sensitivity and selectivity toward various molecular. However, CNT sensors have not been widely adopted and manufactured in the industry. The challenge is that the fabrication processes suffer from non-uniform drying of the CNT solution called the coffee ring effect. The AJP process has tiny droplet sizes that minimize the coffee ring effect. However, the lack of process control for AJP results in variations in the deposition film thickness and resistance. We identified that the issue comes from the instability of the atomization process, which leads to drifting in the printing output volume. The proposed vibration-based method is adopted here to estimate a stable process time and help create maintenance strategies. We observed a 20% reduction in the final resistance performance.

In the second representative application, we demonstrated a 3D transmission line. The fabrication challenge here was to achieve precise control of the printed line feature and morphologies. Traditional printed electronic methods are limited to a feature size of as little as 100 μm, which is not suitable when the fabrication is moving toward high frequency where a 10-20 μm feature size is required. We demonstrated that our process model was derived from the design of experiments and can help minimize the printed overspray and precisely control the printed feature in 10 μm consistently. We observed a 50% improvement in the fabrication completion rate and a 30% variation reduction rate in the printed line width. Furthermore, we also demonstrated the fabrication capabilities for processing conductive and non-conductive materials with the same machine setup for complex 3D structures for the first time.

The second part of this thesis (Chapter 5) includes a set of process monitoring tools to advance the state-of-the-art of the AJP process for large-scale industrial applications in accuracy and repeatability. AJP is a unique additive manufacturing process for printed electronics. However, due to the fact it is a relatively new and emerging process, there is a lack of process monitoring and control techniques for the process. For instance, the process monitoring and control to achieve stable printing involving dynamically changing volume of ink have been a major issue troubling AJP users. Currently, the users rely on time-consuming, offline trial-and-error methods to calibrate the process. This dissertation research tackles the problem by introducing a real-time, advanced process sensing/monitoring (vibration-based) and statistical analysis approach that can significantly improve the efficiency and accuracy for process adjustment and control.

An image-based method that provides quantitative metrics of printed line morphologies was also developed. These two methods served as the foundation for understanding the effect of machine parameters and creating polynomial models through the design of experiment.

In the third part of the thesis (Chapter 6), we introduced two novel methods that extend current AJP capabilities to 3D printing and nanocomposite fabrication. In the first method, we developed a facile method that utilized the unique capability of AJP that enables printing on low surface energy substrate. This property allows printed devices to be easily transferred to another surface. We demonstrated that a print-stick-peel (PSP) method can be used for integrating sensors into 3D printed structures. This process provides a practical manufacturing technique for making the multifunctional smart structure and moving 3D printing parts from passive to active.

In the second method, we developed a novel dual material fabrication method for conductive tailorable nanocomposite fabrication. Conventional methods are limited to a single concentration of nanomaterial. They also suffer from being a heterogeneous distribution of nanomaterials. The atomization process in AJP provides opportunities to mix different materials in aerosol form and the mixing ratio can be adjusted on the fly. We demonstrated the ability to create a composite consisting of different nanomaterial concentrations in a single piece and in the same manufacturing step. In addition, atomization, aerosol mixing, and aerosol deposition were all potentially scalable. The method developed is a promising option that can be adopted for large-scale manufacturing.

This dissertation research lies on the integration of various techniques for AJP process improvement. Although various investigations have been conducted and reported for AJP, they focused on individual aspects/functions. This dissertation work is a pioneering research to integrate several techniques including vibration-based sensing, wavelet analysis, dual-material AJP, and integration of AJP and 3D printing. This integrative investigation has produced promising results for AJP process including fast and accurate process status change identification, significantly improved process repeatability, and new processing capabilities (for making new materials and structures).

In summary, the contributions of this thesis can be listed as follows:

1. Establishing quality control tools for an integrated manufacturing system of AJP with *in situ* monitoring;
2. Revealing the quantitative relationship between process parameters and printed structures;
3. Enhancing the fundamental understanding of capabilities and application potential of the AJP technology; and
4. Extending current AJP technology to other advanced manufacturing fields.

The impact for this thesis is to assist in unleashing the full potential of AJP technology in regards to: (1) increasing the stability and reliability; (2) enhancing novel device applications; and (3) extending AJP fabrication capabilities. Already possessing unmatched flexibility in prototyping of microelectronics, AJP will enable another leap from low rate lab-scale fabrication to high quality, high rate manufacturing for printed electronics.

7.2 Future Directions

In Chapter 4, we only presented two device applications that benefit from the AJP process and demonstrated the effectiveness of our process monitoring techniques. There are many novel devices that can be fabricated using the AJP process. We have developed several different sensor porotypes in the past, including strain sensors, biomedical sensors, RFID, and piezoelectric vibration sensors. These devices are summarized in Figure 65. There are also many device application opportunities that can be investigated with the capabilities of AJP, especially for emerging development for thin film transistors and biomedical sensors.

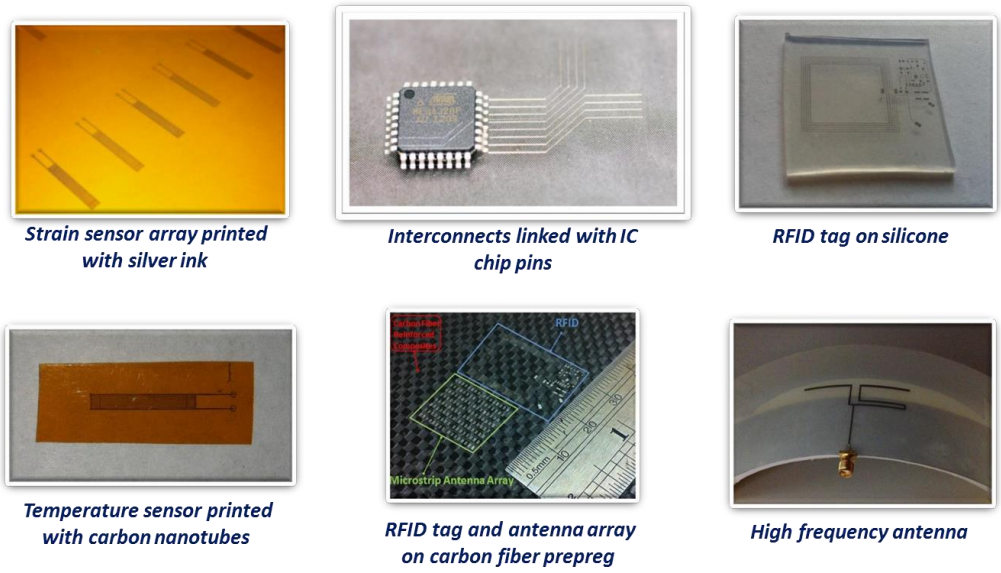

Figure 67: Prototype device developed in Georgia Tech manufacturing institute

In Chapter 5, we provided several tools for monitoring the print quality and proposed second order polynomial models for the relationship between machine parameters and printed line morphologies. As discussed in the literature, the AJP process is a complex gas-liquid phase process that involves a lot of uncertainty. In the study presented, we

considered only the on-line controllable variables such as gas flow rate and printing speed. There are several offline setting variables that could potentially influence the printing quality and stability. In general, the AJP process can be represented as a function:

$$Y = f(X, U, e, n) + \varepsilon \tag{48}$$

where Y is the process output. U is the online controllable variables that can be adjusted during each processing cycle. e and n are the noise factors with e representing online observable factors or estimated from on-line sensing signal, and n representing the noise that cannot be estimated or measured directly, and ϵ is the modeling error with $\epsilon \sim (0, \sigma_\epsilon^2)$. Examples of U, X, and e for the AJP process are given in Table 18.

Table 18: Variables in AJP process

	On-line controllable variable (U)	**Offline setting variable (X)**	**Observable noise (e)**	**Process response factor (Y)**
Atomization	Ultrasonic power	Ink sheet thickness Ink viscosity	Pressure at ink jar	Droplet size distribution Vibration of vial
Deposition	Carrier gas flow Sheath gas flow Platen Speed	Ink viscosity Nozzle diameter Stand-off distance	Pressure at deposition head	Line morphology

The objective is to minimize the response Y variance and can be written as the following equation with least square loss function $L = (Y - T)^2$

$$\begin{aligned} J &= \min E[(Y - T)^2] \\ &= \min E[(\mu_Y - T)^2 + V_Y] \end{aligned} \tag{49}$$

where T is the target value and $\mu_Y - T$ is the process mean deviation from the target, and V_Y is the variance of the response. The future extension for the modeling could be to find

the optimal control parameters for both online and offline control variables and develop statistical measures for quantifying the observable noise factors.

In Chapter 6, we proposed two novel methods for fabricating smart structures or material with AJP. Smart structures and multifunctional composite materials have a lot of potential for becoming next generation technologies. The methods we proposed just enabled a new way for functional fabrication. Research studies, such as novel material design using different mixing materials that can be used for new types of device applications, can be discovered based on our fabrication method. Theoretical study, such as computational fluid dynamic simulation and mechanical characteristics for mixing printing, can also be considered as future research direction.

REFERENCES

1. Khan, S., L. Lorenzelli, and R.S. Dahiya, *Technologies for Printing Sensors and Electronics Over Large Flexible Substrates: A Review.* IEEE Sensors Journal, 2015. **15**(6): p. 3164-3185.

2. Hansen, C.J., et al., *High-Throughput Printing via Microvascular Multinozzle Arrays.* Advanced Materials, 2012. **25**(1): p. 96-102.

3. Bao, Z., et al., *High-Performance Plastic Transistors Fabricated by Printing Techniques.* Chemistry of Materials, 1997. **9**(6): p. 1299-1301.

4. Krebs, F.C., et al., *Production of large-area polymer solar cells by industrial silk screen printing, lifetime considerations and lamination with polyethyleneterephthalate.* Solar Energy Materials and Solar Cells, 2004. **83**(2-3): p. 293-300.

5. Ito, S., et al., *Fabrication of screen-printing pastes from TiO2 powders for dye-sensitised solar cells.* Progress in Photovoltaics: Research and Applications, 2007. **15**(7): p. 603-612.

6. Winther-Jensen, B. and F.C. Krebs, *High-conductivity large-area semi-transparent electrodes for polymer photovoltaics by silk screen printing and vapour-phase deposition.* Solar Energy Materials and Solar Cells, 2006. **90**(2): p. 123-132.

7. Chang, W.-Y., et al., *A Large Area Flexible Array Sensors Using Screen Printing Technology.* Journal of Display Technology, 2009. **5**(6): p. 178-183.

8. Nagata, R., *A glucose sensor fabricated by the screen printing technique.* Biosensors and Bioelectronics, 1995. **10**(3-4): p. 261-267.

9. Khaleel, H.R., H.M. Al-Rizzo, and A.I. Abbosh, *Design, Fabrication, and Testing of Flexible Antennas*. Advancement in Microstrip Antennas with Recent Applications. 2013.

10. Noh, J., et al., *Scalability of Roll-to-Roll Gravure-Printed Electrodes on Plastic Foils.* IEEE Transactions on Electronics Packaging Manufacturing, 2010. **33**(4): p. 275-283.

11. de la Fuente Vornbrock, A., et al., *Fully gravure and ink-jet printed high speed pBTTT organic thin film transistors.* Organic Electronics, 2010. **11**(12): p. 2037-2044.

12. Jung, M., et al., *All-Printed and Roll-to-Roll-Printable 13.56-MHz-Operated 1-bit RF Tag on Plastic Foils.* IEEE Transactions on Electron Devices, 2010. **57**(3): p. 571-580.

13. Puetz, J. and M.A. Aegerter, *Direct gravure printing of indium tin oxide nanoparticle patterns on polymer foils.* Thin Solid Films, 2008. **516**(14): p. 4495-4501.

14. Lau, P.H., et al., *Fully Printed, High Performance Carbon Nanotube Thin-Film Transistors on Flexible Substrates.* Nano Letters, 2013. **13**(8): p. 3864-3869.

15. Secor, E.B., et al., *Gravure Printing of Graphene for Large-area Flexible Electronics.* Advanced Materials, 2014. **26**(26): p. 4533-4538.

16. Soltman, D.B., *Understanding inkjet printed pattern generation*. 2011, University of California, Berkeley.

17. Jun, J.H., et al., *Flexible TFTs based on solution-processed ZnO nanoparticles.* Nanotechnology, 2009. **20**(50): p. 505201.

18. Kang, W., M. Kitamura, and Y. Arakawa, *High performance inkjet-printed C60 fullerene thin-film transistors: Toward a low-cost and reproducible solution process.* Organic Electronics, 2013. **14**(2): p. 644-648.

19. Chen, B., et al., *All-polymer RC filter circuits fabricated with inkjet printing technology.* Solid-State Electronics, 2003. **47**(5): p. 841-847.

20. Liu, Y., T. Cui, and K. Varahramyan, *All-polymer capacitor fabricated with inkjet printing technique.* Solid-State Electronics, 2003. **47**(9): p. 1543-1548.

21. Mager, D., et al., *An MRI Receiver Coil Produced by Inkjet Printing Directly on to a Flexible Substrate.* IEEE Transactions on Medical Imaging, 2010. **29**(2): p. 482-487.

22. Bidoki, S.M., J. Nouri, and A.A. Heidari, *Inkjet deposited circuit components.* Journal of Micromechanics and Microengineering, 2010. **20**(5): p. 055023.

23. Li, J., M.C. Lemme, and M. Östling, *Inkjet Printing of 2D Layered Materials.* ChemPhysChem, 2014. **15**(16): p. 3427-3434.

24. Singh, M., et al., *Inkjet Printing-Process and Its Applications.* Advanced Materials, 2010. **22**(6): p. 673-685.

25. Chang, J., T. Ge, and E. Sanchez-Sinencio. *Challenges of printed electronics on flexible substrates*. in *Circuits and Systems (MWSCAS), 2012 IEEE 55th International Midwest Symposium on*. 2012. IEEE.

26. Kamyshny, A. and S. Magdassi, *Conductive nanomaterials for printed electronics.* Small, 2014. **10**(17): p. 3515-3535.

27. Aleeva, Y. and B. Pignataro, *Recent advances in upscalable wet methods and ink formulations for printed electronics.* Journal of Materials Chemistry C, 2014. **2**(32): p. 6436-6453.

28. Anthony, J.E., *Organic electronics: addressing challenges.* Nature materials, 2014. **13**(8): p. 773-775.

29. Sekine, C., et al., *Recent progress of high performance polymer OLED and OPV materials for organic printed electronics.* Science and Technology of Advanced Materials, 2014. **15**(3): p. 034203.

30. Lee, J., et al., *Register control algorithm for high resolution multilayer printing in the roll-to-roll process.* Mechanical Systems and Signal Processing, 2015. **60-61**: p. 706-714.

31. Chang, Y.-H., et al., *A facile method for integrating direct-write devices into three-dimensional printed parts.* Smart Materials and Structures, 2015. **24**(6): p. 065008.

32. Wang, K., et al. *Evaluation of Quality of Printed Strain Sensors for Composite Structural Health Monitoring Applications*. in *Proc. SAMPE Fall Technical 2013 Conference*. 2013. Vince Wichita, KS, USA.

33. Goth, C., S. Putzo, and J. Franke, *Aerosol Jet printing on rapid prototyping materials for fine pitch electronic applications*, in *2011 IEEE 61st Electronic Components and Technology Conference (ECTC)*. 2011, Institute of Electrical and Electronics Engineers (IEEE).

34. Verheecke, W., et al. *Optimizing aerosol jet printing of silver interconnects on polyimide film for embedded electronics applications*. in *8th International Danube Adria Association for Automation and Manufacturing Baltic Conference "Industrial Engi-neering," Tallinn, Estonia, Apr*. 2012.

35. Mahajan, A., C.D. Frisbie, and L.F. Francis, *Optimization of Aerosol Jet Printing for High-Resolution, High-Aspect Ratio Silver Lines.* ACS Applied Materials & Interfaces, 2013. **5**(11): p. 4856-4864.

36. Seifert, T., et al., *Additive Manufacturing Technologies Compared: Morphology of Deposits of Silver Ink Using Inkjet and Aerosol Jet Printing.* Industrial & Engineering Chemistry Research, 2015. **54**(2): p. 769-779.

37. Brakora, K.F., J. Halloran, and K. Sarabandi, *Design of 3-D Monolithic MMW Antennas Using Ceramic Stereolithography.* IEEE Transactions on Antennas and Propagation, 2007. **55**(3): p. 790-797.

38. Chieh, J.-C.S., et al., *Development of a Ku-Band Corrugated Conical Horn Using 3-D Print Technology*. IEEE Antennas and Wireless Propagation Letters, 2014. **13**: p. 201-204.

39. Kang, B.J., C.K. Lee, and J.H. Oh, *All-inkjet-printed electrical components and circuit fabrication on a plastic substrate.* Microelectronic Engineering, 2012. **97**: p. 251-254.

40. Ferrer-Vidal, A., et al., *Integration of sensors and RFID¿s on ultra-low-cost paper-based substrates for wireless sensor networks applications*, in *2006 2nd IEEE Workshop on Wireless Mesh Networks*. 2006, Institute of Electrical and Electronics Engineers (IEEE).

41. Liang, M., et al., *3D printed multilayer microstrip line structure with vertical transition toward integrated systems*, in *2015 IEEE MTT-S International Microwave Symposium*. 2015, Institute of Electrical and Electronics Engineers (IEEE).

42. Lopes, A.J., E. MacDonald, and R.B. Wicker, *Integrating stereolithography and direct print technologies for 3D structural electronics fabrication.* Rapid Prototyping Journal, 2012. **18**(2): p. 129-143.

43. Samanta, K.K., *A novel multilayer/3d technology for advanced microwave and millimetre-wave wireless circuits and systems*, in *2012 5th International Conference on Computers and Devices for Communication (CODEC)*. 2012, Institute of Electrical and Electronics Engineers (IEEE).

44. Meier, H., et al., *Inkjet printed, conductive, 25 μm wide silver tracks on unstructured polyimide.* physica status solidi (a), 2009. **206**(7): p. 1626-1630.

45. Yu-Min, F., et al., *A Combined Process of Liftoff and Printing for the Fabrication of Scalable Inkjet Printed Microstructures on a Flexible Substrate.* IEEE Transactions on Electron Devices, 2015. **62**(4): p. 1248-1254.

46. van den Berg, A.M.J., et al., *Geometric control of inkjet printed features using a gelating polymer.* J. Mater. Chem., 2007. **17**(7): p. 677-683.

47. Paulsen, J.A., et al., *Printing conformal electronics on 3D structures with Aerosol Jet technology*, in *2012 Future of Instrumentation International Workshop (FIIW) Proceedings*. 2012, Institute of Electrical and Electronics Engineers (IEEE).

48. Cai, F., et al., *High resolution aerosol jet printing of D- band printed transmission lines on flexible LCP substrate*, in *2014 IEEE MTT-S International Microwave Symposium (IMS2014)*. 2014, Institute of Electrical and Electronics Engineers (IEEE).

49. Cohen, D.L., *Fostering Mainstream Adoption of Industrial 3D Printing: Understanding the Benefits and Promoting Organizational Readiness.* 3D Printing and Additive Manufacturing, 2014. **1**(2): p. 62-69.

50. Lee, Y.C., *CPW-TO-STRIPLINE VERTICAL VIA TRANSITIONS FOR 60GHZ LTCC SOP APPLICATIONS.* Progress In Electromagnetics Research Letters, 2008. **2**: p. 37-44.

51. Decrossas, E., et al., *High-Performance and High-Data-Rate Quasi-Coaxial LTCC Vertical Interconnect Transitions for Multichip Modules and System-on-Package Applications.* IEEE Transactions on Components, Packaging and Manufacturing Technology, 2015. **5**(3): p. 307-313.

52. Han, L., et al., *Compact and Broadband Transition of Microstrip Line to Finite-Ground Coplanar Waveguide*, in *2008 38th European Microwave Conference*. 2008, Institute of Electrical and Electronics Engineers (IEEE).

53. Pozar, D.M., *Microwave engineering*. 2009: John Wiley & Sons.

54. Juno, K., et al., *A novel low-loss low-crosstalk interconnect for broad-band mixed-signal silicon MMICs.* IEEE Transactions on Microwave Theory and Techniques, 1999. **47**(9): p. 1830-1835.

55. Chahadih, A., et al., *V-Band Via-Less GCPW-to-Microstrip Transition Designed on PET Flexible Substrate Using Inkjet Printing Technology.* IEEE Microwave and Wireless Components Letters, 2015. **25**(7): p. 436-438.

56. Azucena, O., et al., *Inkjet printing of passive microwave circuitry*, in *2008 IEEE MTT-S International Microwave Symposium Digest*. 2008, Institute of Electrical and Electronics Engineers (IEEE).

57. Cook, B.S. and A. Shamim, *Inkjet Printing of Novel Wideband and High Gain Antennas on Low-Cost Paper Substrate.* IEEE Transactions on Antennas and Propagation, 2012. **60**(9): p. 4148-4156.

58. Lee, K.J., et al., *Environmentally friendly synthesis of organic-soluble silver nanoparticles for printed electronics.* Nanotechnology, 2007. **18**(33).

59. Jones, C.S., et al., *Aerosol-jet-printed, high-speed, flexible thin-film transistor made using single-walled carbon nanotube solution.* Microelectronic Engineering, 2010. **87**(3): p. 434-437.

60. Aernouts, T., et al., *Polymer based organic solar cells using ink-jet printed active layers.* Applied Physics Letters, 2008. **92**(3): p. 033306.

61. Yang, L., et al., *RFID tag and RF structures on a paper substrate using inkjet-printing technology.* Ieee Transactions on Microwave Theory and Techniques, 2007. **55**(12): p. 2894-2901.

62. Rida, A., et al., *Conductive Inkjet-Printed Antennas on Flexible Low-Cost Paper-Based Substrates for RFID and WSN Applications.* Ieee Antennas and Propagation Magazine, 2009. **51**(3): p. 13-23.

63. Maiwald, M., et al., *INKtelligent printed strain gauges.* Sensors and Actuators A: Physical, 2010. **162**(2): p. 198-201.

64. Bidoki, S.M., et al., *Ink-jet fabrication of electronic components.* Journal of Micromechanics and Microengineering, 2007. **17**(5): p. 967-974.

65. Wood, V., et al., *Inkjet-Printed Quantum Dot–Polymer Composites for Full-Color AC-Driven Displays.* Advanced Materials, 2009. **21**(21): p. 2151-2155.

66. O'Donnell, J., et al., *All-printed smart structures: a viable option?*, in *Proc. SPIE*. 2014. p. 905728-905729.

67. Palmer, J.A., et al., *Realizing 3-D interconnected direct write electronics within smart stereolithography structures.* Electronic and Photonic Packaging, Integration and Packaging of MICRO/NANO/Electronic Systems, 2005: p. 287-293.

68. Medina, F. and A. Lopes, *Hybrid Manufacturing: Integrating Direct-Write and Stereolithography*. Proceedings of the …, 2005: p. 39-49.

69. Lopes, A.J., et al., *Expanding rapid prototyping for electronic systems integration of arbitrary form*, in *Proceedings of the 17th Annual Solid Freeform Fabrication Symposium, University of Texas at Austin, Austin, TX*. 2006, Society of Manufacturing Engineers.

70. Castillo, S., et al., *Electronics Integration in Conformal Substrates Fabricated with Additive Layered Manufacturing.* p. 730-737.

71. Vogeler, F., et al., *An Initial Study of Aerosol Jet® Printed Interconnections on Extrusion-Based 3D-Printed Substrates.* Strojniški vestnik – Journal of Mechanical Engineering, 2013. **59**(11): p. 689-696.

72. Paulsen, J.A., et al., *Printing conformal electronics on 3D structures with Aerosol Jet technology*, in *Future of Instrumentation International Workshop (FIIW), 2012*. 2012, IEEE. p. 1-4.

73. Espalin, D., et al., *3D Printing multifunctionality: structures with electronics.* International Journal of Advanced Manufacturing Technology, 2014. **72**(5-8): p. 963-978.

74. Perez, K.B. and C.B. Williams, *DESIGN CONSIDERATIONS FOR HYBRIDIZING ADDITIVE MANUFACTURING AND DIRECT WRITE TECHNOLOGIES.* 2014: p. 1-12.

75. Perelaer, J., B.J. de Gans, and U.S. Schubert, *Ink-jet Printing and Microwave Sintering of Conductive Silver Tracks.* Advanced Materials, 2006. **18**(16): p. 2101-2104.

76. Lopes, A.J., et al., *Laser curing of silver-based conductive inks for in situ 3D structural electronics fabrication in stereolithography.* Journal of Materials Processing Technology, 2014. **214**(9): p. 1935-1945.

77. Abbel, R., et al., *Photonic flash sintering of silver nanoparticle inks: a fast and convenient method for the preparation of highly conductive structures on foil.* MRS Communications, 2012. **2**(04): p. 145-150.

78. Ko, S.H., et al., *Air stable high resolution organic transistors by selective laser sintering of ink-jet printed metal nanoparticles.* Applied Physics Letters, 2007. **90**(14): p. -.

79. Schroder, K., S. McCool, and W. Furlan, *Broadcast photonic curing of metallic nanoparticle films.* Presented at NSTI Nanotech May, 2006. **7**: p. 11.

80. Lee, C.H., et al., *Peel-and-stick: fabricating thin film solar cell on universal substrates.* Sci Rep, 2012. **2**: p. 1000.

81. Carlson, A., et al., *Transfer printing techniques for materials assembly and micro/nanodevice fabrication.* Advanced materials (Deerfield Beach, Fla.), 2012. **24**(39): p. 5284-318.

82. Pereni, C.I., et al., *Surface free energy effect on bacterial retention.* Colloids and Surfaces B: Biointerfaces, 2006. **48**(2): p. 143-147.

83. Herrmann, J., et al., *Nanoparticle films as sensitive strain gauges.* Applied Physics Letters, 2007. **91**(18): p. -.

84. Takei, K., et al., *Highly sensitive electronic whiskers based on patterned carbon nanotube and silver nanoparticle composite films.* Proceedings of the National Academy of Sciences, 2014. **111**(5): p. 1703-1707.

85. Ando, B. and S. Baglio, *All-Inkjet Printed Strain Sensors.* Sensors Journal, IEEE, 2013. **13**(12): p. 4874-4879.

86. Smith, J., et al., *Space durable polymer/carbon nanotube films for electrostatic charge mitigation.* Polymer, 2004. **45**(3): p. 825-836.

87. Jiang, Q., et al., *Mechanical, electrical and thermal properties of aligned carbon nanotube/polyimide composites.* Composites Part B: Engineering, 2014. **56**: p. 408-412.

88. Bauhofer, W. and J.Z. Kovacs, *A review and analysis of electrical percolation in carbon nanotube polymer composites.* Composites Science and Technology, 2009. **69**(10): p. 1486-1498.

89. Lin-Gibson, S., et al., *Elastic flow instability in nanotube suspensions.* Physical review letters, 2004. **92**(4): p. 048302.

90. Rahatekar, S., et al., *Optical microstructure and viscosity enhancement for an epoxy resin matrix containing multiwall carbon nanotubes.* Journal of Rheology (1978-present), 2006. **50**(5): p. 599-610.

91. Ausman, K.D., et al., *Organic solvent dispersions of single-walled carbon nanotubes: toward solutions of pristine nanotubes.* The Journal of Physical Chemistry B, 2000. **104**(38): p. 8911-8915.

92. Zhu, J., et al., *Improving the dispersion and integration of single-walled carbon nanotubes in epoxy composites through functionalization.* Nano Letters, 2003. **3**(8): p. 1107-1113.

93. Sun, Y.-P., et al., *Soluble Dendron-Functionalized Carbon Nanotubes: Preparation, Characterization, and Properties §.* Chemistry of Materials, 2001. **13**(9): p. 2864-2869.

94. Zeng, H.L., C. Gao, and D.Y. Yan, *Poly (ϵ-caprolactone)-Functionalized Carbon Nanotubes and Their Biodegradation Properties.* Advanced Functional Materials, 2006. **16**(6): p. 812-818.

95. Shen, J., et al., *The reinforcement role of different amino-functionalized multi-walled carbon nanotubes in epoxy nanocomposites.* Composites Science and Technology, 2007. **67**(15-16): p. 3041-3050.

96. Wang, M., K. Pramoda, and S.H. Goh, *Enhancement of interfacial adhesion and dynamic mechanical properties of poly (methyl methacrylate)/multiwalled carbon nanotube composites with amine-terminated poly (ethylene oxide).* Carbon, 2006. **44**(4): p. 613-617.

97. Khabashesku, V.N., W.E. Billups, and J.L. Margrave, *Fluorination of single-wall carbon nanotubes and subsequent derivatization reactions.* Accounts of chemical research, 2002. **35**(12): p. 1087-1095.

98. Lauffer, P., et al., *Functionalization of single-walled carbon nanotubes by aromatic molecules studied by scanning tunneling microscopy.* physica status solidi (b), 2006. **243**(13): p. 3213-3216.

99. Ferreira, O.P., et al., *Non-covalent interaction of benzonitrile with single-walled carbon nanotubes.* Journal of Nanoparticle Research, 2009. **11**(8): p. 2163-2170.

100. Lemek, T., et al., *Non-Covalent Functionalization of Multi-Walled Carbon Nanotubes with Organic Aromatic Compounds.* Journal of Nanoscience and Nanotechnology, 2007. **7**(9): p. 3081-3088.

101. Hu, C., et al., *Water-soluble single-walled carbon nanotubes via noncovalent functionalization by a rigid, planar and conjugated diazo dye.* Carbon, 2006. **44**(3): p. 428-434.

102. Lebrón-Colón, M., et al., *Reinforced thermoplastic polyimide with dispersed functionalized single wall carbon nanotubes.* ACS applied materials & interfaces, 2010. **2**(3): p. 669-676.

103. Yuan, W., J. Che, and M.B. Chan-Park, *A Novel Polyimide Dispersing Matrix for Highly Electrically Conductive Solution-Cast Carbon Nanotube-Based Composite.* Chemistry of Materials, 2011. **23**(18): p. 4149-4157.

104. Cai, H., F. Yan, and Q. Xue, *Investigation of tribological properties of polyimide/carbon nanotube nanocomposites.* Materials Science and Engineering: A, 2004. **364**(1-2): p. 94-100.

105. Jiang, X., Y. Bin, and M. Matsuo, *Electrical and mechanical properties of polyimide–carbon nanotubes composites fabricated by in situ polymerization.* Polymer, 2005. **46**(18): p. 7418-7424.

106. Kim, B.S., et al., *Preparation and characterization of polyimide/carbon-nanotube composites.* Macromolecular Research, 2007. **15**(4): p. 357-362.

107. Oh, S.B., Y.J. Kim, and J.H. Kim, *Preparation and properties of polyimide nanocomposites via a soluble polyisoimide precursor.* Journal of Applied Polymer Science, 2006. **99**(3): p. 869-874.

108. Atar, N., et al., *Reinforced Carbon Nanotubes as Electrically Conducting and Flexible Films for Space Applications.* ACS Applied Materials & Interfaces, 2014. **6**(22): p. 20400-20407.

109. Kahn, B., *The M3D aerosol jet system, an alternative to inkjet printing for printed electronics.* Organic and Printed Electronics, 2007. **1**: p. 14-17.

110. Hörteis, M., et al., *Further progress in metal aerosol jet printing for front side metallization of silicon solar cells.* Proceedings of the 22nd EU-PVSEC, 2007.

111. Renn, M.J., *Direct write™ system*. 2007, Google Patents.

112. Sukeshini, M., et al., *Aerosol Jet® Printing of functionally graded SOFC anode interlayer and microstructural investigation by low voltage scanning electron microscopy.* Journal of Power Sources, 2013. **224**: p. 295-303.

113. Sukeshini, A., et al., *Aerosol jet printing and microstructure of SOFC electrolyte and cathode layers.* ECS Transactions, 2011. **35**(1): p. 2151-2160.

114. Endo, M., et al., *'Buckypaper' from coaxial nanotubes.* Nature, 2005. **433**(7025): p. 476-476.

115. Wang, Z., et al., *Processing and property investigation of single-walled carbon nanotube (SWNT) buckypaper/epoxy resin matrix nanocomposites.* Composites Part a-Applied Science and Manufacturing, 2004. **35**(10): p. 1225-1232.

116. Ashrafi, B., et al., *Correlation between Young's modulus and impregnation quality of epoxy-impregnated SWCNT buckypaper.* Composites Part a-Applied Science and Manufacturing, 2010. **41**(9): p. 1184-1191.

117. Sirringhaus, H., et al., *High-Resolution Inkjet Printing of All-Polymer Transistor Circuits.* Science, 2000. **290**(5499): p. 2123-2126.

118. Ho, C.C., J.W. Evans, and P.K. Wright, *Direct write dispenser printing of a zinc microbattery with an ionic liquid gel electrolyte.* Journal of Micromechanics and Microengineering, 2010. **20**(10).

119. Balde, J.W., *Forming vias through multilayer circuit boards*. 1981, U.S. Patent No. 4,258,468. 31 Mar. 1981.

120. Bhatt, A.C., et al., *Manufacturing circuit board assemblies having filled vias*. 1998, U.S. Patent No. 5,822,856. 20 Oct. 1998.

VITA

Yung-Hang Chang was born in Taipei, Taiwan. He received his B.S degree in Computer Science from Yuan Ze University in 2007 and M.S. degree in Industrial Engineering from Georgia Institute of Technology in 2013.